Western Australia School of Mines: Minerals, Energy and Chemical Engineering

Fuels and Energy Technology Institute

Reaction Mechanisms of Biochar Gasification and Tar Reforming

Yurong Liu

This thesis is presented for the Degree of

Doctor of Philosophy

of

Curtin University

Jan 2021

Declaration

To the best of my knowledge and belief this thesis contains no material previously published by any other person except where due acknowledgement has been made.

This thesis contains no material which has been accepted for the award of any other degree or diploma in any university.

25 January 2021

To my beloved husband Yebo Liu

For his endless love, support and encouragement.

“So high, so low, so many things to know”

— Vernor Vinge, A Deepness in the Sky

Acknowledgements

I would like to acknowledge the financial support from the Australian Research Council (DP180101788, FT160100303). I also acknowledge the funding from the Australian Government through ARENA's Emerging Renewables Program. Part of the research was undertaken using the XPS instrumentation (ARC LE120100026) at the John de Laeter Centre, Curtin University. I would like to thank the scientists from the SAXS beamline at the Australian Synchrotron for their help. I wish to thank Richard Gunawan, Lei Zhang, Zhitao Wang, Li Dong, Yao Song and Shu Zhang for providing bio-oil and biochar samples.

I wish to express my deepest gratitude to many wonderful people, who have made my PhD candidacy one of the most memorable and enjoyable journeys.

Thank you, associate professor Mark Paskevicius, it has been a real privilege and honour having you as my supervisor. You were always ready to answer my questions and to point me in the right directions. You were always willing to give me your immense knowledge. You were always patient with me, through all my confusions and mistakes. You have taught me so many valuable academic skills. Your guidance and encouragement have made it possible for the success of my PhD candidacy. My co-supervisor, Professor Gordon Parkinson, it is a pleasure to work with you. You taught me think creatively and to plan ahead for everything. You were always willing to help me overcome difficulties. Professor Chun-Zhu Li, who left my thesis committee later on, is with me all the time. I would like to thank you for giving me this opportunity and giving me your expertise. Thank you for your motivation and guidance in my experimental work as well as the writing of papers. Your cautious attitude towards research will always be an inspiration for my academic career.

I also want to express my appreciation to my friends and colleagues from FETI at Curtin University: Hongqi Wang, Veronica Sofianos, Li Dong, Yao Song, Lei Zhang, Tingting Li, Shuai Wang, Zhitao Wang, Richard Gunawan, Angelina Rossiter, Lana McQueen, Manoj Kumar Jena, Sweta Singh, Juntao Wang. Thank you all for your help.

Last and foremost, I wish to express my love and gratitude to my families. My parents and parents in law, thank you for your unconditional support. My beloved husband, Yebo Liu, you

are my source of emotional strength and my advisor. You always believed me and encourage me to chase my dreams. You are a wonderful and caring companion. I'm so blessed to have you in my life. 我爱你，老公。

Abstract

Biomass is a renewable energy source and represents a valid alternative to fossil fuels. Gasification is a promising technology to thermochemically convert biomass into syngas and a solid product, called biochar. The produced syngas can be further used for the production of electricity, heat, hydrogen and second-generation bioproducts such as chemicals and transportation fuels. During gasification, the pore structure of biochar changes drastically with the continuous removal of carbon atoms by gasifying agents. The study of the changes in the pore structure of biochar is crucial to understanding the gasification process, as well as to optimizing the conditions that are used for the preparation of activated carbon using biochar as a precursor.

Therefore, one of the main objectives of this project is to study the pore development in biochar as function of gasification mechanism. Small angle X-ray scattering (SAXS) was used as an in situ and ex situ characterization technique to study the evolution of the pore structure in biochar during gasification in H_2O, CO_2 and a mixture of them (H_2O/CO_2). A complete picture of the evolution pathway of the pore network in biochar was provided. The impact of gasification temperature (700, 800 and 900 °C) and biomass particle size on the development of pores in biochar was also investigated. The results showed that the pore structure evolution in biochar is paralleled by the transformation of its carbon matrix. The pore development is the result of the conversion and removal of carbon by gasifying agents. CO_2 tends to produce a highly microporous biochar. The carbon removal in CO_2 is more selective and the derived biochar exhibits a pore fractal network on the mesopore size scale. While during gasification in H_2O and H_2O/CO_2, pore enlargement is predominant and the derived biochar samples show surface fractal features. The difference in the pore development between biochar gasified in H_2O and CO_2 is attributed to the different reactivity of H_2O and CO_2, as well as the different contents of O-containing functional groups in biochar.

Another major objective of this work is to investigate the mechanism of tar reforming using biochar as a catalyst. Tar formation is practically unavoidable during biomass gasification and the removal of tar from syngas is the major challenge for the commercialization of gasification technologies. Catalytic tar reforming is one of the most

promising techniques for producing high-quality syngas on a commercial scale. Biochar has great potential to be used as a catalyst for the removal of tar. In this study, we investigated the effects of the structure of biochar on its catalytic activity, focusing on the role of O-containing functional groups of biochar in tar conversion. In the end, a reforming mechanism is proposed, taking into consideration the interactions between O-containing functional groups and tar components. The findings showed that O-containing functional groups especially the aromatic C-O groups in biochar play a critical role in determining the catalytic activity of biochar for both the steam and dry reforming of tar. Both steam and CO_2 activation of biochar can enhance the catalytic activity of biochar by adding O-containing functional groups biochar, while steam activation is more effective compared to activation in CO_2 for the same time. Moreover, the large hydrocarbons and non-oxygen-containing tar compounds are preferably to be adsorbed and reformed over biochar surface, rather than in the gas phase. The O-containing functional groups in biochar are likely to act as active sites that promote the destabilization of tar compounds to form active tar radicals, enhancing the destruction of tar.

List of publications

Y. Liu, M. Paskevicius, H. Wang, G. Parkinson, J.P. Veder, X. Hu, C.-Z. Li, Role of O-containing functional groups in biochar during the catalytic steam reforming of tar using the biochar as a catalyst, Fuel. 253 (2019) 441–448. https://doi.org/10.1016/j.fuel.2019.05.037.

Y. Liu, M. Paskevicius, H. Wang, C. Fushimi, G. Parkinson, C.-Z. Li, Difference in tar reforming activities between biochar catalysts activated in H_2O and CO_2, Fuel, 271 (2020) 117636. https://doi.org/10.1016/j.fuel.2020.117636.

Y. Liu, M. Paskevicius, M.V. Sofianos, G. Parkinson, C.-Z. Li, In situ SAXS studies of the pore development in biochar during gasification, Carbon, N Y 2021;172:454–62. https://doi.org/10.1016/j.carbon.2020.10.028.

Y. Liu, M. Paskevicius, M.V. Sofianos, G. Parkinson, S. Wang, C.-Z. Li, A SAXS study of the pore structure evolution in biochar during gasification in H_2O, CO_2 and H_2O/CO_2, Fuel. 292 (2021) 120384. https://doi.org/10.1016/j.fuel.2021.120384.

Y. Liu, M. Paskevicius, H. Wang, G. Parkinson, J. Wei, A. M.A, C.-Z. Li, Insights into the mechanism of tar reforming using biochar as a catalyst. Fuel. 296 (2021) 120672. https://doi.org/10.1016/j.fuel.2021.120672.

M.A. Akhtar, S. Zhang, X. Shao, H. Dang, **Y. Liu**, T. Li, L. Zhang, C.-Z. Li, Kinetic compensation effects in the chemical reaction-controlled regime and mass transfer-controlled regime during the gasification of biochar in O_2, Fuel Process. Technol, 181 (2018) 25–32. https://doi.org/10.1016/j.fuproc.2018.09.009.

A.T.F. Afolabi, P.N. Kechagiopoulos, **Y. Liu**, C.-Z. Li, Kinetic features of ethanol steam reforming and decomposition using a biochar-supported Ni catalyst, Fuel Process. Technol. 212 (2021) 106622. https://doi.org/10.1016/j.fuproc.2020.106622.

H. Wang, R. Gunawan, Z. Wang, L. Zhang, **Y. Liu**, S. Wang, M.D.M. Hasan, C.-Z. Li, High-pressure reactive distillation of bio-oil for reduced polymerisation, Fuel Process. Technol. 211 (2021) 106590. https://doi.org/10.1016/j.fuproc.2020.106590.

J.Wei, Q. Guo, X. Dong, L. Ding, A. Mosqueda, **Y. Liu**, K. Yoshikawa, G. Yu, Effect of Hydrothermal Carbonization Temperature on Reactivity and Synergy of Co-gasification of

Biomass Hydrochar and Coal. Appl Therm Eng 2021;183:116232. https://doi.org/10.1016/j.applthermaleng.2020.116232.

J. Wei, M. Wang, F. Wang, X. Song, G. Yu, **Y. Liu**, H. Vuthaluru, J. Xu, Y. Xu, H. Zhang, S. Zhang, A review on reactivity characteristics and synergy behavior of biomass and coal Co-gasification, Int. J. Hydrogen Energy. 02 (2021) 0360–3199. https://doi.org/10.1016/j.ijhydene.2021.02.162.

Table of contents

List of figures

List of tables

Chapter 1

Introduction and overview

1.1 Literature review

1.1.1 Biomass gasification as a promising technology for bioenergy production

The increasing concern about sustainability and global warming has led to an ever-growing demand for clean and renewable energy to meet the world's future energy needs. Bioenergy utilises renewable biomass to generate electricity, heat, transport fuels and chemicals [1]. Biomass is an abundant resource including forest residues, municipal waste, and waste from the agricultural and animals. Moreover, when produced and used on a sustainable basis, biomass is a carbon-neutral carrier and can make a large contribution to minimising greenhouse gas emissions [2]. Therefore, bioenergy is considered as a promising alternative to tradition fossil fuels.

One of the most promising technologies to achieve the highly efficient and clean utilisation of biomass is gasification [3]. Biomass gasification is a partial oxidation process that thermochemically converts biomass into syngas (CO and H_2). The produced syngas can be further used to generate power and chemical such as methanol and Fischer-Tropsch fuels (*Figure* 1. *1*) [4,5]. Compared with high rank fuels such as coal, biomass has specific features of a high content of oxygen and a low content of aromatic moieties, which allows the gasification of biomass to be carried out at relatively low temperatures [6]. In addition, gasification can achieve high efficiency of biomass conversion and a versatile applications of the gas products, thus gasification is a particularly attractive technology to utilise biomass [6].

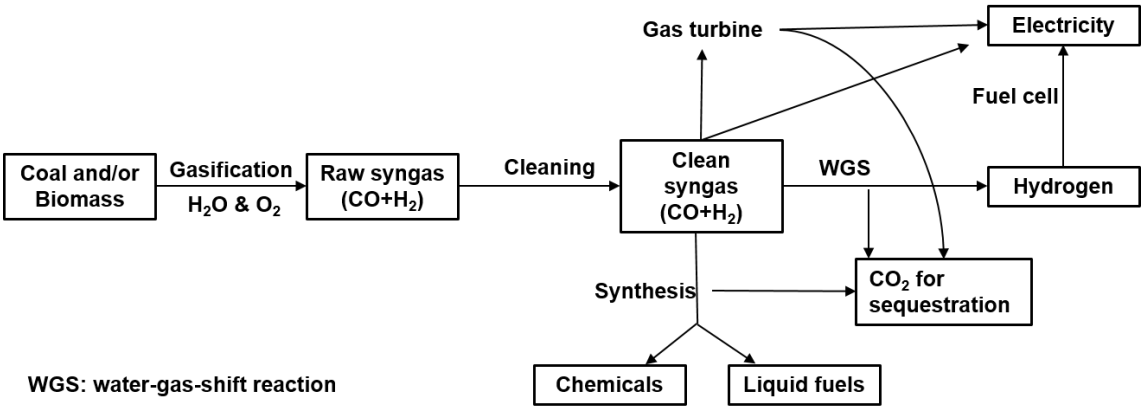

Figure 1. 1. A flow chart showing the utilisation of gasification technology [4]. Copyright (2013), with permission from Elsevier.

1.1.2 Significance of studies on the pore structure of biochar for understanding the mechanism of biochar gasification

During biomass gasification, biomass initially decomosed at high temperatures to generate volatiles and a solid residue called biochar [4]. Biochar continually react with gasifying agents such as O_2, H_2O and CO_2 [4,7–9] to produce syngas. This process is the rate-determining step in the process. Understanding the reaction mechanisms of biochar gasification is essential to the optimization and improvement of gasification technologies.

Extensive efforts have been made to study the behaviour of biochar during gasification aiming to obtain a good knowledge of the reaction mechanisms [10–16]. The reactivity of biochar is closely related to its physical and chemical structures, which change considerably in the course of gasification [4,16–21]. In addition, the changes in the structural features of biochar are greatly affected by the experimental conditions [4,11,14,22–25], especially the temperature [14,26] and gasifying agents [27–30]. For example, gasification with CO_2 would lead to a biochar with a lower content of large aromatic ring systems than the biochar gasified in H_2O [27–30]. It has also been observed that different kinds of O-containing functional groups are formed in biochars derived from gasification under an oxidising atmosphere (e.g. CO_2, H_2O) compared with a reducing atmosphere (e.g. 15% H_2-Ar) [24]. Similarly, the pore structure of biochar also undergoes drastic changes with carbon conversion during gasification [19–21,31,32]. It has been found that the pore structure of biochar from H_2O (steam) gasification is different from that of biochar obtained from CO_2 gasification [32–35]. The different reaction pathways between char-CO_2 and char-H_2O reactions have been widely recognized [24].

Despite the significant progress made in previous studies, the reaction mechanism of biochar gasification remains unclear. In particular, results are inconsistent regarding the effects of H_2O and CO_2 on the porosity development in biochar. Some studies found the maximum micropore development in biochar when subjected to steam gasification [35,36], while others reported that CO_2 gasification resulted in the maximum level of microporosity [32,37–39]. Moreover, the explanation for the different effects of H_2O and CO_2 on the pore development in biochar is not unanimous. Some studies attribute it to the different diffusion coefficients of H_2O and CO_2 arising from their different molecular dimensions [40–42]. Others

believe that it is differences in product (H_2 and CO) inhibition in the C—CO_2 and C—H_2O reactions that cause the different porosity development between biochars gasified in H_2O and CO_2 [43,44]. The porosity in biochar originates from the disordered organisation of the amorphous carbon structures. The pore development of biochar during gasification should be the result of the selective removal of carbon atoms by reacting with gasifying agents. During gasification, with continuous carbon removal and re-arrangement/re-organisation of the carbon matrix, the pore structure evolves simultaneously. However, as far as we know, hardly anyone has correlated the evolution of pore structure in biochar to the transformation in its chemical structure. Furthermore, an agreement has not been met regarding whether there is a synergistic, competitive or additive effect between H_2O and CO_2 during gasification in mixtures of H_2O and CO_2.

Clearly, further studies on the pore development in biochar are needed towards building a better understanding of the reaction mechanism of biochar gasification. A comprehensive analysis of the pore structure evolution in biochar as a consequence of the alteration of the carbon skeleton would provide valuable information in understanding the reaction pathways of biochar gasification.

1.1.3 Biochar as a promising catalyst for tar reforming during gasification

The raw syngas (CO + H_2) from biomass gasification inevitably contains a certain amount of undesirable tar, which is generally defined as the mixture of aromatic hydrocarbons, including large polycyclic aromatic compounds and benzene [45,46]. The presence of tar is considered as the major limitation for the commercialization of biomass gasification technology. Tar compounds are easily condensed, causing the plugging and erosion of the downstream equipment of the gasification system. In addition, the presence of tar contaminants greatly limits the applications of syngas from gasification. For example, a tar concentration of 100 mg m^{-3} in product gas is commonly accepted for a gas engine/ turbine [12]. The maximum tar concentrations for fuel cells and methanol synthesis are 0.001 g Nm^{-3} and 0.1 ppmv respectively [47]. Therefore, the removal of tar to a tolerable limit is a key issue for the successful end-use applications of product gas [4,45]. Moreover, tar removal is crucial for the development and commercialization of gasification technologies.

A great variety of approaches have been used for tar destruction and conversion. The key technologies can be generally classified into physical treatment using wet scrubbers or filters [48], cleaning using plasma [49,50], and thermochemical conversion methods that convert tar into syngas through thermal cracking at high temperature or catalytic reforming employing a catalyst [52–57]. Physical treatment is relatively simple but it requires further treatment for the generated waste liquid (usually water) contaminated with tar [56]. Although plasma assisted tar destruction is effective, it has several disadvantages such as the high cost and the short lifetime of pulsed power devices [49]. Thermal cracking requires high temperatures (> 1100°C) due to the refractory nature of tar [57,58]. Catalytic tar reforming is considered as a technically and economically attractive technique for gas cleaning because such a technique is attractive because it removes tar effectively and simultaneously converts tar into useful gases (H_2, CO and CH_4) [59–63].

Over the years, a wide range of catalysts such as nickel-based [61,64,65] zeolites [66], ilmenites [52,67,68] and alkali metals [58,69] have been employed for catalytic tar elimination. Those catalysts usually have high activities but they are easily deactivated due to coke formation on their surface [58,70,71]. The regeneration and disposal of the catalyst waste is also an issue as they increase the cost of the technology. On the other hand, char, a byproduct from pyrolysis/gasification, shows a high catalytic activity for tar destruction [54,67,72]. It can also be continuously produced inside the gasifier. Furthermore, the deactivated biochar catalyst can be directly burned or gasified without the need for expensive disposal while its energy value is recovered [6,67,73,74]. Therefore, char has attracted great attention to be used as a cost-effective catalyst [23,54,59,67,74–77] for tar removal.

Extensive studies [54,59,72,74] have been carried out to investigate the activity of char catalysts in tar removal, using model tar compounds [78–87] or real tar from the pyrolysis or gasification of biomass/coal/bio-oil [52–54,59,68,73,74]. The catalytic activity of char catalysts has been found to be closely related to the physicochemical properties of char [54] [54,55,74,88] including the surface chemistry, porous structure (large specific surface area), characteristics of inherent alkali and alkaline earth metallic (AAEM) species, as well as the amorphous carbon structure of char [53,74,75]. Despite the great efforts made by researchers, the exact catalytic mechanism of tar reforming over biochar remains unclear, primarily due to the chemical complexity of tar compounds and biochar structure. Particularly, the role of

O-containing functional groups in biochar during the catalytic conversion of tar remains unclear. It has not been clarified what types of O-containing functional groups are important for the catalytic activity of biochar. Furthermore, it remains unclear how these catalytically active O-containing functional groups in biochar might change/evolve during the reforming process.

A full understanding of the mechanism of tar reforming employing biochar as a catalyst requires further study of the correlation between the structural characteristics of activated biochar and its catalytic activity. This understanding would help to optimise the conditions to produce biochar catalysts for tar reforming in commercial gasifiers. This study is part of our ongoing efforts to develop a biochar- based hot gas cleaning system for biomass gasification.

1.2 Thesis objectives

The main objective of this thesis is to understand the reaction mechanisms of biochar gasification as well as the mechanism of tar reforming using biochar as a catalyst. The detailed aims are summarised as follows.

1. To investigate the evolution of the pore structure of biochar during gasification in H_2O, CO_2 and a mixture of H_2O and CO_2 (H_2O/CO_2) using synchrotron small angle X-ray scattering (SAXS) as an *in situ* and *ex situ* characterization technique.
2. To establish a correlation between the changes in the pore structure and the transformations of the chemical structure of biochar in the course of gasification using SAXS, FT-Raman, and X-ray photoelectron spectroscopy (XPS).
3. To study the role of O-containing functional groups in activated biochar in the process of tar reforming over biochar catalysts. Identifying the particular types of O-containing functional groups that are responsible for enhancing the catalytic activity of biochar for tar reforming.
4. To examine the effects of activating agents (H_2O and CO_2) on biochar and the reforming agents (H_2O and CO_2) on the catalytic activities of biochar during tar reforming.

5. To explore the reforming mechanism of tar over a biochar catalyst, particularly the interactions between O-containing functional groups and tar components.

1.3 Thesis outline

This thesis contains eight chapters. Following the introduction, chapter 2 summarizes the materials, experimental setup and methods employed in this project. The next 6 chapters, the main body of this thesis, are based on the six appended peer-reviewed papers and manuscripts. Chapters 3 and 4 are published papers in Carbon [31] and Fuel [32], focusing on the study of the reaction mechanisms of biochar gasification. Chapter 5, 6, and 7 are published papers in Fuel [55–57], focusing on the catalytic tar reforming using biochar as a catalyst. The concluding part, chapter 8, presents the major outcomes of this thesis as well as the recommendations for future work. A brief outline of each chapter from 3 to 7 are given below.

Chapter 3. *In situ SAXS studies of the pore development in biochar during gasification.*

This chapter presents the first *in situ* structural development of the pore network of biochar during gasification under different atmospheres (H_2O, CO_2 and H_2O/CO_2) and temperatures (700, 800 and 900°C). The evolution of specific surface area (SSA), pore volume and size distribution and the fractal features of the porous network of biochar were comprehensively analysed, providing a picture of pore development in biochar during gasification.

Chapter 4. *A SAXS study of the pore structure evolution in biochar during gasification in H_2O, CO_2 and H_2O/CO_2.*

This chapter presents the first correlations between the evolution of pore structure in biochar and the changes in its chemical structure, providing an explanation for the different pore structures produced by H_2O, CO_2 and H_2O/CO_2. The evolution pathway of the pore network in biochar during gasification is given. The pore development in various gasifying agents was found to be paralleled by the evolution of the aromatic structures in biochar. The effects of temperature and biomass particle size on the pore structure of biochar are also included.

Chapter 5. *Role of O-containing functional groups in biochar during the catalytic steam reforming of tar using the biochar as a catalyst.*

This chapter presents the critical role of O-containing functional groups in biochar for improving the efficiency of tar reforming using H_2O-activated biochars as catalysts at 800°C. The evolution of O-containing groups in the biochar catalyst during tar reforming was characterized using FT-Raman and XPS. Steam activation enhanced the catalytic activity of biochar by increasing the content of O-containing functional groups in biochar. The consumption of O-containing functional groups especially the C-O groups in the biochar catalysts was observed.

Chapter 6. *Difference in tar reforming activities between biochar catalysts activated in H_2O and CO_2*.

This chapter presents the different catalytic activities between H_2O-activated biochar and CO_2-activated biochar for tar reforming. The evolution in the biochar structure and tar composition was analysed. The effects of reforming agents (H_2O and/or CO_2) on the tar removal efficiency were also included.

Chapter 7. *Insights into the mechanism of tar reforming using biochar as a catalyst.*

This chapter presents a reforming mechanism of tar over biochar catalyst, taking into consideration the interactions between O-containing functional groups and tar components. The effects of the pore structure of biochar on its catalytic activity was also studied, along with the impacts of biochar on light tar composition and the product gas composition.

1.4 References

[1] Bioenergy IEA. Potential Contribution of Bioenergy to the World's Future Energy Demand 2007.

[2] KLASS DL. Biomass for Renewable Energy, Fuels, and Chemicals. J Environ Qual 2000;29:662–3.

[3] McKendry P. Energy production from biomass (part 1): overview of biomass. Bioresour Technol 2002;83:37–46.

[4] Li C-Z. Importance of volatile-char interactions during the pyrolysis and gasification of low-rank fuels - A review. Fuel 2013;112:609–23.

[5] Sikarwar VS, Zhao M, Clough P, Yao J, Zhong X, Memon MZ, Shah N, Anthony EJ, Fennell PS. An overview of advances in biomass gasification. Energy Environ Sci 2016;9:2939–77.

[6] Li C-Z. Some recent advances in the understanding of the pyrolysis and gasification behaviour of Victorian brown coal. Fuel 2007;86:1664–83.

[7] David Sutton) , Brian Kelleher JRHR. Review of literature on catalysts for biomass gasification

2001:548.

[8] Wu H, Yip K, Tian F, Xie Z, Li C-Z. Evolution of char structure during the steam gasification of biochars produced from the pyrolysis of various mallee biomass components. Ind Eng Chem Res 2009;48:10431–8.

[9] Li C-Z. Special issue—gasification: a route to clean energy. Process Saf Environ Prot 2006;84:407–8.

[10] Kajita M, Kimura T, Norinaga K, Li C-Z, Hayashi JI. Catalytic and noncatalytic mechanisms in steam gasification of char from the pyrolysis of biomass. Energy and Fuels 2010;24:108–16.

[11] Zhang L, Li T, Quyn D, Dong L, Qiu P, Li C-Z. Structural transformation of nascent char during the fast pyrolysis of mallee wood and low-rank coals. Fuel Process Technol 2015;138:390–6.

[12] Dong L, Asadullah M, Zhang S, Wang XS, Wu H, Li C-Z. An advanced biomass gasification technology with integrated catalytic hot gas cleaning Part I. Technology and initial experimental results in a lab-scale facility. Fuel 2013;108:409–16.

[13] Zhang S, Luo Y, Li C, Wang Y. Changes in char reactivity due to char-oxygen and char-steam reactions using victorian brown coal in a fixed-bed reactor. Chinese J Chem Eng 2015;23:321–5.

[14] Keown DM, J-I. H, Li C-Z. Drastic changes in biomass char structure and reactivity upon contact with steam. Fuel 2008;87:1127–32.

[15] Su S, Song Y, Wang Y, Li T, Hu S, Xiang J, Li C-Z. Effects of CO_2 and heating rate on the characteristics of chars prepared in CO_2 and N_2 atmospheres. Fuel 2015;142:243–9.

[16] Bouraoui Z, Jeguirim M, Guizani C, Limousy L, Dupont C, Gadiou R. Thermogravimetric study on the influence of structural, textural and chemical properties of biomass chars on CO_2 gasification reactivity. Energy 2015;88:703–10.

[17] Septien S, Valin S, Peyrot M, Dupont C, Salvador S. Characterization of char and soot from millimetric wood particles pyrolysis in a drop tube reactor between 800 °C and 1400 °C. Fuel 2014;121:216–24.

[18] Di Blasi C. Combustion and gasification rates of lignocellulosic chars. Prog Energy Combust Sci 2009;35:121–40.

[19] Hurt RH, Sarofim AF, Longwell JP. Effect of Nonuniform Surface Reactivity on the Evolution of Pore Structure and Surface-Area During Carbon Gasification. Energy & Fuels 1991;5:463–8.

[20] Wu Z, Wang S, Luo Z, Chen L, Meng H, Zhao J. Physico-chemical properties and gasification reactivity of co-pyrolysis char from different rank of coal blended with lignocellulosic biomass: Effects of the cellulose. Bioresour Technol 2017;235:256–64.

[21] Foster MD, Jensen KF. SAXS investigation of model carbon pore structure and its change with gasification. Carbon N Y 1991;29:271–82.

[22] Zhang L, Kajitani S, Umemoto S, Wang S, Quyn D, Song Y, Li T, Zhang S, Dong L, Li C-Z. Changes in nascent char structure during the gasification of low-rank coals in CO_2. Fuel 2015;158:711–8.

[23] Song Y, Xiang J, Hu S, Quyn DM, Zhao Y, Hu X, Wang Y, Li C-Z. Importance of the aromatic structures in volatiles to the in-situ destruction of nascent tar during the volatile-char interactions. Fuel Process Technol 2015;132:31–8.

[24] Li T, Zhang L, Dong L, Li C-Z. Effects of gasification atmosphere and temperature on char structural evolution during the gasification of Collie sub-bituminous coal. Fuel 2014;117:1190–5.

[25] Keown DM, Li X, Hayashi J-I, Li C-Z. Evolution of biomass char structure during oxidation in O2 as revealed with FT-Raman spectroscopy. Fuel Process Technol 2008;89:1429–35.

[26] Asadullah M, Zhang S, Min Z, Yimsiri P, Li C-Z. Importance of biomass particle size in structural evolution and reactivity of char in steam gasification. Ind Eng Chem Res 2009;48:9858–63.

[27] Tay HL, Kajitani S, Zhang S, Li C-Z. Effects of gasifying agent on the evolution of char structure during the gasification of Victorian brown coal. Fuel 2013;103:22–8.

[28] Tay HL, Li C-Z. Changes in char reactivity and structure during the gasification of a Victorian brown coal: Comparison between gasification in O_2 and CO_2. Fuel Process Technol 2010;91:800–4.

[29] Tay HL, Kajitani S, Zhang S, Li C-Z. Inhibiting and other effects of hydrogen during gasification: Further insights from FT-Raman spectroscopy. Fuel 2014;116:1–6.

[30] Wang S. Evolution of Char Structure and Reactivity during Gasification 2016.

[31] Liu Y, Paskevicius M, Sofianos MV, Parkinson G, Li C-Z. In situ SAXS studies of the pore development in biochar during gasification. Carbon N Y 2021;172:454–62.

[32] Liu Y, Paskevicius M, Sofianos MV, Parkinson G, Wang S, Li C-Z. A SAXS study of the pore structure evolution in biochar during gasification in H_2O, CO_2 and H_2O/CO_2. Fuel 2021;292:120384.

[33] Molina-Sabio M, González MT, Rodriguez-Reinoso F, Sepúlveda-Escribano A. Effect of steam and carbon dioxide activation in the micropore size distribution of activated carbon. Carbon N Y 1996;34:505–9.

[34] Rodríguez-Reinoso F, Molina-Sabio M, González MT. The use of steam and CO_2 as activating agents in the preparation of activated carbons. Carbon N Y 1995;33:15–23.

[35] Coetzee GH, Sakurovs R, Neomagus HWJP, Morpeth L, Everson RC, Mathews JP, Bunt JR. Pore development during gasification of South African inertinite-rich chars evaluated using small angle X-ray scattering. Carbon N Y 2015;95:250–60.

[36] González JF, Encinar JM, González-García CM, Sabio E, Ramiro A, Canito JL, Gañán J. Preparation of activated carbons from used tyres by gasification with steam and carbon dioxide. Appl Surf Sci 2006;252:5999–6004.

[37] Rodríguez-Reinoso F. Controlled gasification of carbon and pore structure development. In: Lahaye J. EP, editor. Fundam. Issues Control Carbon Gasif. React., Springer, Dordrecht; 1991, p. 533–71.

[38] Pastor-Villegas J, Durán-Valle CJ. Pore structure of activated carbons prepared by carbon dioxide and steam activation at different temperatures from extracted rockrose. Carbon N Y 2002;40:397–402.

[39] Gonzalez J, Gonza JF, Roma S, Gonza CM, Ortiz AL, Roma R. Porosity Development in Activated Carbons Prepared from Walnut Shells by Carbon Dioxide or Steam Activation Porosity Development in Activated Carbons Prepared from Walnut Shells by Carbon Dioxide or Steam Activation 2009:7474–81.

[40] Bai Y, Lv P, Yang X, Gao M, Zhu S, Yan L, Li F. Gasification of coal char in H_2O/CO_2 atmospheres: Evolution of surface morphology and pore structure. Fuel 2018;218:236–46.

[41] Alcañiz-Monge J, Cazorla-Amorós D, Linares-Solano A, Yoshida S, Oya A. Effect of the activating gas on tensile strength and pore structure of pitch-based carbon fibres. Carbon N Y 1994;32:1277–83.

[42] González JF, Román S, González-García CM, Nabais JMV, Ortiz AL. Porosity development in

activated carbons prepared from walnut shells by carbon dioxide or steam activation. Ind Eng Chem Res 2009;48:9354.

[43] Wigmans T. Industrial aspects of production and use of activated carbons. Carbon N Y 1989;27:13–22.

[44] Walker PL. Production of activated carbons: use of CO_2 versus H_2O as activating agent. Carbon N Y 1996;34:1297–9.

[45] Pastor AC, Marsh H. Preparation of activated carbon cloths from viscous rayon. Part II : physical activation processes. Carbon N Y 2000;38:379–95.

[46] Dayton D. Review of the literature on catalytic biomass tar destruction; NREL/TP- 510-32815. Golden, CO; NREL; 2002. Natl Renew Energy Lab 2002:28.

[47] Milne TA, Evans RJ, Abatzaglou N. Biomass gasifier "tars": their nature, formation, and conversion. technical report (NREL/TP-570-25357). National Energy Laboratory.The United states. 1998.

[48] Buentello-Montoya DAA, Zhang X, Li J. The use of gasification solid products as catalysts for tar reforming. Renew Sustain Energy Rev 2019;107:399–412.

[49] Paethanom A, Nakahara S, Kobayashi M, Prawisudha P, Yoshikawa K. Performance of tar removal by absorption and adsorption for biomass gasification. Fuel Process Technol 2012;104:144–54.

[50] Nair SA, Pemen AJM, Yan K, Van Gompel FM, Van Leuken HEM, Van Heesch EJM, Ptasinski KJ, Drinkenburg AAH. Tar removal from biomass-derived fuel gas by pulsed corona discharges. Fuel Process Technol 2003;84:161–73.

[51] Tao K, Ohta N, Liu G, Yoneyama Y, Wang T, Tsubaki N. Plasma enhanced catalytic reforming of biomass tar model compound to syngas. Fuel 2013;104:53–7.

[52] Wang Y, Hu X, Song Y, Min Z, Mourant D, Li T, Gunawan R, Li C-Z. Catalytic steam reforming of cellulose-derived compounds using a char-supported iron catalyst. Fuel Process Technol 2013;116:234–40.

[53] Min Z, Asadullah M, Yimsiri P, Zhang S, Wu H, Li C-Z. Catalytic reforming of tar during gasification. Part I. Steam reforming of biomass tar using ilmenite as a catalyst. Fuel 2011;90:1847–54.

[54] Min Z, Zhang S, Yimsiri P, Wang Y, Asadullah M, Li C-Z. Catalytic reforming of tar during gasification. Part IV. Changes in the structure of char in the char-supported iron catalyst during reforming. Fuel 2013;106:858–63.

[55] Liu Y, Paskevicius M, Wang H, Parkinson G, Veder JP, Hu X, Li C-Z. Role of O-containing functional groups in biochar during the catalytic steam reforming of tar using the biochar as a catalyst. Fuel 2019;253:441–8.

[56] Liu Y, Paskevicius M, Wang H, Fushimi C, Parkinson G, Li C-Z. Difference in tar reforming activities between biochar catalysts activated in H_2O and CO_2. Fuel 2020;271:117636.

[57] Liu Y, Paskevicius M, Wang H, Parkinson G, Wei J, M.A A, Li C-Z. Insights into the mechanism of tar reforming using biochar as a catalyst. Fuel 2021;296:120672.

[58] Torres W, Pansare SS, Goodwin JG. Hot gas removal of tars, ammonia, and hydrogen sulfide from biomass gasification gas. Catal Rev - Sci Eng 2007;49:407–56.

[59] Bridgwater A V. The technical and economic feasibility of biomass gasification for power generation. Fuel 1995;74:631–53.

[60] David Sutton , Brian Kelleher, Ross JRH. Review of literature on catalysts for biomass gasification. Fuel Process Technol 2001;101:155–73.

[61] Song Y, Wang Y, Hu X, Xiang J, Hu S, Mourant D, Li T, Wu L, Li C-Z. Effects of volatile-char interactions on in-situ destruction of nascent tar during the pyrolysis and gasification of biomass. Part II. Roles of steam. Fuel 2015;143:555–62.

[62] Li C, Hirabayashi D, Suzuki K. Steam reforming of biomass tar producing H_2-rich gases over $Ni/MgO_x/CaO_{1-x}$ catalyst. Bioresour Technol 2010;101.

[63] Cao JP, Shi P, Zhao XY, Wei XY, Takarada T. Catalytic reforming of volatiles and nitrogen compounds from sewage sludge pyrolysis to clean hydrogen and synthetic gas over a nickel catalyst. Fuel Process Technol 2014;123:34–40.

[64] Yu J, Tian FJ, Chow MC, McKenzie LJ, Li C-Z. Effect of iron on the gasification of Victorian brown coal with steam: Enhancement of hydrogen production. Fuel 2006;85:127–33.

[65] Yu J, Tian FJ, Mckenzie LJ, Li C-Z. Char-supported nano iron catalyst for water-gas-shift reaction hydrogen production from coal/biomass gasification. Process Saf Environ Prot 2006;84:125–30.

[66] Caballero MA, Corella J, Aznar MP, Gil J. Biomass gasification with air in fluidized bed. Hot gas cleanup with selected commercial and full-size nickel-based catalysts. Ind Eng Chem Res 2000;39:1143–54.

[67] Román Galdámez J, García L, Bilbao R. Hydrogen production by steam reforming of bio-oil using coprecipitated Ni-Al catalysts. Acetic acid as a model compound. Energy and Fuels 2005;19:1133–42.

[68] Buchireddy PR, Bricka RM, Rodriguez J, Holmes W. Biomass gasification: Catalytic removal of tars over zeolites and nickel supported zeolites. Energy and Fuels 2010;24:2707–15.

[69] Min Z, Yimsiri P, Asadullah M, Zhang S, Li C-Z. Catalytic reforming of tar during gasification. Part II. Char as a catalyst or as a catalyst support for tar reforming. Fuel 2011;90:2545–52.

[70] Min Z, Yimsiri P, Zhang S, Wang Y, Asadullah M, Li C-Z. Catalytic reforming of tar during gasification. Part III. Effects of feedstock on tar reforming using ilmenite as a catalyst. Fuel 2013;103:950–5.

[71] Mudge LK, Weber SL, Mitchell DH, Sealock LJ, Robertus RJ. Investigations on Catalyzed Steam Gasification of Biomass 1981.

[72] Bridgwater A V. Catalysis in thermal biomass conversion. Appl Catal A, Gen 1994;116:5–47.

[73] Abu El-Rub Z, Bramer EAA, Brem G. Review of catalysts for tar elimination in biomass gasification processes. Ind Eng Chem Res 2004;43:6911–9.

[74] Zhang S, Asadullah M, Dong L, Tay HL, Li C-Z. An advanced biomass gasification technology with integrated catalytic hot gas cleaning. Part II: Tar reforming using char as a catalyst or as a catalyst support. Fuel 2013;112:646–53.

[75] Song Y, Zhao Y, Hu X, Zhang L, Sun S, Li C-Z. Destruction of tar during volatile-char interactions at low temperature. Fuel Process Technol 2018;171:215–22.

[76] Song Y, Wang Y, Hu X, Hu S, Xiang J, Zhang L, Zhang S, Min Z, Li C-Z. Effects of volatile-char interactions on in situ destruction of nascent tar during the pyrolysis and gasification of biomass. Part I. Roles of nascent char. Fuel 2014;122:60–6.

[77] Zhang S, Song Y, Song YC, Yi Q, Dong L, Li TT, Zhang L, Feng J, Li WY, Li C-Z. An advanced biomass gasification technology with integrated catalytic hot gas cleaning. Part III: Effects of inorganic species in char on the reforming of tars from wood and agricultural wastes. Fuel 2016;183:177–

84.

[78] Matsuhara T, Hosokai S, Norinaga K, Matsuoka K, Li C-Z, Hayashi J-I. In-situ reforming of tar from the rapid pyrolysis of a brown coal over char. Energy and Fuels 2010;24:76–83.

[79] Hosokai S, Norinaga K, Kimura T, Nakano M, Li C-Z, Hayashi J-I. Reforming of volatiles from the biomass pyrolysis over charcoal in a sequence of coke deposition and steam gasification of coke. Energy and Fuels 2011;25:5387–93.

[80] Hosokai S, Kumabe K, Ohshita M, Norinaga K, Li C-Z, Hayashi J-I. Mechanism of decomposition of aromatics over charcoal and necessary condition for maintaining its activity. Fuel 2008;87:2914–22.

[81] Lu P, Huang Q, Chi Y, Yan J. Preparation of high catalytic activity biochar from biomass waste for tar conversion. J Anal Appl Pyrolysis 2017;127:47–56.

[82] Ravenni G, Elhami OH, Ahrenfeldt J, Henriksen UB, Neubauer Y. Adsorption and decomposition of tar model compounds over the surface of gasification char and active carbon within the temperature range 250–800 °C. Appl Energy 2019;241:139–51.

[83] Fuentes-Cano D, Gómez-Barea A, Nilsson S, Ollero P. Decomposition kinetics of model tar compounds over chars with different internal structure to model hot tar removal in biomass gasification. Chem Eng J 2013;228:1223–33.

[84] Bhandari PN, Kumar A, Bellmer DD, Huhnke RL. Synthesis and evaluation of biochar-derived catalysts for removal of toluene (model tar) from biomass-generated producer gas. Renew Energy 2014;66:346–53.

[85] Burhenne L, Aicher T. Benzene removal over a fixed bed of wood char: The effect of pyrolysis temperature and activation with CO_2 on the char reactivity. Fuel Process Technol 2014;127:140–8.

[86] Fuentes-Cano D, Parrillo F, Ruoppolo G, Gómez-Barea A, Arena U. The influence of the char internal structure and composition on heterogeneous conversion of naphthalene. Fuel Process Technol 2018;172:125–32.

[87] Hervy M, Weiss-Hortala E, Pham Minh D, Dib H, Villot A, Gérente C, Berhanu S, Chesnaud A, Thorel A, Le Coq L, Nzihou A. Reactivity and deactivation mechanisms of pyrolysis chars from bio-waste during catalytic cracking of tar. Appl Energy 2019;237:487–99.

[88] Klinghoffer NB, Castaldi MJ, Nzihou A. Catalyst properties and catalytic performance of char from biomass gasification. Ind Eng Chem Res 2012;51:13113–22.

[89] Abu El-Rub Z, Bramer EA, Brem G. Experimental comparison of biomass chars with other catalysts for tar reduction. Fuel 2008;87:2243–52.

[90] Moliner R, Suelves I, Lázaro MJ, Moreno O. Thermocatalytic decomposition of methane over activated carbons: Influence of textural properties and surface chemistry. Int J Hydrogen Energy 2005;30:293–300.

Chapter 2

Methodology

2.1 Introduction

This chapter presents the research methodologies employed in this study. The experimental setup and general procedures are detailed described, followed by the approaches that used for the characterization and analysis of samples.

2.2 Experimental set up and general procedures

2.2.1 Sample preparation

Australian Mallee wood was used as feedstock for biomass gasification experiments. The Mallee wood was debarked before being milled into small chips. The wood chips were then sieved to obtain various particle size ranges (0.18−1.0, 1.0−2.0, 2.0−3.35, 3.35−4.0, 4.0−4.75, and 4.75−5.6 mm). The proximate and ultimate analysis of the Mallee wood is shown in *Table* 2. 1.

Table 2. 1. Properties of Mallee wood and bio-oil used in this study.

	Proximate analysis (wt%)		Ultimate analysis (wt%)			
	Volatile matter[b]	Ash[a]	C[b]	O[b,c]	H[b]	N[b]
Mallee wood	81.6	0.9	48.2	45.5	6.1	0.2
Bio-oil	-	-	58.5	34.5	6.7	0.4

[a] Dry basis, [b] dry and ash-free basis, [c] by difference; no Sulphur was detected in Malle wood and bio-oil samples.

The biochar samples (106–250 μm) used in this study were obtained from the the pyrolysis and partial gasification (5–10 min) of Mallee biomass at 750 – 850 °C in Renergi's gasification demonstration plant [1,2].

Bio-oil produced from the pyrolysis of Mallee biomass from the Renergi's grinding pyrolysis pilot plant [22] was used to generate volatiles (including tar) in the tar reforming experiments. The properties of bio-oil are also included in *Table* 2. 1.

2.2.2 Gasification experiments

The gasification of Mallee wood with different particle sizes was carried out using a fluidised-bed quartz reactor. The detailed description of the reactor and the experimental procedure

can be found in references [3,4]. Briefly, a fluidised-bed quartz reactor was placed in a furnace and heated up with argon flowing through the reactor. After the target temperatures (700, 800 or 900 ˚C) were reached, approximately 2 g of Mallee wood was fed into the reactor to commence the pyrolysis of the sample. The reactor was held for 20 mins in argon after the completion of feeding. Afterwards, argon was switched to 15% H_2O/Ar and/or pure CO_2 to proceed the gasification of biochar for 4 min. The reactor was then lifted out of the furnace and cooled down naturally to room temperature in argon before the biochar was collected.

The gasification/activation of biochar (106–250 μm) was performed at 800 ˚C in 15 vol. % H_2O balanced with Ar (named H_2O), pure CO_2 (named CO_2) and/or 15 vol. % H_2O mixed with CO_2 (named H_2O/CO_2) for varying periods (10–50 min). A three-frit two-stage fluidized-bed/fixed bed quartz reactor [5,6] was employed (*Figure* 2. *1*). Briefly, 1 g of biochar was preloaded in the middle frit of the reactor before being heated under argon. After the reactor had stabilised at 800 °C, argon was switched to H_2O, CO_2 or H_2O/CO_2 at a total flow rate of 2.0 L min^{-1} to continue the gasification of biochar for different times. Biochar samples were collected after the reactor had cooled down to room temperature under argon flow.

2.2.3 Tar reforming experiments

The reforming experiments were performed at 800 °C. A three-frit two-stage fluidized-bed/fixed-bed quartz reactor as shown in *Figure* 2. *1*. was used for the catalytic tar reforming experiments [5,6]. The biochar (106–250 μm) was preloaded on the middle frit prior to being heated in argon. After the reactor had stabilized at 800 °C, CO_2 or 15 vol% steam in argon was flowed into the reactor from the bottom at a total flow rate of 2.0 L min^{-1} to *in situ* activate the biochar for different times (10-50 mins). After the activation was finished, CO_2 or 15 vol% steam was switched to the reforming agent, which may be CO_2 or 15 vol % H_2O in argon, while the feeding of bio-oil at 0.20 mL min^{-1} into the reactor with a high performance liquid chromatography (HPLC) pump also commenced simultaneously to begin the dry reforming or steam reforming of tar. Volatiles, including tar, were generated immediately after bio-oil reached the reaction zone at 800 °C. In other words, the tar for reforming, was generated *in situ* from the reactions of bio-oil. It should be noted that, based on the relationships between biochar conversion and activation time that had been experimentally determined separately, the amount of biochar left after activation was controlled to be 1 g [5].

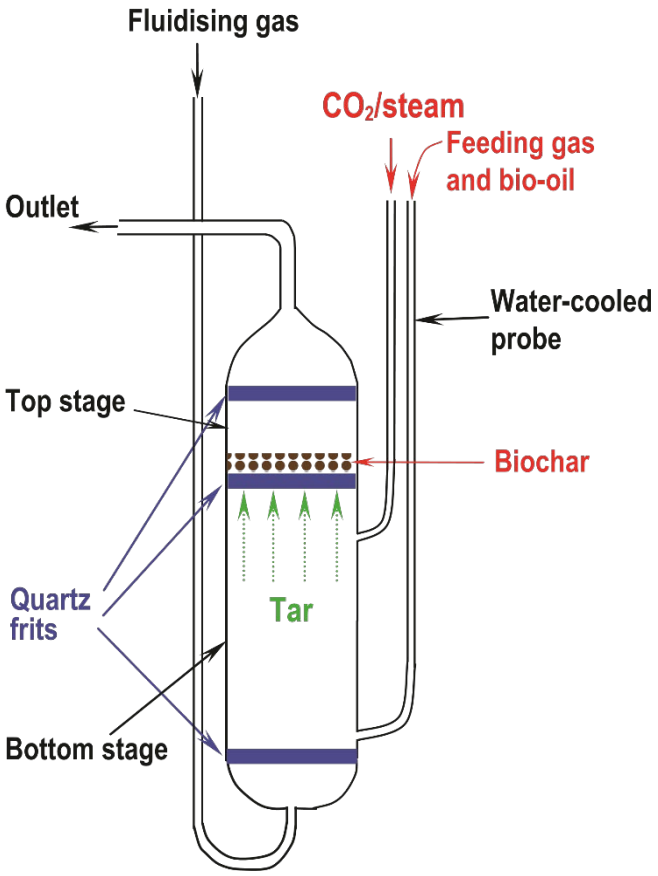

Figure 2. 1. A schematic diagram of the three-frit fluidized-bed/fixed-bed quartz reactor (modified from Ref. [7] with permission from Elsevier).

During reforming, the reactor outlet was connected to a series of three condensation traps to collect the condensable compounds from the outlet stream. These traps were filled with a mixture of HPLC-grade chloroform and methanol (4:1 by vol) [8,9]. When the required reforming time has elapsed, the feeding of bio-oil was stopped and the flow of reforming agent was switched to argon. The reactor was then lifted out of the furnace and cooled down under argon flow. The biochar and tar solutions were then collected for further analysis.

To facilitate comparison, two control experiments were also carried out without using biochar as a catalyst whilst keeping other conditions the same.

2.3 Characterization and analysis of samples

2.3.1 Biochar characterization and analysis

2.3.1.1 FT-Raman spectroscopy

A Perkin–Elmer Spectrum GX FT-IR/Raman spectrometer was used to characterize the structural features of the aromatic ring systems and the O-containing functional groups of biochar. Briefly, 0.25 wt% biochar was mixed with KBr and then ground before being scanned 200 times. Afterwards, the Raman spectrum in the range of 800 - 1800 cm^{-1} was baseline-corrected before being fit with 10 Gaussian bands following our previous procedure [10]. The assigned D band (1300 cm^{-1}) represents the large aromatic ring systems containing 6 or more rings. The G_R (1540 cm^{-1}), V_L (1465 cm^{-1}) and V_R (1380 cm^{-1}) bands correspond to small aromatic ring systems containing 3-5 rings. The band area ratio $I_{(GR+VL+VR)}/I_D$ reflects the relative content of small and large aromatic ring systems. The total Raman peak area in the range of 800 -1800 cm^{-1} was used to indicate the relative amount of O-containing functional groups that, together with their attached aromatic ring systems, can generate a resonance effect.

2.3.1.2 X-ray photoelectron spectroscopy (XPS)

A Kratos AXIS Ultra DLD XPS spectrometer equipped with an Al- Kα X-ray source (energy 1486.7 eV) was used to study the evolution of O-containing functional groups on biochar surface. An XPS survey spectrum was obtained over an energy range from 0 to 1200 eV. High-resolution spectra of C 1s and O 1s were obtained at a pass energy of 40 eV. The CasaXPS software was used to analyse the obtained XPS spectra. The spectra was calibrated using the amorphous C 1s peak at 284.5 eV. After calibration and Shirley background subtraction, the O 1s spectra were curve-fitted following our previous procedure [4]. The aromatic C=O groups and C-O groups were assigned to 531.4 eV and 533.4 eV respectively. The band at 536.0 eV was assigned to the adsorbed oxygen on the biochar surface.

2.3.1.3 Small Angle X-ray Scattering (SAXS)

The pore structure of biochar was characterized using SAXS. *In situ* and *ex situ* SAXS measurements were conducted at the SAXS/WAXS beamline equipped with a Pilatus 1-M

detector at the Australian Synchrotron in Melbourne [11]. The FWHM beam size was 240 µm horizontally and 24 µm vertically. The X-ray transmission (T_s) is measured by recording the incident flux (I_0) and transmitted flux (I_{BS}) using an upstream detector and a detector inside the beamstop respectively.

For the *in situ* measurement (*Figure* 2. 2), biochar sample was loaded into a thin-walled quartz capillary (OD = 1 mm, wall thickness is 0.01 mm) open at both ends and heated under a flow off gasifying agent (H_2O, CO_2 or a mixture of them). During this process, SAXS data were collected with a one second time resolution for 60 min or until the biochar was fully consumed. The *in situ* data was collected at a camera length of 959 mm, which corresponds to a *q*-range of 0.03-1.5 Å^{-1} (q is the scattering vector $q = (4\pi/\lambda)\sin(\theta/2)$, λ (0.62 Å) and θ are the wavelength and scattering angle) [12]. The background scattering from the capillary was subtracted using a single measurement of an empty capillary.

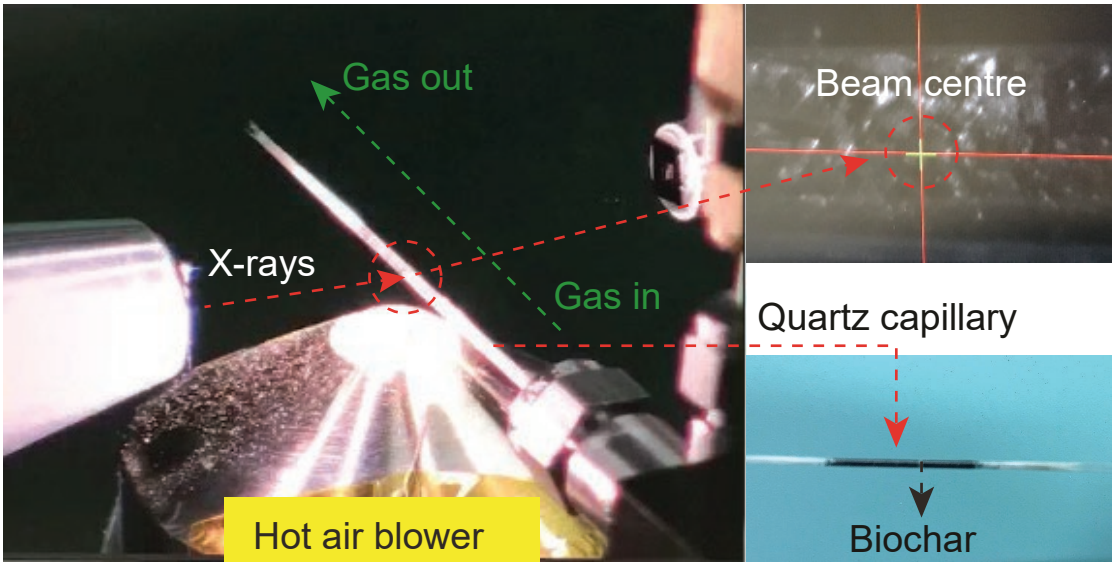

Figure 2. 2. Diagram showing the experimental set-up in place on the SAXS beamline at the Australian Synchrotron.

For the *ex situ* measurement, biochar samples were mounted in square holes (4 x 4 mm) in a 2-mm-thick stainless steel plate with Kapton tape covering both sides, as shown in *Figure* 2. 3. All samples were measured at two camera lengths (3343 mm and 959 mm) to achieve a wide *q*-range from 0.005 to 1.5 Å^{-1}, respectively, which are appropriate to probe a pore diameter ranging approximately from 0.4 to 125 nm. A scattering background from Kapton tape was measured and subtracted from all data sets. Silver behenate was used to

calibrate the *q*-scale of the instrument, and a 1 mm thick glassy carbon standard was used for absolute intensity calibration [13].

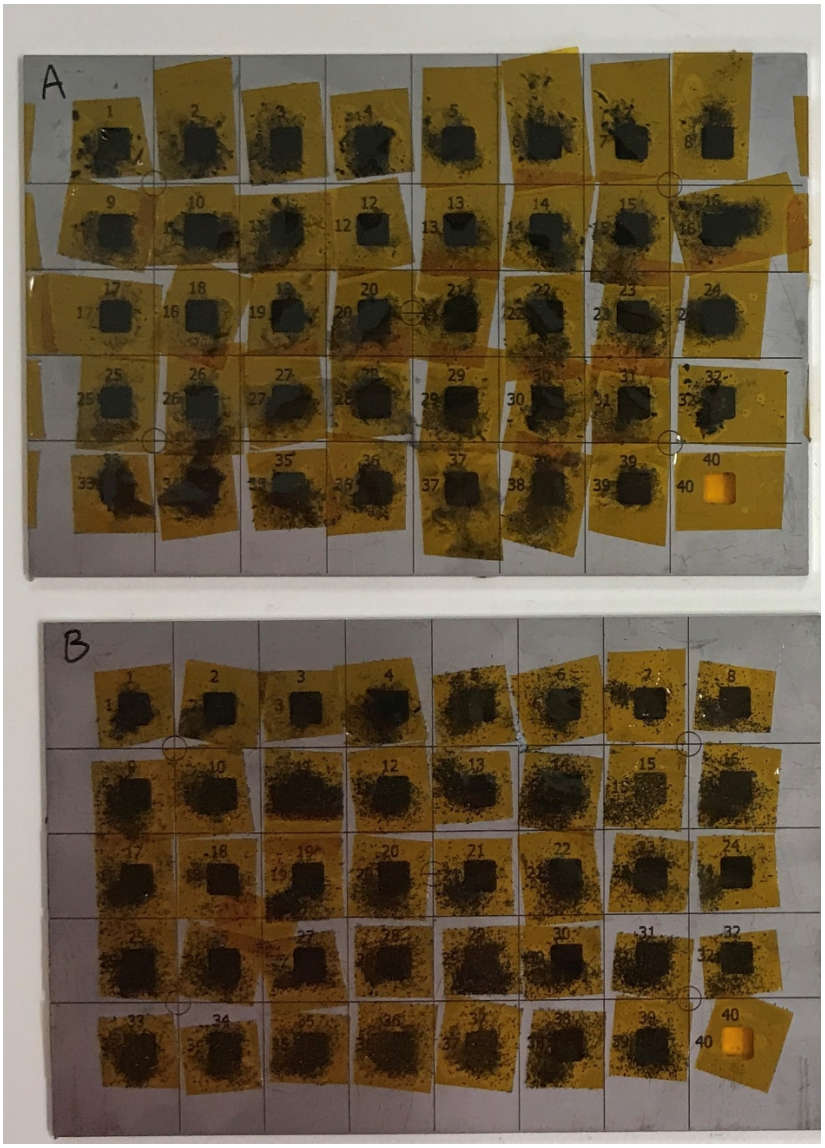

Figure 2. 3. Biochar samples loaded into 2-mm-thick sample plate and fixed to the plate using Kapton tape for the SAXS testing.

2.3.2 Tar analysis

2.3.2.1 Tar yield

As described previously [8,14,15], tar yield was determined by measuring the concentration of tar dissolved in a chloroform/methanol solvent trap. Tar is experimentally defined as the

material soluble in the chloroform/methanol mixture that does not evaporate at 35 °C within 4 h. A blank experiment was also carried out to exclude the non-evaporative residues in the solvents themselves. Tar yield is defined as the ratio of the amount of tar to the amount of bio-oil used in the experiments.

2.3.2.2 UV-fluorescence spectroscopy

A UV-fluorescence spectroscopy (Perkin-Elmer LS50B spectrometer) was used to characterize the collected tar samples. The synchronous spectra were recorded with a slit width of 2.5 nm and a scan speed of 200 nm min^{-1} at a constant energy difference of -2800 cm^{-1}. Before characterization, the tar solutions were diluted with methanol (Uvasol for spectroscopy; purity: 99.9% by GC) to 4 ppm (by weight).

2.3.2.3 GC-MS

Tar samples were also analysed using an Agilent GC–MS (a 6890 series GC plus a 5973 MS detector) with helium as the carrier gas. Detailed parameters of the measurement can be found elsewhere [20,21]. The detected compounds corresponding to each ion peak were identified based on the standard spectra of compounds in the National Institute of Standards and Technology (NIST) library and/or the spectra of known species injected.

2.3.3 Gas composition analysis

The product gases were on-line analysed by a QMS Prisma™ 200 MS. The instrument was calibrated using a certified calibration standard (ISO Guide 34 accredited) gas mixtures. The molar/volume ratios of H_2, CO, CO_2, and CH_4 were calculated respectively after calibration as described previously [17].

2.5 References

[1] Advanced biomass gasification technology, Australian Renewable Energy Agency.

[2] Grinding pyrolysis, Renergi Pty Ltd. http://www.renergi.net/grinding_pyrolysis. (accessed December 20, 2020).

[3] Wang S, Wu L, Hu X, Zhang L, Li T, Li C-Z. Effects of the particle size and gasification atmosphere on the changes in the char structure during the gasification of mallee biomass. Energy and Fuels 2018;32:7678–84.

[4] Wang S, Wu L, Hu X, Zhang L, O'Donnell KM, Buckley CE, Li C-Z. An X-ray photoelectron spectroscopic perspective for the evolution of O-containing structures in char during gasification. Fuel Process Technol 2018;172:209–15.

[5] Liu Y, Paskevicius M, Wang H, Parkinson G, Veder JP, Hu X, Li C-Z. Role of O-containing functional groups in biochar during the catalytic steam reforming of tar using the biochar as a catalyst. Fuel 2019;253:441–8.

[6] Liu Y, Paskevicius M, Wang H, Fushimi C, Parkinson G, Li C-Z. Difference in tar reforming activities between biochar catalysts activated in H_2O and CO_2. Fuel 2020;271:117636.

[7] Wu H, Quyn DM, Li C-Z. Volatilisation and catalytic effects of alkali and alkaline earth metallic species during the pyrolysis and gasification of Victorian brown coal. Part III. The importance of the interactions between volatiles and char at high temperature. Fuel 2002;81:1033–9.

[8] Min Z, Asadullah M, Yimsiri P, Zhang S, Wu H, Li C-Z. Catalytic reforming of tar during gasification. Part I. Steam reforming of biomass tar using ilmenite as a catalyst. Fuel 2011;90:1847–54.

[9] Jiang S, Hu X, Xia D, Li C-Z. Formation of aromatic ring structures during the thermal treatment of mallee wood cylinders at low temperature. Appl Energy 2016;183:542–51.

[10] Li X, Hayashi J-I, Li C-Z. Volatilisation and catalytic effects of alkali and alkaline earth metallic species during the pyrolysis and gasification of Victorian brown coal. Part VII. Raman spectroscopic study on the changes in char structure during the catalytic gasification in air. Fuel 2006;85:1509–17.

[11] Kirby NM, Mudie ST, Hawley AM, Cookson DJ, Mertens HDT, Cowieson N, Samardzic-Boban V. A low-background-intensity focusing small-angle X-ray scattering undulator beamline. J Appl Crystallogr 2013;46:1670–80.

[12] Glatter O, Kratky O. Small angle x-ray scattering. 1982.

[13] Dreiss CA, Jack KS, Parker AP. On the absolute calibration of bench-top small-angle X-ray scattering instruments: A comparison of different standard methods. J Appl Crystallogr 2006;39:32–8.

[14] Min Z, Yimsiri P, Zhang S, Wang Y, Asadullah M, Li C-Z. Catalytic reforming of tar during gasification. Part III. Effects of feedstock on tar reforming using ilmenite as a catalyst. Fuel 2013;103:950–5.

[15] Sathe C, Pang Y, Li C-Z. Effects of heating rate and ion-exchangeable cations on the pyrolysis yields from a Victorian brown coal. Energy and Fuels 1999;13:748–55.

[16] Wang Y, Hu X, Mourant D, Song Y, Zhang L, Lievens C, Xiang J, Li C-Z. Evolution of aromatic structures during the reforming of bio-oil: Importance of the interactions among bio-oil components. Fuel 2013;111:805–12.

[17] Wang Y, Li X, Mourant D, Gunawan R, Zhang S, Li C-Z. Formation of aromatic structures during the pyrolysis of bio-oil. Energy and Fuels 2012;26:241–7.

[18] Akhtar MA, Zhang S, Shao X, Dang H, Liu Y, Li T, Zhang L, Li C-Z. Kinetic compensation effects in the chemical reaction-controlled regime and mass transfer-controlled regime during the gasification of biochar in O2. Fuel Process Technol 2018;181:25–32.

Chapter 3

In situ SAXS studies of the pore development in biochar during gasification

Y. Liu, M. Paskevicius, M.V. Sofianos, G. Parkinson, C.-Z. Li, In situ SAXS studies of the pore development in biochar during gasification, Carbon, N Y 2021;172:454–62. https://doi.org/10.1016/j.carbon.2020.10.028.

Abstract

This work investigates the pore development in biochar during gasification using synchrotron small angle X-ray scattering (SAXS) as an *in situ* characterization technique. The influence of the gasifying agents (H_2O, CO_2 or H_2O/CO_2) and temperature on the pore structure development in biochar was studied by carrying out the hour-long gasification of mallee wood biochar (106–250 µm) in: (i) H_2O at 700, 800 and 900°C respectively, (ii) CO_2 at 700 and 800°C, and (iii) a mixture of H_2O and CO_2 (H_2O/CO_2) at 800°C. There was a minor increase in the micro- and mesopore volumes in biochar during gasification in H_2O at 700°C, in contrast to CO_2 gasification at the same temperature where no measurable changes to the pore structure were observed. At 800°C, biochar derived from H_2O/CO_2 gasification exhibited the highest specific surface area (SSA). CO_2 tended to produce a highly microporous biochar with a mesopore network showing pore fractal features. Micropore enlargement was a major process in the presence of H_2O. In this case, the pore structure evolved from being a porous network of branched micropore clusters (pore fractal) to being dominated by rough surfaced mesopores (surface fractal) during gasification in H_2O and H_2O/CO_2. The evolution of pore structures resulted from the different ways in which carbon atoms were removed by either H_2O or CO_2. H_2O is more reactive and less selective towards reacting with biochar, resulting in a less worm-like network of pores than CO_2. Moreover, it was found that increasing temperatures can lead to faster rates of pore generation and pore enlargement, which is attributed to the increased reaction rate and the less selective removal of carbon atoms.

3.1 Introduction

Biomass, as a widely available and carbon neutral resource, plays an important role in supplying clean and affordable energy. Gasification is a highly efficient technology to utilize biomass for power generation, as well as for the production of biofuels and chemicals [1]. Biomass gasification is a thermo-chemical process to convert biomass to syngas and biochar [2]. During gasification, biochar reacts with the gasifying agents and undergoes drastic changes in both its chemical and physical structure [3,4]. The study of pore evolution in biochar during gasification is critical to understanding the gasification process, as well as to

optimizing the conditions that are used for the preparation of activated carbon using biochar as a precursor [5–8].

It has been reported [9–12] that the pore structure of biochar largely depends on the gasification conditions such as the biomass feedstocks, the gasifying agents and the carbon conversion level. Particularly, the pore structure of biochar from H_2O (steam) gasification has been found to be different from that of biochar obtained from CO_2 gasification [5,10,11,13]. However, different results have been obtained regarding the effects of steam and CO_2 on the porosity development in biochar. Some studies found the maximum micropore development in biochar when subjected to steam gasification [10,14], while others reported that CO_2 gasification resulted in the maximum level of microporosity [6,13,15,16]. Additionally, it has not reached an agreement regarding whether there is a synergistic, competitive or additive effect between H_2O and CO_2 during gasification in the mixture of H_2O and CO_2.

Those reported results are based on measurements using a wide range of techniques including N_2 adsorption (BET), scanning and transmission electron microscopy (SEM and TEM), as well as SAXS and small angle neutron scattering (SANS). Among these techniques, SAXS has been historically utilized to characterize the porosity and the pore morphology of coal and porous carbon with the advantage of detecting both closed and open pores over wide dimension ranges [11,17–23]. Moreover, SAXS can provide the textural properties (e.g. surface roughness or aggregation) of biochar by giving fractal information of the pore network [24–27]. The development of the pore network reflects the evolution of the carbon matrix during gasification, which depends on the reaction pathways of gasification. Therefore, the evolution in the porous network of biochar is of great importance for understanding the reaction pathways during gasification. However, little has been reported on the evolution of the porous network of biochar along gasification. Moreover, *in situ* SAXS is capable of tracking the real-time changes of pore structure under high temperatures throughout the process of gasification. In this way, the *in situ* SAXS measurement avoids the possible changes in biochar structure during cooling down, which can be a shortcoming of *ex situ* measurements. To the best of our knowledge, no *in situ* SAXS measurements of this kind have been previously performed.

To this end, this study uses synchrotron SAXS to characterize the real-time evolution of the pore structure of biochar during gasification. Gasifying agents including H_2O, CO_2 and

their mixture were used with the aim of studying the effects of different gasifying agents on the pore development of biochar. The influence of gasification temperature (700, 800 and 900°C) on the development of pores in biochar was also investigated.

3.2 Experimental

3.2.1 In situ SAXS measurement

In situ SAXS measurements were conducted at the SAXS beamline of the Australian Synchrotron, Melbourne, Australia [28]. The X-ray beam energy and size was 20 keV and 240 (horizontally) X 24 (vertically) µm respectively. Data were acquired using a Pilatus 1 M detector at a camera length of 959 mm, which corresponds to a *q*-range of 0.03-1.5 $Å^{-1}$ (*q* is the scattering vector $q = (4\pi/\lambda)\sin(\theta/2)$, λ (0.62 Å) and θ are the wavelength and scattering angle) [29]. The *q* range approximately corresponds to observing a pore diameter ranging from 4 to 180 Å [29]. The SAXS patterns were acquired every 1 s during gasification. Silver behenate was used to calibrate the *q*-scale of the instrument, and a 1 mm thick glassy carbon standard was used for absolute intensity calibration [30]. The background scattering from the capillary was subtracted using a single measurement of an empty capillary.

3.2.2 Experimental set-up

The biochar (106-250 µm) used in this study is from the pyrolysis and gasification of mallee wood in Renergi's gasification demonstration plant at Curtin University, Australia [31,32]. The biochar precursor was loaded into a thin-walled quartz capillary (OD = 1 mm, wall thickness is 0.01 mm) open at both ends. Quartz wool was firmly inserted at both sides of the biochar to prevent sample displacement while allowing gas flow through the samples (*Figure* 3. *1*). A total of 3 different gasifying gases including steam (3 vol. % H_2O in argon), pure CO_2 and a mixture of steam and CO_2 (3 vol. % H_2O in CO_2) were used in this study. Steam was generated by flowing argon or CO_2 through 2 connected gas washing bottles that contained DI water (a 100% relative humidity at room temperature gives a ~3 vol. % steam at 800-900 °C). Gas was flowed through the sample from one end to another of the capillary with a flow rate of 10 ml min^{-1} controlled by a mass flow controller (Alicat MC).

Biochar samples were heated to operating temperature under an argon flow before switching to the prescribed gasifying agent. During this process, SAXS data were collected for 60 min or until the biochar was fully consumed. It should also be mentioned that one data set was collected during the heating of biochar up to 900°C in pure argon, where no changes in the scattering intensities were observed to verify that the pore network does not change under these conditions. The heating of biochar was achieved by placing a hot-air blower underneath the capillary, which can provide a uniform heating of the sample in the X-ray beam. A K-type thermocouple was placed on the outside of the capillary and fixed next to the sample in the beam to accurately measure the temperature. All the experiments were operated under ambient pressure.

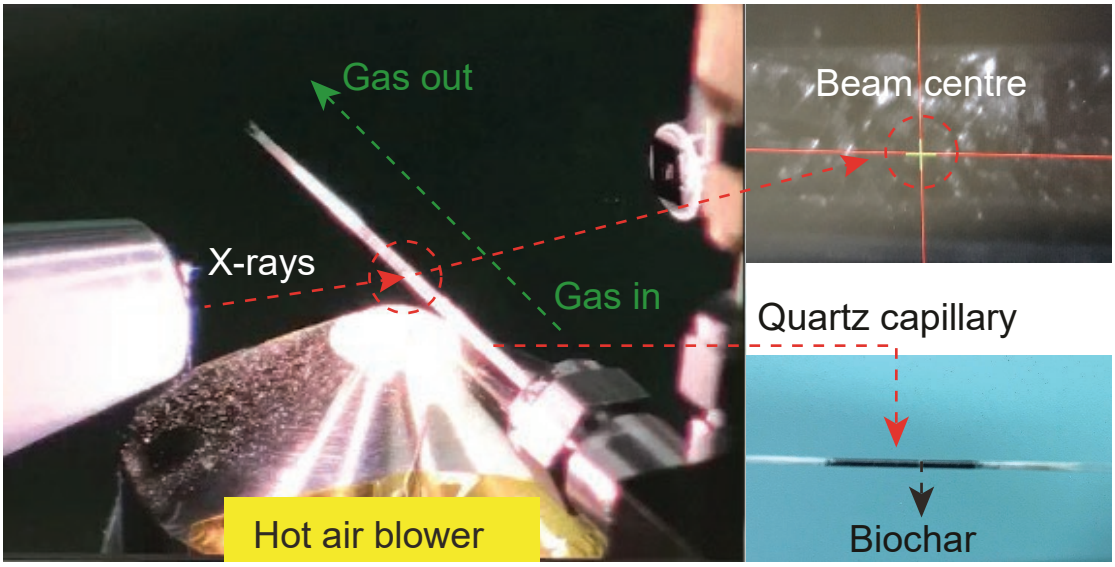

Figure 3. 1. Diagram showing the experimental set-up in place on the SAXS beamline at the Australian Synchrotron.

3.2.3 Data processing

The collected SAXS patterns were background subtracted using Scatterbrain [33,34] before being converted to an absolute scale by normalising the intensity by the sample thickness with reference to a known glassy carbon standard [35]. The solid thickness of the sample was calculated using Eq. (3.1), which is described elsewhere [35].

$$d = -\ln(T_s)/\mu \qquad (3.1)$$

where, d is the solid thickness of sample, T_s is the X-ray transmission that is measured by recording the incident flux (I_0) and transmitted flux (I_{BS}) using an upstream detector and a detector inside the beamstop respectively. μ is the linear adsorption coefficient of the sample (the density of 2.0 g cm^{-3} for amorphous carbon was used for the calculation).

SAXS data were interpreted to solely originate from the dominant scatterer within the sample, which was deemed to be the electron density difference due to porosity on the micro- and meso- length scale. It should be noted that the analysis of fractal power-law regimes within the SAXS data is limited to the q-range of the data but it has been interpreted as a representation of either rough pore surfaces or pore fractals based on its dimensionality.

The normalised SAXS patterns were then processed using the Irena package for Igor Pro (WaveMetrics) [36]. The Unified model [37] was used to fit the scattering patterns as it can describe the structural features of complex systems containing multiple structural levels. The Unified equation for one structural level combines a Guinier law and a structurally limited power law [37], as shown in Eq. (3.1).

$$I(q) = G\exp\left(-\frac{q^2R_g^2}{3}\right) + B(q^*)^{-P}, \quad q^* = \frac{q}{[\mathrm{erf}\,(qR_g/\sqrt{6})]^{-3}} \qquad (3.2)$$

where $I(q)$ is the scattering intensity, erf( ) is the error function. G and B are the prefactors from the Guinier and power law regions respectively. R_g is the radius of gyration of the scattering objects, the pores in this case, and P is the scattering exponent. A detailed description of the parameters can be found in ref [37]. The extracted R_g and P from each structural level provide information on the size and the morphology of the pores. If we assume the pores are spherical, their radius can be calculated by $r = \sqrt{5/3}\ R_g$. The power law slope given by P provides information about the fractal dimension of the pores and/or their network [26,38]. Generally, for surface fractals $4 > P > 3$ and the fractal dimension $D_s = -P + 6$. A smooth surface corresponds to $D_s = 2$ and the surface roughness increases with increasing D_s. For mass or pore fractals $P < 3$ and the fractal dimensions $D_m = D_p = P$. Pore fractal can be viewed as the negative image of mass fractal. The pore fractal dimension (D_p) describes the space-filling and branching properties of pores in a structure [26].

The specific surface area (S) was calculated (Eq. 3.3) using the parameters extracted from the unified fit [38,39].

$$S(r) = Sr^{2-D_S} \quad (3.3)$$

where *r* is the size of the 'measurement stick' for which 4 Å (the size of a nitrogen molecule) was used, and *S* is given by:

$$S = 2\pi\varphi(1-\varphi)B/Q\rho_{bulk}F(D_s) \quad (3.4)$$

where *F*(*Ds*), the mass fraction *φ* and the high-*q* invariant *Q* are given by the following:

$$F(D_s) = \Gamma(5-D_s)\sin[\pi(3-D_s)/2]/(3-D_s) \quad (3.5)$$

$$\varphi = \rho_{bulk}/\rho_{base\ material} \quad (3.6)$$

$$Q = \int_0^\infty I(q)q^2dq = 2\pi^2G/V_p \quad (3.7)$$

Where ρ_{bulk} and $\rho_{base\ material}$ are the bulk density (see ref. [40] for the calculation) and the primary particle density (2.0 g cm^{-3}) of sample, V_p is the volume of the primary particles (pores in our case).

The pore size distribution was determined using the IPG/TNNLS (Internal Point Gradient-Total Non-Negative Least Square) fitting method in Irena [36]. This model provides a size distribution assuming a dilute dispersion of scattering features, but has been verified to provide accurate size distributions even for scattering features that demonstrate fractal aggregation [41].

3.3 Results and discussion

3.3.1 Pore development of biochar gasification at 800 °C in H_2O, CO_2 and H_2O/CO_2.

3.3.1.1 In situ SAXS patterns of biochar during gasification

Figure 3. *2* shows the SAXS patterns of biochar during gasification for 60 min at 800 °C in (a) H_2O, (b) CO_2, and (c) H_2O/CO_2 mixture. The scattering intensity *I*(*q*) was plotted on log-log scale and the scattering intensities are on an absolute scale. The sequences of scattering patterns represent the changes in the scatterers (pores in our case) from the beginning of the gasification (blue line in graph) until after 60 min of reaction (red line). The intensities (*I*) as a function of the scattering vector (*q*) are due to X-rays scattered from the electron density difference between the carbon matrix and the empty pores (the scattering from the gases

used in experiments is negligible) at various length scales [29]. The intensities in the high q region (roughly $q > 0.3$ Å^{-1}) correspond to the features of micropores (pore diameter less than 20 Å). Similarly, intensities in the low q region (roughly $q < 0.3$ Å^{-1}) reflect scattering from mesopores (pore diameter between 20 and 500 Å). The increase or decrease in the scattering intensity shows the general growth or reduction of the specific surface area (SSA) and/or volume from micro- (high q) and mesopores (low q).

For all the biochars gasified (in H_2O, CO_2 or H_2O/CO_2) at 800°C, there are obvious changes in the SAXS intensities throughout the gasification process, reflecting the transformations in the pore structure over time. There is a clear increase in the intensities at low q as the gasification progresses, indicating that the volume fraction of mesopores steadily increases over time. There are also differences in the increase of intensities at low q among the three gasifying agents, indicating the differences in the mesopore development in biochar during gasification in different gasifying agents. As for the intensities at high q, a slight decrease is observed as the conversion proceeds. During gasification in H_2O/CO_2, the intensities at q higher than 0.2 Å^{-1} decreased with increasing time, implying the reduction of the micropore volume. Also, the intensity decrease is more significant in H_2O/CO_2 than any in either H_2O or CO_2 alone. The reactions occuring on the size scale of the micropores appear to be enhanced by the presence of both H_2O and CO_2. The differences in the SAXS patterns among different gasifying agents show the differences in pore development in biochar gasified in different gases.

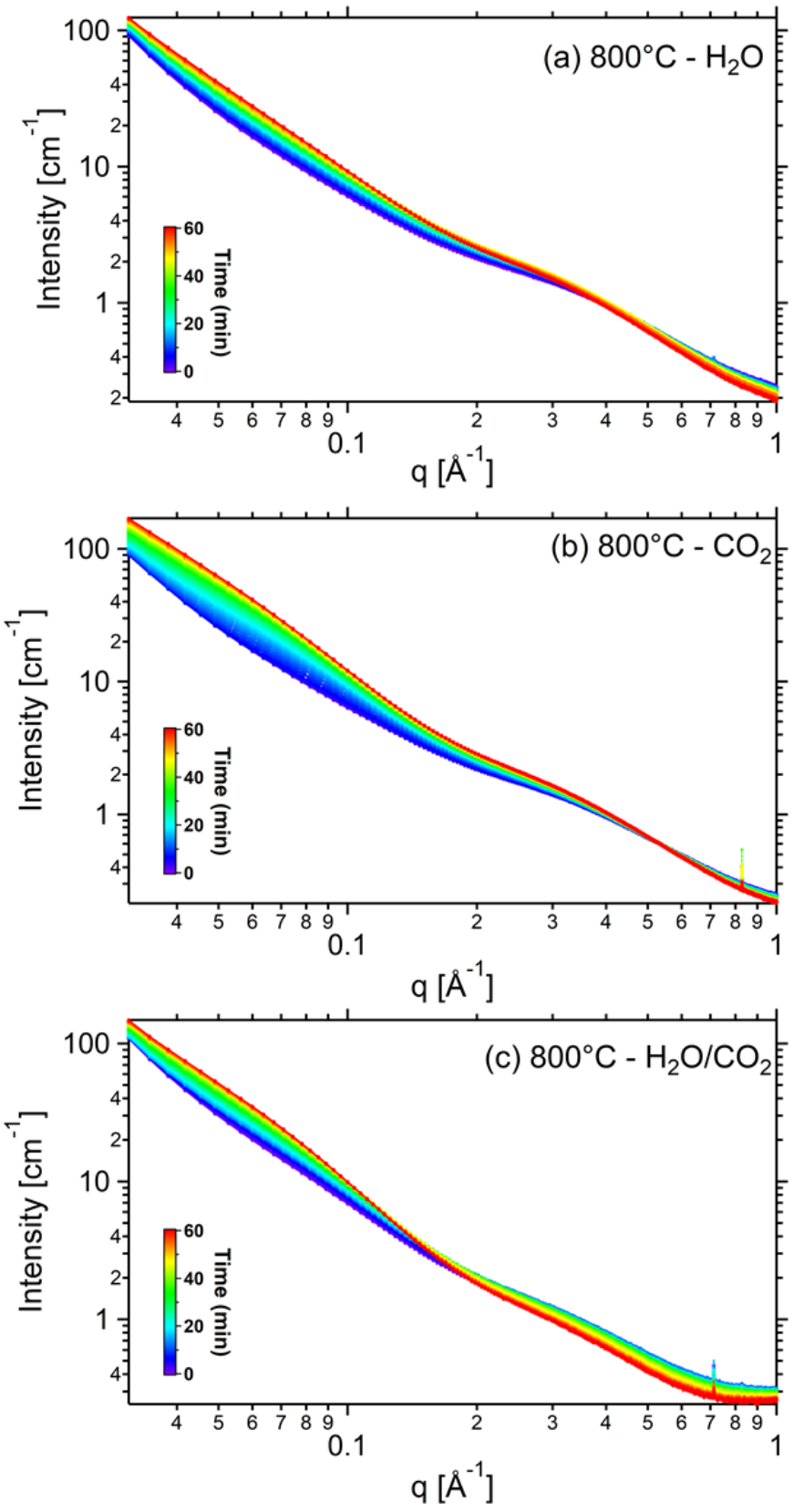

Figure 3. 2. Time-resolved SAXS patterns of biochar during gasification in (a) H_2O, (b) CO_2 and (c) H_2O/CO_2 at 800°C. The SAXS curves were plotted on linear time scale.

3.3.1.2 SAXS analysis

Before further analysis, it should be pointed out that the porosity in biochar originates from the disordered organisation of the amorphous carbon structures. The pore development of biochar during gasification is the result of the selective removal of carbon atoms by reacting with gasifying agents. During gasification, some ultramicropores (pore size is smaller than 10 Å) will be created when some carbon atoms are selectively removed by H_2O or CO_2. The initially created ultramicropores allow the next H_2O or CO_2 molecules to enter into the pore and to continue attacking the next carbon site. In this way, an abundance of micropores will be generated in the process.

In the case of gasification in the mixture of H_2O and CO_2, both of H_2O and CO_2 molecules could access the micropores initially created either by H_2O or CO_2. This is reasonable as the molecular size of H_2O (2.75 Å) and CO_2 (3.3 Å) is much smaller than the size of micropores if they are part of an open-pore (not closed-pore) network. With the continuous removal of the interior micropore walls, micropores may turn into meso- and macropores. Additionally, pore enlargement and coalescence will also occur when reactions take place on the pore walls or if the wall between pores is consumed. However, new micropores may also be created simultaneously. Therefore, the pore distribution in biochar observed at any point is the net result of pore generation, pore enlargement, and pore coalescence that occur simultaneously during gasification. For example, when the rate of micropore generation is slower than the rate of micropore enlargement and/or coalescence, a reduction in micropores and an increase in mesopores would occur.

To analyse better the pore development of biochar, we selected a few datasets (gasification for 0, 10, 20, 30, 40, 50 and 60 min) and performed a fit to the data using the Unified model [37]. Two structural levels were used in this study that represent the scattering from the (1 – high q) microporous and (2 – low q) mesoporous size regimes. As shown in *Figure* 3. *3*, the first structural level at high q contains a Guinier region (presenting as a hump) and a following power law region (linear on a log-log plot). The Guinier region represents the average size of micropores (d_{micro}) and the slope of the power law region at high q (not shown) gives information on the texture of micropores [37,38]. To get a stable fit to the data we had to assume that the micropore surface was smooth and thus fixed the slope of the high q power law region at 4. This is also reasonable on this length-scale (sub-20 Å) due to the limited

possibilities for roughness when C-C bonds are approximately 1.5 Å. Due to the limited *q* range, we do not see a Guinier regime from mesopores, which would exist at even lower *q*. As a result, the second structural level at low *q* only covers a power law region (*P*, green line), giving fractal information from the mesopore size regime. As such, the average size of mesopores, as well as an accurate mesopore volume, is not able to be extracted from the data. Measurements covering a wider *q* range will be conducted in future work.

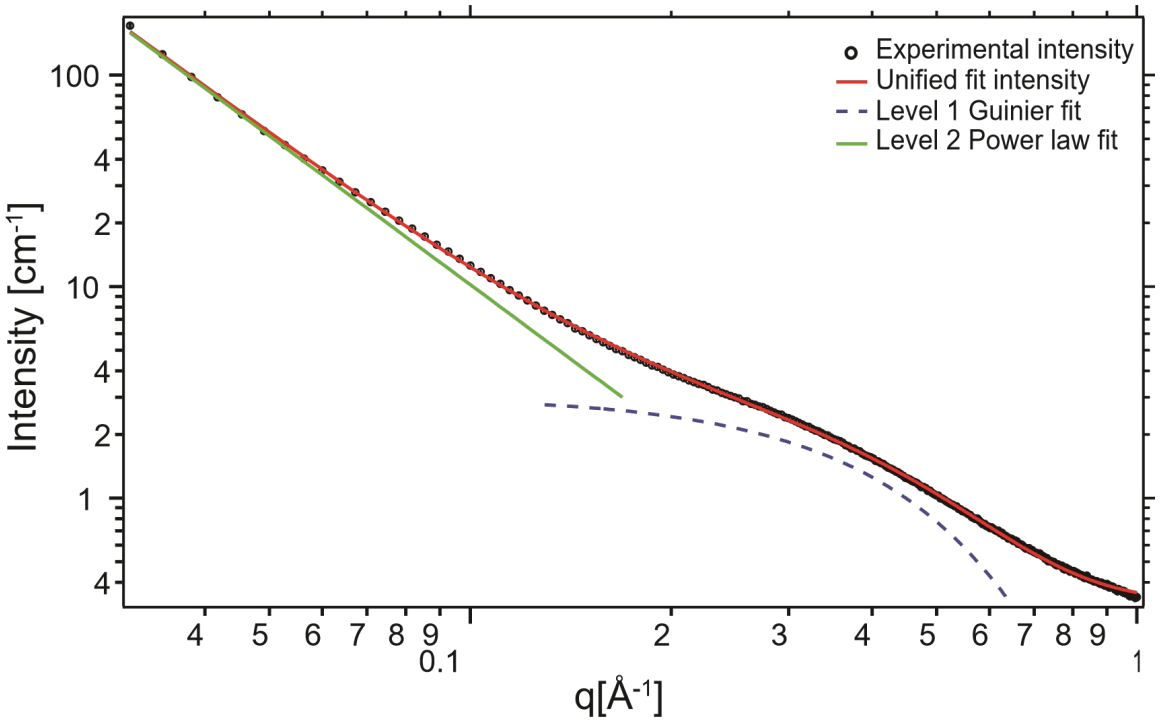

Figure 3. 3. A representative set of SAXS data (black circles) and a two-level unified model (red line) reproduces the experimental data.

The derived parameters from the refined unified model are shown in *Table 3. 1*. The overall average diameter of micropores (d_{micro}) in the gasified biochar was calculated to be around 10 Å. Additionally, in the three data series, the average size of the micropores gradually increased over time during gasification. This demonstrates the occurrence of widening of micropores during gasification. The increase in the size of micropores was more rapid with reaction time in the case of mixed gas H_2O/CO_2 gasification compared to that in the case of H_2O or CO_2 gasification. This could be due to the enhanced removal of the interior

micropore walls as both H_2O and CO_2 molecules can penetrate into the micropores initially created by H_2O or CO_2.

Table 3. 1. Derived average diameter of micropores (d_{micro}), micropore volume (V_{micro}), fractal dimension (D_p, D_s) and SSA from the two-level unified fit of SAXS patterns for biochar gasified in H_2O, CO_2 and H_2O/CO_2 at 800°C for different times (10–60 min).

	0 min	10 min	20 min	30 min	40 min	50 min	60 min
H_2O							
d_{micro} (± 0.5 Å)	9.8	9.9	10.4	10.9	11.1	11.3	12.0
V_{micro} (± 0.01 cm^3/g)	0.19	0.20	0.20	0.20	0.20	0.20	0.19
Fractal dimension (± 0.05)	D_p = 2.4	D_p = 2.4	D_p = 2.7	D_p = 2.9	D_s = 3.0	D_s = 3.0	D_s = 3.1
SSA (± 1 m^2/g)	106	122	139	154	166	179	195
CO_2							
d_{micro} (± 0.5 Å)	10.1	10.5	10.6	10.7	10.8	10.9	11.0
V_{micro} (±0.01 cm^3/g)	0.18	0.20	0.21	0.21	0.21	0.21	0.22
Fractal dimension (± 0.05)	D_p = 2.4	D_p = 2.4	D_p = 2.4	D_p = 2.4	D_p = 2.5	D_p = 2.6	D_p = 2.7
SSA (± 1 m^2/g)	106	188	212	215	218	216	215
H_2O/CO_2							
d_{micro} (± 0.5 Å)	10.1	11.6	11.7	12.0	12.3	12.8	13.3
V_{micro} (±0.01 cm^3/g)	0.19	0.19	0.20	0.20	0.19	0.17	0.15
Fractal dimension (± 0.05)	D_p = 2.4	D_p = 2.5	D_p = 2.7	D_p = 2.9	D_s = 3.1	D_s = 3.3	D_s = 3.4
SSA (± 1 m^2/g)	107	127	182	205	211	232	250

Note: the average diameter of micropores was calculated by assuming the pores are spherical. For surface fractal, $D_s = -P + 6$ and for pore fractal, $D_p = P$.

When the gasification time was extended from 10 to 60 min, the micropore volume (V_{micro}) decreased slightly for the biochar gasified in H_2O and H_2O/CO_2. The decrease is more evident for biochar gasified in H_2O/CO_2. On the contrary, an insignificant increase of the

micropore volume was observed in biochar gasified with CO_2. The subtle changes in the micropore volume coincide with the slight variations in the SAXS intensity at high *q* observed from *Figure* 3. *2*. The micropore development during gasification with H_2O and H_2O/CO_2 presents a relatively constant and slightly decreased micropore volume over time, suggesting a decrease in the quantity of micropores to compensate for a larger average micropore size. The greater reduction of the micropore volume in H_2O/CO_2 gasified biochar indicates that the rate of micropore enlargement become higher than that of micropore creation at the late stage of the process. This could be attributed to the rapid removal of large amount of carbon atoms by both H_2O and CO_2 molecules, causing the rapid destruction/collapse of micropore walls. The results suggest that there could be a synergy effect between H_2O and CO_2 in attacking various active carbon sites. For example, the micropore wall left by H_2O is preferentially consumed by CO_2, consequently, a rapid enlargement of micropores would occur. Unlike gasification in H_2O and H_2O/CO_2, the rate of micropore enlargement is probably slower than that of new micropore generation for CO_2 gasification. Consequently, within the experimental time in this study, there is a steady increase in the micropore volume of the CO_2 gasified biochar.

The pore sizes and volume fractions derived from the Unified fit (as reflected in *Table 3. 1*) are comparable to the pore size distribution obtained using the IPG/TNNLS fitting method in Irena [36], as shown in *Figure* 3. *4*. Similarly, most of the micropores are around 10 Å and no obvious changes in the pore volume distribution is observed. If we compare the micropore volume for biochar gasified in different atmospheres for the same time, the biochar gasified in CO_2 has the highest micropore volume, followed by the biochar gasified in H_2O, whilst the micropore volume in biochar gasified in H_2O/CO_2 is the lowest. This agrees with literature [5,6,13,15,16], where gasification with H_2O leads to biochar with a lower micropore volume than CO_2. It seems that the enlargement of micropores could be a primary phenomenon in the presence of H_2O. Accordingly, the resulting in biochars exhibit a low micropore volume at the late stage of the process after gasification in H_2O and/or H_2O/CO_2.

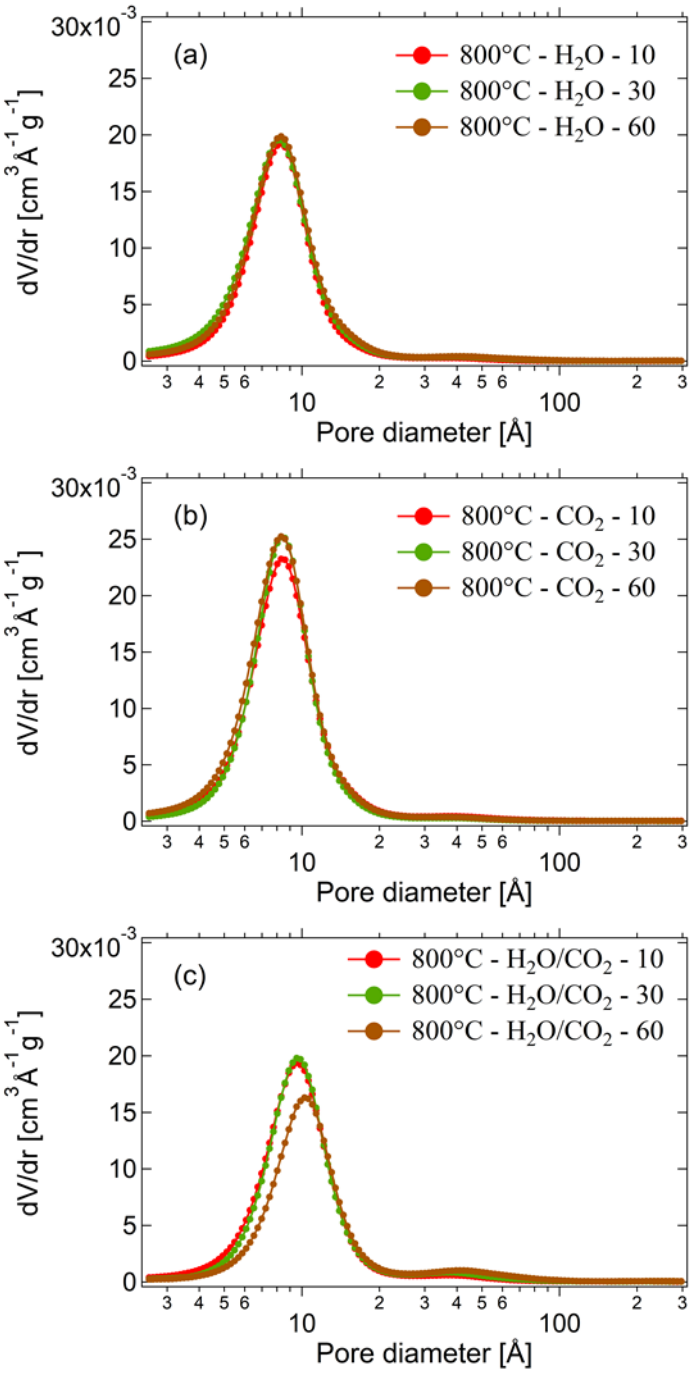

Figure 3. 4. Pore size and volume distribution of biochar over gasification time (10, 30 and 60 min) in (a) H_2O, (b) CO_2 and (c) H_2O/CO_2. The results were obtained from the IPG/TNNLS fitting method to SAXS data.

The specific surface area (SSA, as shown in *Table 3. 1*) can also be extracted from the SAXS data where it can be seen that both of the H_2O and H_2O/CO_2 gasified biochars showed significant growth after gasification for 60 min (60% and 97% growth respectively). The biochar derived from gasification in H_2O/CO_2 has the highest SSA (250 m^2/g). However, only

a small increase was observed for the biochar gasified in CO_2 (14% growth). The reason for the growth of SSA could be due to the rough surface of mesopores [39], which will be discussed later.

One of the most important parameters to help understand the evolution of pore structure in biochar is the fractal information of the pore network, which is a measure of its morphology. Fractal information is an intrinsic characteristic of an object, regardless of the scale at which it is viewed [24,38]. This fractal property can be used to describe the surface roughness of a pore (surface fractal) or the aggregation of a network of smaller pores (pore fractal) [26]. The modelled fractal dimensions of mesopores from SAXS data are presented in *Table 3. 1*. As mentioned above, the power law slope (*P*) lies between 1 and 3 for pore fractals and between 3 and 4 in the case of surface fractals. In this scenario, a pore fractal where P approaches 2 describes an almost sheet-like network (do not display branching), and conversely when P approaches 3, the fractal dimension describes an extremely disordered pore network in three dimensions that is akin to a sponge-like morphology. The power law slope *P* in the surface fractal regime approaches 3 for an extremely rough surface, bordering on becoming a sponge-like aggregate of pores/surface. Whereas, when a power law slope *P* becomes 4 it is a representation of a perfectly smooth surface.

For the biochar gasified in CO_2, the *P* values suggest a pore fractal of dimension D_p = 2.4 where the dimension increases (to 2.7) as gasification proceeds. The results indicate that micropores are distributed across biochar in a way that forms a network of micropore clusters of a particular size that become more sponge-like and more branched over time. At the end of gasification, the derived biochar presents a porous network of clusters of branched micropore aggregates [26,42]. As mentioned before, the way in which the pore network of biochar evolves reflects the way in which the carbon atoms are removed. The evolution of the fractal features in biochar during CO_2 gasification suggests that the removal of carbon atoms occurs in clusters at particular locations. CO_2 molecules react with carbon atoms at particular active sites, inducing the local etching of pore walls to form mesoporous channels of uniform size. This process then branches in a new direction in such a way that the remaining carbon solid is riddled with micropore clusters, leaving behind a porous network with a fractal dimension just below 3.

In contrast, the pore evolution during gasification in H_2O and H_2O/CO_2 occurs differently to that in CO_2 alone. The mesopore network does exhibit a branched and disordered pore network (pore fractal) at the early stages of gasification but the pore network transitions into a surface fractal at the late stage, representing a larger mesopore with a rough surface where the cluster of micropore channels used to reside. Essentially, this is the physical representation of the transition from a pore fractal to a surface fractal. This process is akin to removing solid material from a sponge-like object until there only remains a larger pore without many interconnected solids across that pore, but only a remnant of solid roughness on the surface of the larger pore. Thus, considerable numbers of carbon atoms are removed at the late stages of gasification, giving rise to the collapse and damage of micropore walls. As a result, a rough surface in the mesopores is detected instead of the previous branched micropore network. The different pore evolution, reflected by the fractal dimension, between H_2O and CO_2 gasified biochar could result from the different reactivity of H_2O and CO_2 with carbon [5,10,43]. At 800°C, lower energy is needed to dissociate a H_2O molecule than for a CO_2 molecule (the apparent activation energies are 275 and 211 kJ/mol for CO_2 and H_2O, respectively) [5,43,44]. The high reactivity of H_2O makes it less selective in reacting with biochar in comparison to CO_2. Therefore, H_2O molecules react with carbon atoms located almost anywhere. Carbon atoms can be removed layer after layer to essentially carve out a mesopore from a cluster of smaller micropores. With the continuous elimination of carbon atoms in this way, the pore network transits from a pore fractal to surface fractal. This could also be a principal process during the gasification in H_2O/CO_2, giving rise to the similar changes in fractal dimensions of biochar to that of H_2O gasified biochar. The high selectivity of CO_2 results in preferred carbon attack, and thus the development of a more branched micropore network.

Our *in situ* SAXS data has shown clear differences in pore development especially the fractal properties between biochar gasified in H_2O and CO_2. The fractal feature of the porous network in biochar shows the way in which pores (empty phase) distribute in the two-phase structure. Thus, from another perspective, it also reflects the way of the arrangement and organisation of the carbon matrix (solid phase). Therefore, the different fractal features of biochar gasified in H_2O and CO_2 has further confirmed that the reaction pathway for biochar gasification in H_2O is different from that in CO_2 [45,46]. Pore enlargement is a prominent phenomenon during gasification in H_2O and H_2O/CO_2, while CO_2 tends to produce biochar

with a high micropore volume in a branched network. A significant increase in SSA of biochar was observed during gasification in H_2O and H_2O/CO_2, which is predominantly associated with the development of rough mesopore surfaces. The simultaneous use of H_2O and CO_2 produced a higher SSA in biochar than the case in which only H_2O or CO_2 was used, due to a synergistic development of rough surfaced mesopores and additional branched micropore clusters. The result is generally consistent with the findings obtained using gas adsorption techniques and SAXS by others [5,6,11,13,15,16,47].

3.3.2 The impact of temperature on pore development of biochar during gasification in H_2O and/or CO_2.

3.3.2.1 Pore development during gasification at 700°C in H_2O and CO_2.

Figure 3. 5 shows the SAXS patterns of biochar during (a) H_2O gasification at 700°C and (b) CO_2 gasification at 700°C for 60 min. As expected, unlike gasification at 800°C, only minor changes in the intensities were shown when biochar was gasified at 700°C. This is particularly true for the case of gasification in CO_2 (*Figure 3. 5*b), during which the SAXS patterns barely changed. The data imply that the pore structure of biochar changed slightly or stayed almost unchanged. This is because, at 700°C, the reactions were modest and unable to eliminate sufficient carbon atoms to cause porosity development.

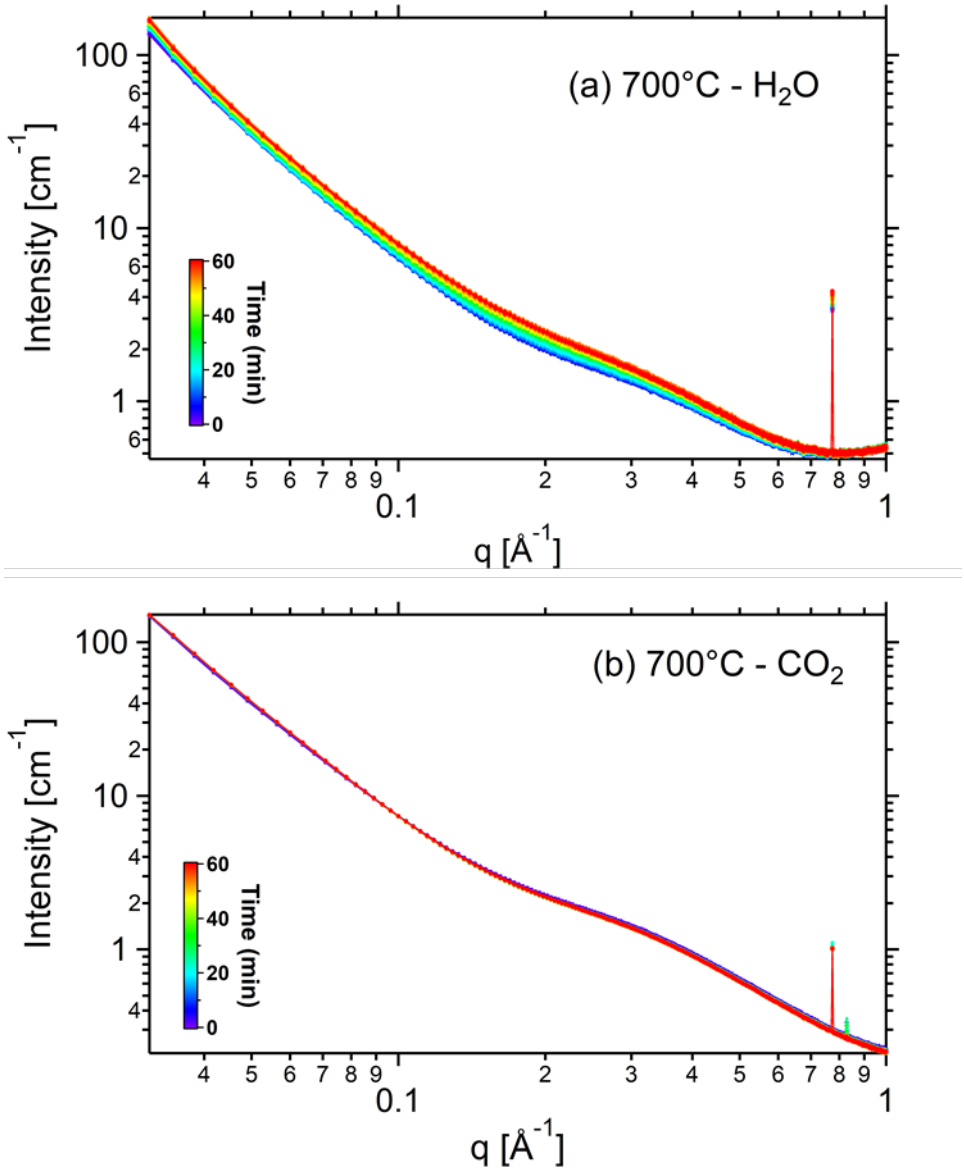

Figure 3. 5. SAXS patterns of biochar during gasification at 700°C (a) in H_2O for 60 min, (b) in CO_2 for 60 min. Please be noted that the peaks at high q from the detector and can be neglected.

Despite the small changes in the scattering intensities, the SAXS patterns of biochar changed more significantly during gasification in H_2O than that during CO_2 gasification. The SAXS intensities showed a slightly increasing trend in intensities for the whole *q* range over the 60 min of gasification in H_2O, suggesting the development of both micropores and mesopores or the increase of SSA in biochar. The barely visible changes in SAXS patterns of CO_2 gasified biochar is most likely ascribed to the lower reactivity of CO_2 compared to H_2O [5,44,48]. At 700°C, the reactivity of carbon sites with CO_2 is not high enough for intense

reactions to take place. For this reason, the pore structure of biochar is nearly constant throughout the process [22].

3.3.2.2 Pore development during gasification at 900°C in H_2O.

As gasification is typically carried out between 800 and 900°C, it is of more practical significance to investigate the pore development of biochar at temperatures above 800°C. Thus we also performed the gasification in H_2O at 900°C. It is worth mentioning that the measurement was ceased after 35 min of gasification when the biochar was completely consumed. The quick conversion of biochar is due to the enhanced thermal cracking and gasification reactions at 900°C. The SAXS patterns of biochar are displayed in *Figure 3. 6*. Before the completion of reactions, the evolution of scattering intensity (*Figure 3. 6*b) is similar to that obtained for biochar during gasification in H_2O at 800°C (*Figure 3. 2*a). When the reaction went to completion, the total intensity dropped quickly and eventually was shown as the red line in *Figure 3. 6*a. It can be seen that the signals at high q disappeared eventually, demonstrating a complete loss of microporosity. The scattering intensity at low q shows a q^{-4} dependency ($P = 4$), as indicated by the black line in *Figure 3. 6*a, which means the scattering was generated from residual bulk surface scattering.

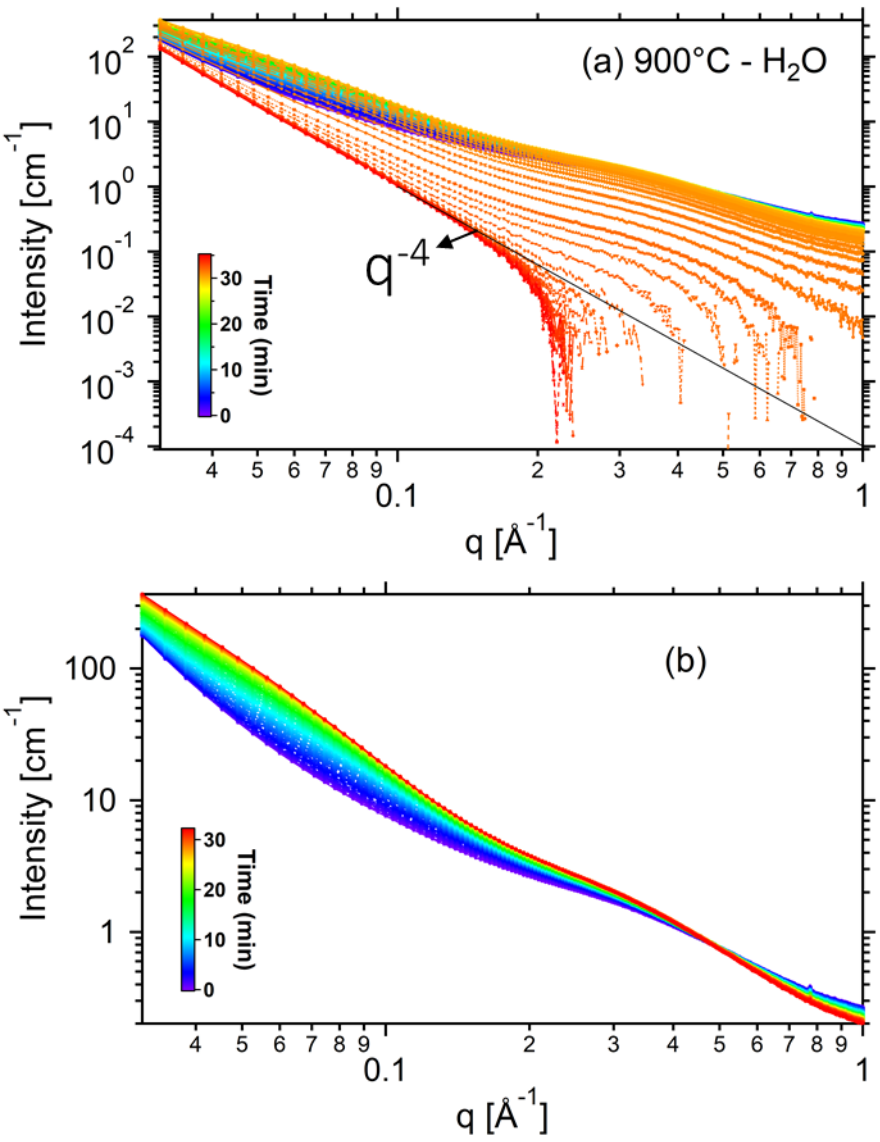

Figure 3. 6. (a) SAXS pattern of biochar during gasification in H_2O at 900°C until the complete conversion of biochar; (b) SAXS pattern of biochar during gasification at 900°C before the completion of reaction.

To have a better understanding of the temperature influence on pore development, the pore size distributions for biochar were compared further in *Figure 3. 7*. After 30 min of gasification, the increase in temperature from 700 to 800°C leads to a wider pore size distribution with the growth of both micropore and mesopore volume. The rise of temperature can not only promote the creation but also the enlargement of micropores. As stated before, the pore development in biochar is the result of the selective removal of carbon structures, which is determined by the reactivity between carbon sites and gasifying agents.

There are different carbon sites with various structural features and energy levels in biochar. Therefore, different activation energies are required for those carbon sites to react with gasifying agents. At 700°C, most of the carbon sites are not reactive enough to react with gasifying agents and therefore to be removed. As a result, no obvious creation of pores will be observed. When the temperature increases to 800°C, more carbon sites become reactive enough to react with gasifying agents. Accordingly, an obvious development of micro- and mesopores will occur, as we observed here.

A further rise in temperature from 800 to 900°C gives rise to a decrease in the micropore volume as well as a shift of the distribution of pores to larger sizes. This is because a large amount of micropores are already converted to mesopores and macropores after gasification at 900°C for such a long time. During gasification at 800°C, those carbon sites with lower activation energies would be gasified/consumed more easily than those with higher activation energies. At 900°C, the reaction rate of carbon sites with higher activation energies increases more rapidly than that of carbon sites with lower activation energies. When different carbon sites have closer gasification rates, carbon removal become less selective and a less significant micropore creation would occur at 900°C. Pore development would be dominated by the development of large pores due to the enhanced gasification rate and thermal cracking. Therefore, at a similar biochar conversion level (after gasification at 900°C for 10 min and at 800 for 30 min, see ref [49]), the biochar gasified at 900°C has a lower micropore volume (0.12 cm^3/g) than the biochar gasified at 800°C (0.20 cm^3/g).

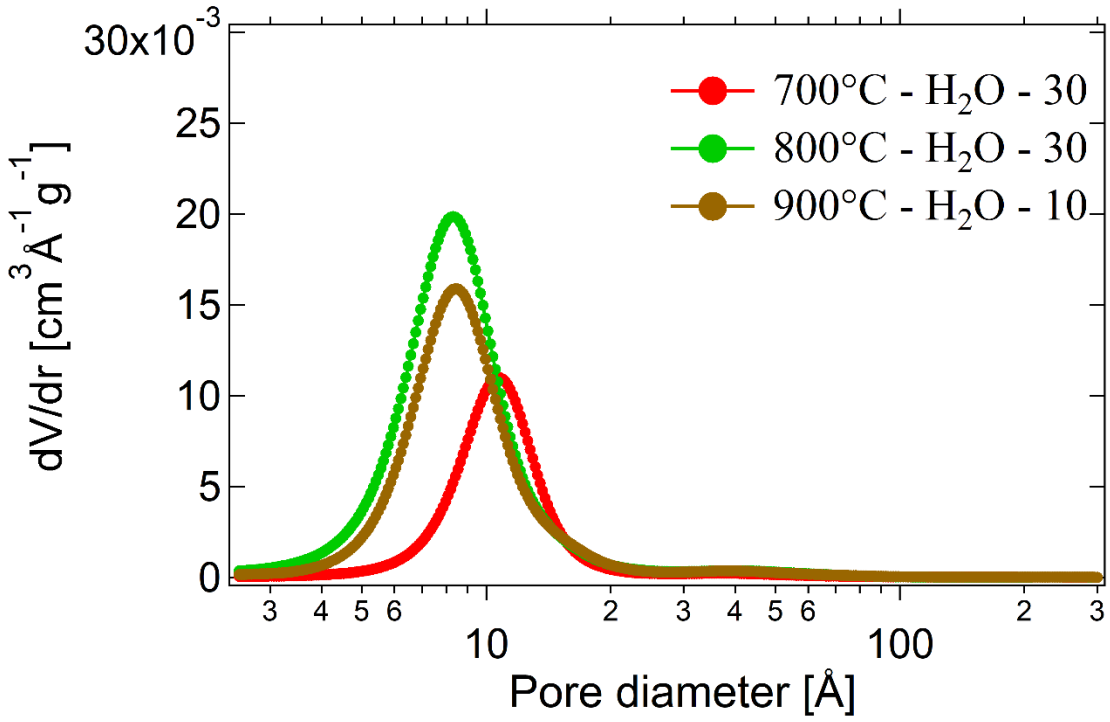

Figure 3. 7. Pore size and volume distribution for biochars after 30 min gasification in H_2O at 700 and 800°C, 10 min at 900°C.

3.4 Conclusion

The evolution in pore structure of biochar during gasification was investigated *in situ* using synchrotron SAXS. Differences in the pore development were observed for biochar gasified in different atmospheres (H_2O, CO_2, and H_2O/CO_2) and at different temperatures (700, 800 and 900°C). H_2O started to create micro- and mesopores at 700°C while the pore structure of biochar stayed nearly unchanged during CO_2 gasification at 700°C. At 800°C, the simultaneous use of H_2O and CO_2 led to a higher SSA in biochar than the case in which only H_2O or CO_2 was used. The CO_2 gasified biochar exhibited a high micropore volume while the enlargement of micropores was a pronounced phenomenon during H_2O and H_2O/CO_2 gasification. Moreover, the mesoporous network of biochar gasified in CO_2 presented pore fractal features throughout the whole gasification process. A transition from pore fractal to surface fractal was observed for the biochar gasified in H_2O and H_2O/CO_2. The differences in the evolution of pore structure between biochar gasified in H_2O and CO_2 could be attributed to the different

reactivity of H_2O and CO_2. CO_2 is less reactive and more selective towards reacting with biochar. It was found that the increase in temperature enhanced reaction rates and makes carbon removal less selective, leading to the enhanced rate of pore creation and enlargement.

3.5 Reference

[1] Li C-Z. Special issue—gasification: a route to clean energy. Process Saf Environ Prot 2006;84:407–8.

[2] Li C-Z. Importance of volatile-char interactions during the pyrolysis and gasification of low-rank fuels - A review. Fuel 2013;112:609–23.

[3] Wang S, Wu L, Hu X, Zhang L, O'Donnell KM, Buckley CE, Li C-Z. An X-ray photoelectron spectroscopic perspective for the evolution of O-containing structures in char during gasification. Fuel Process Technol 2018;172:209–15.

[4] Wu H, Yip K, Tian F, Xie Z, Li C-Z. Evolution of char structure during the steam gasification of biochars produced from the pyrolysis of various mallee biomass components. Ind Eng Chem Res 2009;48:10431–8.

[5] Rodríguez-Reinoso F, Molina-Sabio M, González MT. The use of steam and CO_2 as activating agents in the preparation of activated carbons. Carbon N Y 1995;33:15–23.

[6] Pastor-Villegas J, Durán-Valle CJ. Pore structure of activated carbons prepared by carbon dioxide and steam activation at different temperatures from extracted rockrose. Carbon N Y 2002;40:397–402.

[7] Liu Y, Paskevicius M, Wang H, Parkinson G, Veder JP, Hu X, Li C-Z. Role of O-containing functional groups in biochar during the catalytic steam reforming of tar using the biochar as a catalyst. Fuel 2019;253:441–8.

[8] Liu Y, Paskevicius M, Wang H, Fushimi C, Parkinson G, Li C-Z. Difference in tar reforming activities between biochar catalysts activated in H_2O and CO_2. Fuel 2020;271:117636.

[9] Tomków K, Siemieniewska T, Czechowski F, Jankowska A. Formation of porous structures in activated brown-coal chars using O_2, CO_2 and H_2O as activating agents. Fuel 1977;56:121–4.

[10] González JF, Encinar JM, González-García CM, Sabio E, Ramiro A, Canito JL, Gañán J. Preparation of activated carbons from used tyres by gasification with steam and carbon dioxide. Appl Surf Sci 2006;252:5999–6004.

[11] Coetzee GH, Sakurovs R, Neomagus HWJP, Morpeth L, Everson RC, Mathews JP, Bunt JR. Pore development during gasification of South African inertinite-rich chars evaluated using small angle X-ray scattering. Carbon N Y 2015;95:250–60.

[12] Sircar I, Sane A, Wang W, Gore JP. Experimental and modeling study of pinewood char gasification with CO_2. Fuel 2014;119:38–46.

[13] Molina-Sabio M, González MT, Rodriguez-Reinoso F, Sepúlveda-Escribano A. Effect of steam and carbon dioxide activation in the micropore size distribution of activated carbon. Carbon N Y 1996;34:505–9.

[14] Rodríguez-Reinoso F. Controlled gasification of carbon and pore structure development. In: Lahaye J. EP, editor. Fundam. Issues Control Carbon Gasif. React., Springer, Dordrecht; 1991, p. 533–71.

[15] Gonzalez J, Gonza JF, Roma S, Gonza CM, Ortiz AL, Roma R. Porosity Development in Activated Carbons Prepared from Walnut Shells by Carbon Dioxide or Steam Activation Porosity Development in Activated Carbons Prepared from Walnut Shells by Carbon Dioxide or Steam Activation 2009:7474–81.

[16] Bai Y, Lv P, Yang X, Gao M, Zhu S, Yan L, Li F. Gasification of coal char in H_2O/CO_2 atmospheres: Evolution of surface morphology and pore structure. Fuel 2018;218:236–46.

[17] Kalliat M, Kwak CY, Schmidt PW, Cutter BE, McGinnes EA. Small angle X-ray scattering measurement of porosity in wood following pyrolysis. Wood Sci Technol 1983;17:241–57.

[18] Foster M, Jensen KF. Small angle X-ray scattering investigations of pore structure changes during coal gasif ication 1990;69:88–96.

[19] Reich MH, Russo SP, Snook IK, Wagenfeld HK. The application of SAXS to determine the fractal properties of porous carbon-based materials. J Colloid Interface Sci 1990;135:353–62.

[20] Foster MD, Jensen KF. SAXS investigation of model carbon pore structure and its change with gasification. Carbon N Y 1991;29:271–82.

[21] Nakagawa T, Komaki I, Sakawa M, Nishikawa K. Small angle X-ray scattering study on change of fractal property of Witbank coal with heat treatment. Fuel 2000;79:1341–6.

[22] Smith AJ, MacDonald MJ, Ellis LD, Obrovac MN, Dahn JR. A small angle X-ray scattering and electrochemical study of the decomposition of wood during pyrolysis. Carbon N Y 2012;50:3717–23.

[23] Okolo GN, Everson RC, Neomagus HWJP, Roberts MJ, Sakurovs R. Comparing the porosity and surface areas of coal as measured by gas adsorption, mercury intrusion and SAXS techniques. Fuel 2015;141:293–304.

[24] Beaucage G. Determination of branch fraction and minimum dimension of mass-fractal aggregates. Phys Rev E - Stat Physics, Plasmas, Fluids, Relat Interdiscip Top 2004;70:10.

[25] Pfeifer P. Fractal dimension as working tool for surface-roughness problems. Appl Surf Sci 1984;18:146–64.

[26] Pfeifer P, Ehrburger-Dolle F, Rieker TP, González MT, Hoffman WP, Molina-Sabio M, Rodríguez-Reinoso F, Schmidt PW, Voss DJ. Nearly space-filling fractal networks of carbon nanopores. Phys Rev Lett 2002;88:115502.

[27] Bale HD, Schmidt PW. Small-Angle X-Ray-Scattering Investigation of Submicroscopic Porosity with Fractal Properties. Phys Rev Lett 1984;53:596–9.

[28] Kirby NM, Mudie ST, Hawley AM, Cookson DJ, Mertens HDT, Cowieson N, Samardzic-Boban V. A low-background-intensity focusing small-angle X-ray scattering undulator beamline. J Appl Crystallogr 2013;46:1670–80.

[29] Glatter O, Kratky O. Small angle x-ray scattering. 1982.

[30] Dreiss CA, Jack KS, Parker AP. On the absolute calibration of bench-top small-angle X-ray scattering instruments: A comparison of different standard methods. J Appl Crystallogr 2006;39:32–8.

[31] Advanced biomass gasification technology, Australian Renewable Energy Agency.

[32] Grinding pyrolysis, Renergi Pty Ltd. http://www.renergi.net/grinding_pyrolysis.

(accessed December 20, 2020).

[33] Allen AJ, Zhang F, Joseph Kline R, Guthrie WF, Ilavsky J. NIST Standard Reference Material 3600: Absolute Intensity Calibration Standard for Small-Angle X-ray Scattering. J Appl Crystallogr 2017;50:462–74.

[34] SAXS Software - scatterBrain.

[35] Spalla O, Lyonnard S, Testard F. Analysis of the small-angle intensity scattered by a porous and granular medium. J Appl Crystallogr 2003;36:338–47.

[36] Ilavsky J, Jemian PR. Irena : tool suite for modeling and analysis of small-angle scattering. J Appl Crystallogr 2009;42:347–53.

[37] Beaucage G. Approximations leading to a unified exponential power-law approach to small-angle scattering. J Appl Crystallogr 1995;28:717–28.

[38] Beaucage G, IUCr. Small-Angle Scattering from Polymeric Mass Fractals of Arbitrary Mass-Fractal Dimension. J Appl Crystallogr 1996;29:134–46.

[39] Hurd AJ, Schaefer DW, Smith DM, Ross SB, Le Méhauté A, Spooner S. Surface areas of fractally rough particles studied by scattering. Phys Rev B 1989;39:9742–5.

[40] Paskevicius M. A nanostructural investigation of mechanochemically synthesised hydrogen storage materials, PhD thesis, Curtin University of Technology, Australia. 2009.

[41] Beaucage G, Kammler HK, Pratsinis SE. Particle size distributions from small-angle scattering using global scattering functions. J Appl Crystallogr 2004;37:523–35.

[42] Avnir D, Farin D, Pfeifer P. Surface geometric irregularity of particulate materials: The fractal approach. J Colloid Interface Sci 1985;103:112–23.

[43] González JF, Román S, González-García CM, Nabais JMV, Ortiz AL. Porosity development in activated carbons prepared from walnut shells by carbon dioxide or steam activation. Ind Eng Chem Res 2009;48:9354.

[44] Román S, González JF, González-García CM, Zamora F. Control of pore development during CO_2 and steam activation of olive stones. Fuel Process Technol 2008;89:715–20.

[45] Tay HL, Kajitani S, Zhang S, Li C-Z. Effects of gasifying agent on the evolution of char

structure during the gasification of Victorian brown coal. Fuel 2013;103:22–8.

[46] Wang S, Wu L, Hu X, Zhang L, Li T, Li C-Z. Effects of the particle size and gasification atmosphere on the changes in the char structure during the gasification of mallee biomass. Energy and Fuels 2018;32:7678–84.

[47] Arenas E, Chejne F. The effect of the activating agent and temperature on the porosity development of physically activated coal chars. Carbon N Y 2004;42:2451–5.

[48] Pallarés J, González-Cencerrado A, Arauzo I. Production and characterization of activated carbon from barley straw by physical activation with carbon dioxide and steam. Biomass and Bioenergy 2018;115:64–73.

[49] Wang S. Evolution of Char Structure and Reactivity during Gasification (thesis). Curtin University, 2016.

Chapter 4

A SAXS study of the pore structure evolution in biochar during gasification in H_2O, CO_2 and H_2O/CO_2

Y. Liu, M. Paskevicius, M.V. Sofianos, G. Parkinson, S. Wang, C.-Z. Li, A SAXS study of the pore structure evolution in biochar during gasification in H_2O, CO_2 and H_2O/CO_2, Fuel. 292 (2021) 120384. https://doi.org/10.1016/j.fuel.2021.120384.

Abstract

Gasification of biomass allows for its efficient utilisation as a renewable fuel through syngas production. This work presents the different effects of gasifying agents (H_2O, CO_2 and H_2O/CO_2) on the evolution of pore structure in biochar during gasification. The effects of temperature (700, 800 and 900°C) and biomass particle sizes (up to 5.6 mm) were also studied. The pore structure of biochar was characterized using synchrotron small angle X-ray scattering (SAXS). The pore development in biochar during gasification in H_2O/CO_2 is close to that in H_2O. Carbon removal is more selective in CO_2 and the derived biochar displays pore fractal features. Whereas the H_2O-derived biochar exhibits a surface fractal network. The development of pore structure produced by various gasifying agents is paralleled by the evolution of the aromatic structures characterized by Raman spectroscopy. The different pore structural features result from the different reactivity of carbon sites with H_2O and CO_2, which could be attributed to the different amounts of O-containing groups in biochar as well as the different reactivity between H_2O and CO_2. Increasing temperature reduces differences in pore structure between the biochars gasified in H_2O and CO_2. Biomass particle size has little impact on the pore structure of biochar.

4.1 Introduction

The ever-increasing need for the reduction of greenhouse gas emissions has made clean and renewable energy resources attractive. Biomass, as a potential carbon-neutral and renewable energy source, has gained particular attention [1,2]. Gasification is a promising technology to achieve highly efficient utilization of biomass by thermochemically converting biomass to syngas, which can be further used for electricity generation and the production of liquid fuels and chemicals [2]. During gasification, carbon atoms are continuously removed by reacting with gasifying agents, leading to the rearrangement and reorganisation of the residual carbon matrix [3]. As the porosity in biochar originates from the disordered organisation of the carbon matrix, therefore, the porous structure of biochar changes drastically in the meantime [4,5]. The study of the changes in the pore structure of biochar is therefore essential for understanding the reaction pathways of biochar during gasification in various gasifying agents.

Moreover, the porous nature of activated biochar is a key property influencing its utilization as an absorbent and possible energy storage material [6]. Therefore, the study of the pore structure of biochar is also of great significance for achieving efficient utilization of biochar as well as for optimizing the process of thermal activation to produce activated carbon.

Intensive studies [7,8,17,18,9–16] have been undertaken on the porosity development of biochar during gasification. It has been widely found that H_2O and CO_2 produce biochars with different pore size distributions. Despite the considerable efforts made by many researchers, the explanation for the different effects of H_2O and CO_2 on the pore development in biochar is not unanimous. Some studies attribute it to the different diffusion coefficients of H_2O and CO_2 arising from their different molecular dimensions [13,19,20]. Others believe that it is the differences in extents of product (H_2 and CO) inhibition in the C—CO_2 and C—H_2O reactions that causes the different porosity development between biochars gasified in H_2O and CO_2 [21,22].

In any case, we believe the porosity development in biochar is a function of the gasification mechanism. During biochar gasification, with continuous carbon removal and re-arrangement of the carbon structure, the pore structure described by the pore shape and size distribution evolves simultaneously [5]. To have a complete picture of the process of biochar gasification or activation, one must have an adequate understanding of the evolution of the pore structure that is a consequence of the alteration of the carbon skeleton, driven by gasification/activation under different conditions. However, as far as we know, hardly anyone has connected the evolution of pore structure in biochar to changes in its chemical structure.

Therefore, it is compelling to investigate the evolution of both the pore structure and chemical structure of biochar during gasification. Small angle X-ray scattering (SAXS) has been demonstrated to be suitable for characterizing the pore structure of disordered carbonaceous materials as it has advantages over other traditional techniques such as gas (i.e. N_2) adsorption/desorption and transmission electron microscopy (TEM) [23]. For example, gas adsorption can only detect the pores that gases can access, and transmission electron microscope (TEM) can only give the information of pores in a limited sample volume [8,24–26]. SAXS can detect a wide range of pore sizes including closed pores in bulk samples [11,27,28]. More importantly, SAXS has an advantage of “seeing” into the structure of the carbon matrix in biochar by giving information on the fractal features of the pore network

over different length scales [29–31]. A fractal model is a mathematical method of describing disordered and irregular objects [32,33]. The fractal dimension of pores is particularly useful in describing the network of pore aggregation (pore fractal) as well as the irregularity and roughness of pore boundaries (surface fractal) [34]. Thus, changes in the fractal dimension of pores can describe the evolution of the carbon skeleton in biochar during gasification. On the other hand, FT-Raman spectroscopy has long been demonstrated to be suitable for characterizing the chemical structure of biochar [3,35,36].

To this end, in this work, biochar was gasified in H_2O, CO_2 and H_2O/CO_2 respectively to various conversion levels. The evolution of the pore structure and chemical structure was characterized by SAXS and FT-Raman spectroscopy respectively. The aim of this study is to investigate the different mechanisms through which the three gasifying agents develop micro- and mesopores in biochar by combining the fractal properties of the porous structure of biochar with information regarding the transformation of chemical structures in biochar. The effects of temperature and biomass particle size on the pore structure of biochar were also studied.

4.2 Experimental

4.2.1 Biochar preparation

Three series of experiments were carried out to prepare biochar samples. The first series (biochar A) was the gasification of biochar (106–250 μm) at 800 ˚C in 15 vol. % H_2O balanced with Ar (named H_2O), pure CO_2 (named CO_2) and/or 15 vol. % H_2O mixed with CO_2 (named H_2O/CO_2) for varying periods (10–50 min). The starting biochar was obtained from the pyrolysis and partial gasification (5–10 min) of Mallee biomass at 750 – 850 °C in Renergi's gasification demonstration plant [33,34] using a three-frit two-stage fluidized-bed/fixed bed quartz reactor [31,32]. Briefly, 1 g of biochar was preloaded in the middle frit of the reactor before being heated under argon. After the reactor had stabilised at 800 °C, argon was switched to H_2O, CO_2 or H_2O/CO_2 at a total flow rate of 2.0 L min^{-1} to continue the gasification of biochar for different times. Biochar samples were collected after the reactor had cooled down under argon flow.

The second series (biochar B) of experiments was the gasification of Mallee wood (4.75–5.6mm) at different temperatures (700, 800 or 900 ˚C) in 15% H_2O/Ar and/or pure CO_2 for the same time (4 min). The experimental procedure was described in our previous study [35]. Briefly, a fluidised-bed quartz reactor was placed in a furnace and heated up with argon flowing through the reactor. After the target temperatures were reached, approximately 2 g of Mallee wood was fed into the reactor to commence the pyrolysis of the sample. The reactor was held for 20 mins in argon after the completion of feeding. Afterwards, argon was switched to 15% H_2O/Ar and/or pure CO_2 to proceed the gasification of biochar for 4 mins. Reactor was then lifted out of the furnace and cooled down in argon before biochar was collected.

The third series (biochar C) of experiments was the gasification of biomass with different particle sizes at 800°C in 15% H_2O/Ar and/or pure CO_2. The particle sizes of Mallee wood samples are: 0.18−1.0, 1.0−2.0, 2.0−3.35, 3.35−4.0, 4.0−4.75, and 4.75−5.6 mm. As was described in detail previously [36], a fluidised-bed quartz reactor was firstly heated up to 800°C with 15% H_2O/Ar or pure CO_2 flowing through the reactor. Afterwards, 2 g of Mallee wood was fed into the reactor within 4 min. When the feeding of biomass was finished, the reactor was immediately lifted out of the furnace and cooled down in argon. The obtained biochar samples were then collected to study the influence of biomass particle size on the pore structure of biochar.

4.2.2 Characterisation of the pore structure of biochar

4.2.2.1 SAXS measurement

The pore structure of biochar was characterised using the SAXS beamline equipped with a Pilatus 1-M detector at the Australian Synchrotron in Melbourne [37]. The FWHM beam size was 240 μm horizontally and 24 μm vertically. Biochar samples were mounted in square holes (4 x 4 mm) in a 2-mm-thick stainless steel plate with Kapton tape covering both sides. All samples were measured at two camera lengths (3343 mm and 959 mm) to achieve a wide q-range (q is the scattering vector $q = (4\pi/\lambda)\sin(\theta/2)$, λ (1.03 Å) and θ are the wavelength and scattering angle) from 0.005 to 1.5 $Å^{-1}$, respectively, which are appropriate to probe a pore diameter ranging approximately from 0.4 to 125 nm. For each sample, 10 scans were

acquired across the sample to provide a representative analysis. The data collection time for each scan is 1 second. Silver behenate was used to calibrate the *q*-scale of the instrument, and glassy carbon (1 mm thick) was used for absolute intensity calibration [38]. A scattering background from Kapton tape was measured and subtracted from data sets. The X-ray transmission (T_S) was acquired by recording the incident flux (I_0) and transmitted flux (I_{BS}) using an upstream detector and a detector inside the beamstop respectively.

4.2.2.2 SAXS data processing and analysis

The measured intensities were background subtracted and calibrated using glassy carbon before being normalised for sample thickness to convert to absolute intensities [38–40]. The effective solid thickness (*d*) of the sample was calculated using [39]:

$$d = -\ \ln(T_S)/\mu \qquad (4.1)$$

where, μ is the linear adsorption coefficient of the sample, assumed to be purely amorphous carbon with a density of 2.0 g cm^{-3}. Afterwards, the data collected at two detector positions were merged together and then fitted with the unified model [41] using Irena [42] within Igor Pro (Wavemetrics). The unified model [41] was applied because it can describe the structural features of complex systems containing several structural levels (displaying multiple size-scale structures). In general, on a log-log plot of *I*(*q*), the SAXS spectrum for each level contains a Guinier region (a 'knee-like' feature) and a linear power law region at higher-*q* [41]. The Guinier region represents the average size of pores and their radius can be calculated by $r = \sqrt{5/3}\ R_g$ (R_g is the radius of gyration of the scattering objects) if we assume the pores are nearly spherical. The slope (*P*) of the power law region gives information on the characteristics of pore morphology and texture by providing fractal dimensions of the pores [25,27,41]. For a smooth and sharp interface between the pore wall and void, the power-law follows Porod's law and *P* = 4. Rough surfaced pores can be represented by surface fractals, where the value of *P* lies between 3 and 4 and the fractal dimension $D_s = -P + 6$. The increase of D_s represents an increase in surface roughness. Aggregate-type structures can be explained by pore fractal where *P* < 3 and the fractal dimension $D_p = P$.

In the case of biochar, three structural levels were used to model the scattering curve. As shown in *Figure* 4. 1, the three levels represent the scattering from the microporous (1 – high *q*), mesoporous (2 – middle *q*) and macroporous (3 – low *q*) size regimes, respectively.

Because the scattering intensity in the high q power law region is too close to the scattering from the background, it was assumed that the micropore surface is smooth and the slope of the high q (level 1) power law was fixed ($P_1 = 4$). This is also necessary to obtain a stable and repeatable fit to the data. Due to the limited q range, a Guinier regime does not present from the macroporous size regime, which would exist at even lower q (< 0.005 Å^{-1}). As a result, the third structural level at low q only includes a power law region (P_3). As such, refined parameters, including the average size of micro- and mesopores (given by R_{g1} and R_{g2} respectively) as well as the fractal dimensions (given by P_2 and P_3), were extracted from SAXS data.

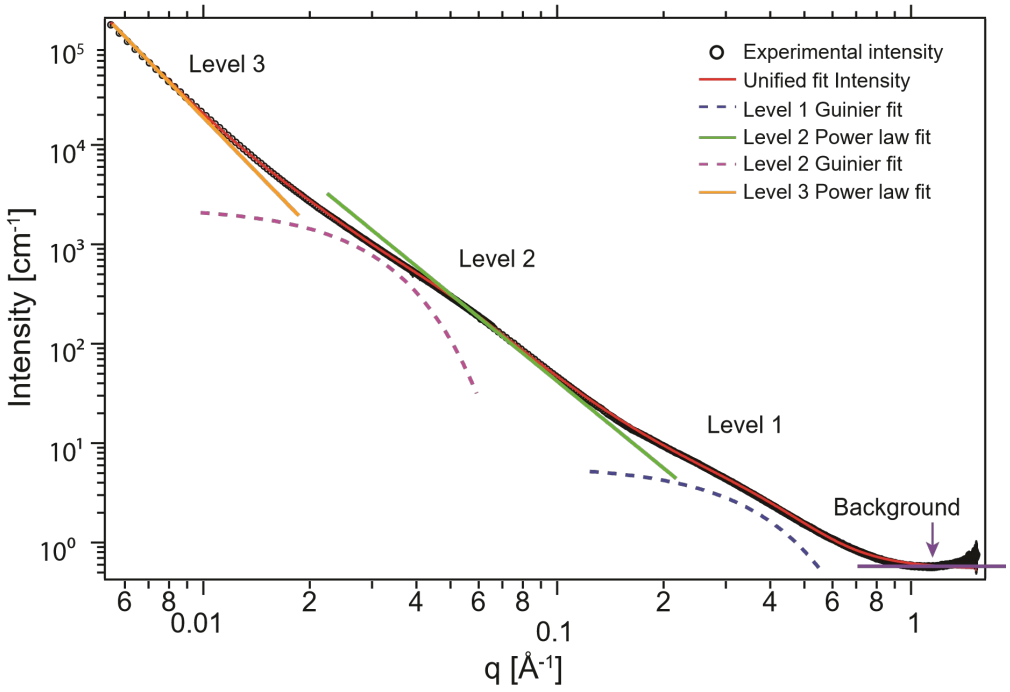

Figure 4. 1. A typical SAXS pattern of log ($I_{(q)}$) versus log (q) representing the scattering intensity (black circles) and the three-level unified fit (red line) to the data.

The specific surface area for a surface fractal [43] using a particular measurement scale, r, is given by the following (r = 4 Å, the size of a nitrogen molecule in this study) :

$$S(r) = Sr^{2-D_s} \quad (4.2)$$

Where S is given by:

$$S = 2\pi\varphi(1-\varphi)B/Q\rho_{bulk}F(D_s) \quad (4.3)$$

Where $F(D_s)$, φ and Q are given by the following:

$$F(D_s) = \Gamma(5 - D_s)\sin[\pi(3 - D_s)/2]/(3 - D_s) \quad (4.4)$$

$$\varphi = \rho_{bulk}/\rho_{base\ material} \quad (4.5)$$

$$Q = \int_0^\infty I(q)q^2dq = 2\pi^2 G/V_p \quad (4.6)$$

Where ρ_{bulk} is the bulk density and can be calculated $\rho_{bulk} = \frac{\rho_{base\ material}\ d^3}{{d_{tot}}^3}$ (d and d_{tot} are the effective solid thickness and the total thickness of the sample (0.2 cm), (see ref. [44] for equation formulation), $\rho_{base\ material}$ is the true density of the solid material (2.0 g cm^{-3}), and V_p is the volume of the primary scatterer (pores in this case).

For a mass fractal, the surface area can be determined by the following [27]:

$$\frac{total\ surface\ area}{mass\ sample} = \frac{(S_p/V_p)\varphi}{\rho_{bulk}} = \frac{2\pi^2\varphi_p B_{mass-fractal}}{A\rho_{bulk}Qr^{(4-Dm)}} \quad (4.7)$$

Where $B_{mass-fractal}$ is the power-law scaling prefactor obtained from the unified fit, r is 4 Å, *A* is the geometric factor and assumed to be 7.6, see details elsewhere [27].

A carbon black standard (used for the calibration of a Micromeritics' TriStar II gas adsorption analyser) was used as a specific surface are (SSA) reference and measured using SAXS. The SSA (S_{SAXS} = 26 ± 0.5 m^2 g^{-1}) obtained from SAXS is comparable to the SSA acquired by N_2 adsorption (S_{BET} = 21.0 ± 0.75 m^2 g^{-1}) but likely also includes some surface area from closed porosity.

Pore size distributions were determined using the IPG/TNNLS (Internal Point Gradient-Total Non-Negative Least Square) fitting method in Irena [42].

4.2.3 Characterisation of the chemical structure of biochar

A Perkin–Elmer Spectrum GX FT-IR/Raman was used to characterize the chemical structure of biochar, following the procedure described earlier [30]. In brief, the Raman spectrum (800–1800 cm^{-1}) was baseline-corrected and fitted with 10 Gaussian bands at representative wavenumbers. The assigned G_R (1540 cm^{-1}), V_L (1465 cm^{-1}) and V_R (1380 cm^{-1}) bands represent the small aromatic ring systems with 3–5 rings. The D band (1300 cm^{-1}) corresponds to large aromatic ring systems with 6 or more rings. The band area ratio $I_{(GR+VL+VR)}/I_D$ was used to reflect the transformation of aromatic structures in biochar, where an increase of the ratio

represents a growth in the content of large aromatic ring systems (more than 6 rings). The total Raman peak area was also used to characterize the total O-containing functional groups in biochar.

4.3 Results and discussion

4.3.1 Evolution of biochar conversion with time during gasification in H_2O, CO_2 and H_2O/CO_2 at 800°C (biochar A)

The weight losses (conversion level) of biochar samples with increasing gasification/activation time are shown in *Figure* 4. *2*. It is clearly shown that, after gasification/activation at 800°C for the same time, the biochar gasified in H_2O/CO_2 reaches the highest conversion level followed by the H_2O gasified biochar. The biochar gasified in CO_2 shows the lowest conversion level. This indicates that the simultaneous use of H_2O and CO_2 enhances reaction rate, giving rise to a higher rate of biochar conversion than that in the case of using H_2O or CO_2 alone. It also, in turn, indicates that the reactivity of biochar with H_2O is higher than that with CO_2.

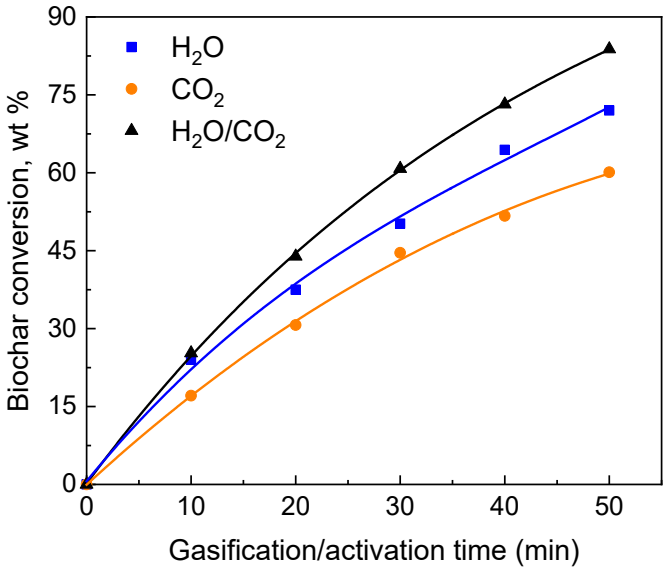

Figure 4. 2. Biochar conversion as a function of gasification/activation time for biochar samples gasified in H_2O, CO_2 and H_2O/CO_2 at 800°C.

4.3.2 Evolution of pore structure in biochar during gasification/activation in H_2O. CO_2 and H_2O/CO_2 at 800°C (biochar A)

4.3.2.1 Evolution of porosity

As stated in our previous work [4], the porosity development during biochar gasification is the result of the creation of micropores and the enlargement of existing pores. New micropores are created by the selective removal of certain carbon atoms by gasifying agents. With the continuous removal of the interior micropore walls, micropores can turn into meso and macropores. The enlargement of pores could also occur when the wall between pores is consumed. These processes take place simultaneously during gasification. Therefore, the observed porosity in biochar at any point is the dynamic balance of pore creation and destruction.

The porosity development of biochar during gasification is paralleled by the evolution of surface area and pore volume with biochar conversion. *Figure* 4. *2* shows the development of SSA as function of biochar conversion level. The values of SSA are similar with those obtained using BET or SSA by others [12,45]. The SSA shows significant growth for both of the H_2O and H_2O/CO_2 gasified biochars, especially in the initial stage of gasification, whereas only a small increase is observed for biochar gasified in CO_2. In general, biochar samples produced by H_2O gasification/activation have a much higher SSA than the CO_2 gasified biochar. The steam gasified biochar achieved the highest SSA of 610 ± 30 $m^2 g^{-1}$ at around 65 wt% conversion before decreasing thereafter when most of the mass was consumed. The H_2O/CO_2 gasification/activation results in similar SSA development to that produced by H_2O gasification/activation.

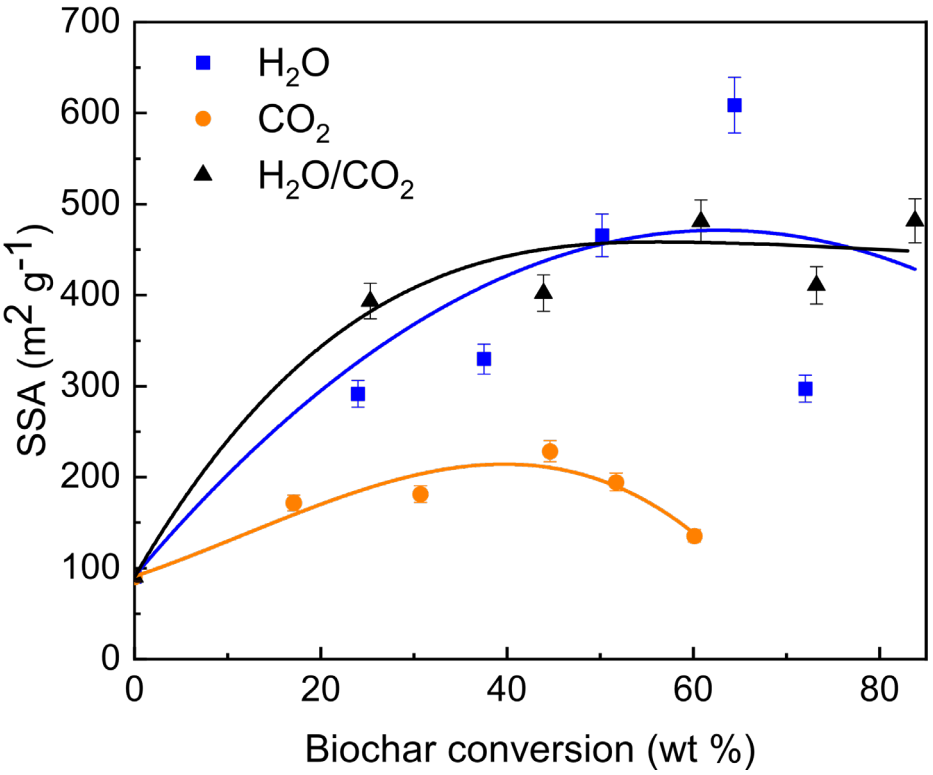

Figure 4. 3. The SSA of biochar samples gasified in H_2O, CO_2 and H_2O/CO_2 as a function of biochar conversion derived from SAXS data.

Figure 4. 4 shows the pore size distribution of biochar samples prepared from gasification/activation in (a) H_2O, (b) CO_2 and (c) H_2O/CO_2 for different times (0, 10, 30 50 min), giving an overall illustration of porosity development in biochar. A distinct feature of all the biochar samples is that there is an abundance of micropores around 1 nm, showing the highly microporous nature of biochar. Another finding is that, regardless of the gasifying agents, the increase in gasification/activation time (conversion level) leads to a wider pore size distribution biased towards larger pore sizes, suggesting the occurrences of pore enlargement with the continuous removal of carbon throughout the process. Moreover, there is a significant initial increase in micropore volume at the early stages (low conversion) of gasification/activation (especially from 0 to 10 min) followed by a decrease at the late stages. This indicates that the creation of micropores is more marked at lower conversion while the enlargement of micropores become the dominant process at higher conversion.

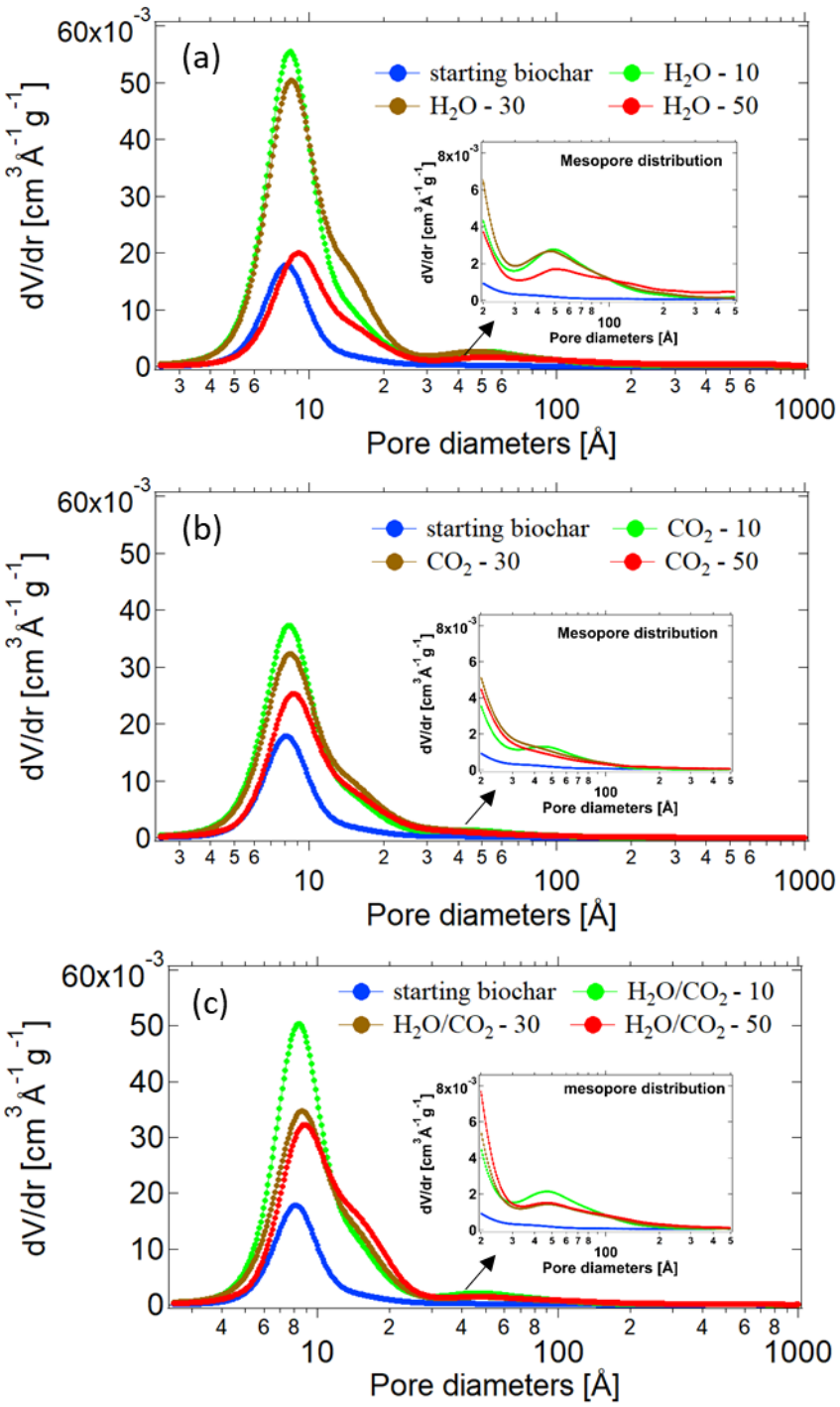

Figure 4. 4. Pore size distribution obtained from the IPG/TNNLS fitting method to SAXS data for biochar samples gasified in (a) H_2O, (b) CO_2 and (c) H_2O/CO_2 over gasification/activation time (10, 30 and 50 min).

To effectively analyse the creation and destruction of pores during gasification/activation, the micro-and mesopore volume (deduced from the unified fit) were plotted as a function of biochar conversion and these are included in *Figure* 4. 5, where the

pore volumes are expressed per g of activated biochar. This can also give a better comparison among different gasifying agents in terms of the differences in porosity development. There is a clear increase in both micro- and mesopore volumes at the early stage of gasification/activation for all the biochar samples gasified in H_2O, CO_2 and H_2O/CO_2. This is also consistent with the size distributions determined earlier. The micropore volume (*Figure* 4. 5a) reaches a maximum after a moderate biochar conversion (around 45-50 wt% coversion) before gradually decreasing. However, the reduction in micropore volume is more remarkable for steam gasified biochar than for biochar prepared from gasification/activation in CO_2 and H_2O/CO_2. The mesopore volume (*Figure* 4. 5b) exhibits an initial growth until around 40-50 wt% conversion followed by a slight decrease thereafter for biochars gasified in H_2O and H_2O/CO_2. The CO_2 gasified biochar shows a small but steady growth in the mesopore volume up to about 60 wt% conversion. Overall, steam gasification/activation gives rise to the most drastic increase of micro- and mesopore volumes whereas CO_2 gasification/activation leads to the smallest growth. The values of micro- and mesopore volume attained from H_2O/CO_2 gasification/activation are, in general, between the values obtained from the analogous experiments with H_2O and CO_2 separately. Similar results were also reported by others [13,15,16,45,46].

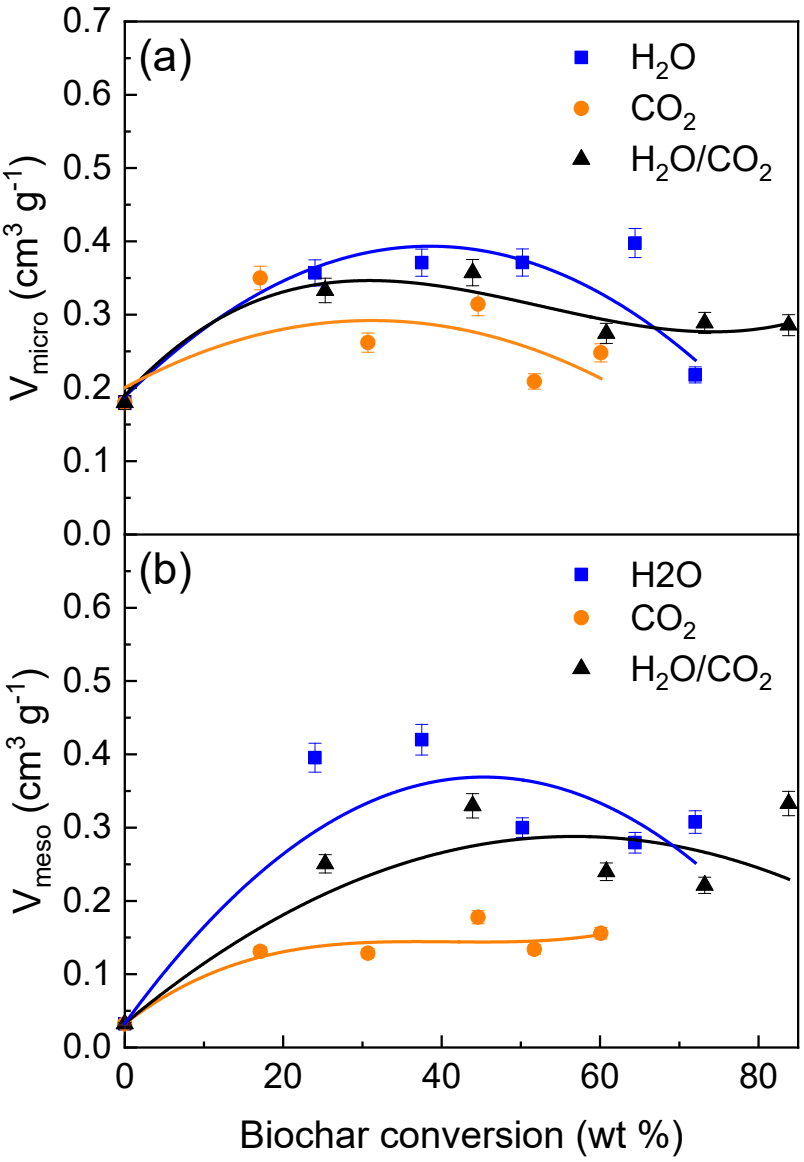

Figure 4. 5. Development of (a) micropore volume and (b) mesopore volume as a function of biochar conversion for biochar samples gasified in H_2O, CO_2 and H_2O/CO_2. The results were extracted from the unified fit to SAXS data.

The porosity evolution indicates that the creation and enlargement of micropores take place from the onset of gasification/activation, leading to the simultaneous development of micro- and mesopores. Consequently, the micro- and mesopore volumes as well as the SSA increased at the early stages of gasification/activation. At the later stages, the process of micropore enlargement become more predominant, converting micropores to meso and macropores, especially in the case of steam gasification. As a result of pore enlargement, a decrease of micropore volume is accompanied by the growth of mesopore volume. Steam

produced an overall higher mesopore volume in biochar compared with CO_2. It seems that the enlargement of micropores is more remarkable during gasification/activation in H_2O than that in CO_2.

Overall, those observation are in line with our previous results [4] revealed by the *in situ* measurements of the pore development during gasification at 800˚C. It appears that there are no obvious changes in biochar structure during cooling down.

4.3.2.2 Evolution of pore network

Biochar is a two-phase system consisting of a carbon skeleton formed by disorderly stacked carbon layers as building blocks that surround pores. The carbon layers consist of defective aromatic structures and are often curved/distorted due to the stresses caused by defects and heterogeneous atoms such as O and N. The curved carbon layers are cross-linked and disorderly stacked, leaving empty spaces of different widths and shapes. The empty voids and interlayer spaces are regarded as the porosity [47,48]. When subjected to gasification/activation, the carbon layers undergo a process of continuous re-combination and re-organisation induced by the selective extraction of carbon atoms and other functional groups by gasifying agents. As carbon layers are reorganised there are simultaneous changes in the distance between the layers, the pore size and morphology. Therefore, the evolution of the pore network illustrates the way in which carbon atoms are removed during gasification/activation.

There is no doubt that the pore network in the micropore size regime is the key to understanding the dominant structure of the carbon skeleton. It is also essential to study the pore network in the mesopore size regime in order to have a complete picture of the evolution pathway of the pore network, especially when considering the transitions from micropore to mesopore and the presence of pore-pore correlations (pore aggregation).

We have previously focussed on the SSA and evolving pore volume from different size regimes. However, it is also important to consider the average pore size and pore morphology in those size regimes. As previously stated, the average pore size is calculated from the radius of gyration in the Guinier regime of the unified fit to SAXS data. *Figure* 4. 6 shows the changes of the radius of gyration (R_{g1} and R_{g2} from the average size of micro- and mesopores, respectively) from the unified fits with increasing biochar conversion. In the micropore size

regime (high q, level 1), the radius of gyration (R_{g1}) increases gradually for biochar gasified in H_2O, CO_2 and H_2O/CO_2. This indicates a consistent enlargement of micropores during gasification/activation, independent of the gasifying agent. This can be explained by the partial removal of the inner pore walls or the collapse of walls between pores, leading to a growth in the average pore size. At the similar conversion level, the mean micropore size is very close for all biochar samples. This is reasonable given that the molecular size of CO_2 (3.3 Å) and H_2O (2.75 Å) is similar.

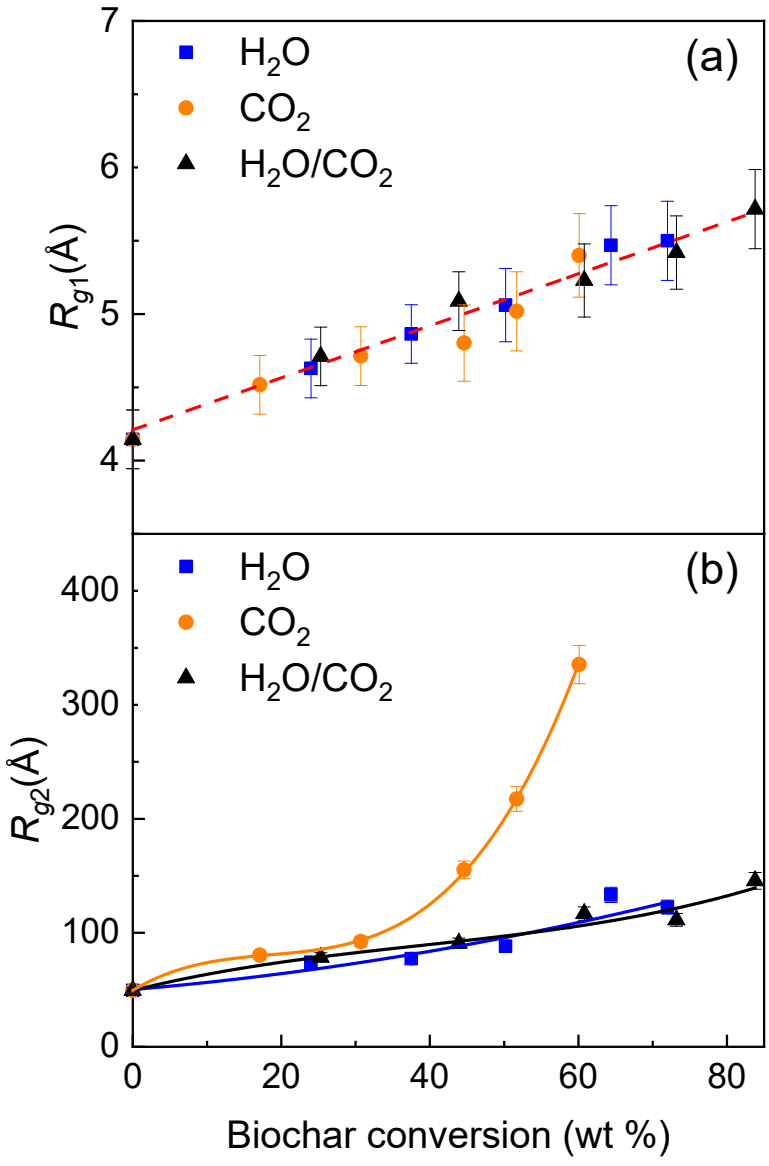

Figure 4. 6. Radius of gyration of biochar as a function of biochar conversion in H_2O, CO_2 and H_2O/CO_2. (a) R_{g1} and (b) R_{g2} were obtained from micro- (level 1 Guinier region) and mesopore size regime (level 2 Guinier region) of the unified fits to SAXS data.

In the mesopore size regime (middle q, level 2), the radius of gyration, R_{g2}, also shows an increasing trend as gasification/activation proceeds. Interestingly, the trends in the case of H_2O and H_2O/CO_2 gasification/activation are similar, whereas CO_2 is markedly different after longer gasification times. After conversion higher that 30 wt%, the increase in R_{g2} during CO_2 gasification/activation (from 90 to 270 Å) is more significant than that during gasification/activation in H_2O and H_2O/CO_2 (from 90 to 120 and 140 Å respectively). The results suggest that the differences in pore development especially in the mesopore size regime between biochar gasified in H_2O or CO_2 become more significant at higher conversion level.

It is better to analyse the pore network by combining the pore size and the texture and morphology of pores given the possibility of pore aggregation. The pore morphology is characterized by the fractal dimension of the pore network. The fractal dimension allows us to "see" how the pores are arranged/distributed spatially and/or their structural makeup. Surface fractal dimension (P lies between 3 and 4) describes the irregularity and roughness of the pore surface, where a dimension of 2 represents a perfectly smooth and sharp interface and a dimension of 3 describes an extremely rough surface. Pore fractals (P falls in between 2 and 3) can be viewed as a "negative image" of mass fractals. The dimension of pore fractal describes the space-filling and branching properties of the pore network [25]. A pore fractal where P approaches 3 describes an extremely disordered pore network in three dimensions that is akin to a sponge-like morphology.

The power law slope (P_2) from the mesopore size regime (middle q, level 2) and the corresponding fractal dimensions are presented in *Table 4. 1*. The mesoporous network of the starting biochar (0 min) exhibits as a pore fractal with a dimension of 2.8, displaying a branched and disordered network of smaller micropores [25]. After being gasified, the pore network of the CO_2 gasified biochar remains as a pore fractal with similar dimensions. In contrast, after 20 wt% of conversion (after 10 min), the fractal pore network in the H_2O and H_2O/CO_2 gasified biochars evolves into a surface fractal with dimension close to 3. This implies that the branched porous network breaks down and becomes dominated by mesopores with an extremely rough surface.

Table 4. 1. Derived power law slope (P_2) from the mesopore size regime (middle q, level 2) and the corresponding fractal dimensions (D_p, D_s) for biochar gasified in H_2O, CO_2 and H_2O/CO_2 at 800°C for different times (0–50 min).

	0 min	10 min	20 min	30 min	40 min	50 min
H_2O						
P_2	2.8	3.3	3.3	3.1	3.0	3.4
Fractal dimension (± 0.05)	D_p = 2.8	D_s = 2.7	D_s = 2.7	D_s = 2.9	D_s = 3.0	D_s = 2.6
CO_2						
P_2	2.8	2.8	2.8	2.6	2.7	2.8
Fractal dimension (± 0.05)	D_p= 2.8	D_p = 2.8	D_p = 2.8	D_p = 2.6	D_p = 2.7	D_p = 2.8
H_2O/CO_2						
P_2	2.8	3.1	3.1	3.0	3.1	3.0
Fractal dimension (± 0.05)	D_p = 2.8	D_s = 2.9	D_s = 2.9	D_s = 3.0	D_s = 2.9	D_s = 3.0

A combination of the parameters from the micro- and mesopore size regimes provides a clearer picture of the pore network evolution. *Figure* 4. 7 provides a schematic diagram illustrating the evolution of pore network in biochar gasified in H_2O and CO_2. It should be noted that the pore network of H_2O/CO_2 gasified biochar evolves in a similar manner to H_2O gasified biochar and is not explicitly shown in *Figure* 4. 7. Before gas treatment, the biochar possesses a considerable fraction of pore channels (pore fractal) forming a network that criss-crosses the solid carbon framework (showed in black in *Figure* 4. 7a). The channels are formed from the aggregation of primary micropores with a radius of gyration R_{g1}. Therefore, the average channel width can be represented by the value of R_{g1} (4.2 ± 0.2 Å). Those branched channels are embedded in the solid and connected, forming a pore-fractal like network. The overall network is fractal at the mesoscopic length scale and the average size of

the network (or cluster) has a radius of gyration R_{g2} (a correlation length that limits the extension of the order). Essentially, this network results in a sponge-like porous solid.

In the case of CO_2 gasification/activation (*Figure* 4. 7b), the pore network remains as a pore fractal over conversion, with a slight increase in the pore channel width (increase of R_{g1} from 4.2 to 5.4 ± 0.2 Å). A significant change is that the pore fractal regime extends to a larger length scale (power law scaling across a wider range of q, marked with dashed arrows), as indicated by the increase of R_{g2} (from 50 ± 2.5 to 266 ± 13.3 Å). Therefore, after 60 wt% of conversion in CO_2 results in an extended network of pores (larger clusters of pore channels). The average size of the new network of micropores (that clusters into a mesopore) is at least five times as large as that of the original one. The results indicate that CO_2 molecules tend to remove pore walls through the existing channels and extend the pore network. Hence, the local etching and collapse of pore walls is the main process during CO_2 gasification/activation. As a result, an extended network of branched micropore clusters is formed. It should be noted that the pore fractal could turn into surface fractal at a higher conversion level (after 50 min) when the channel walls break down to a point where they become part of a rough mesopore surface.

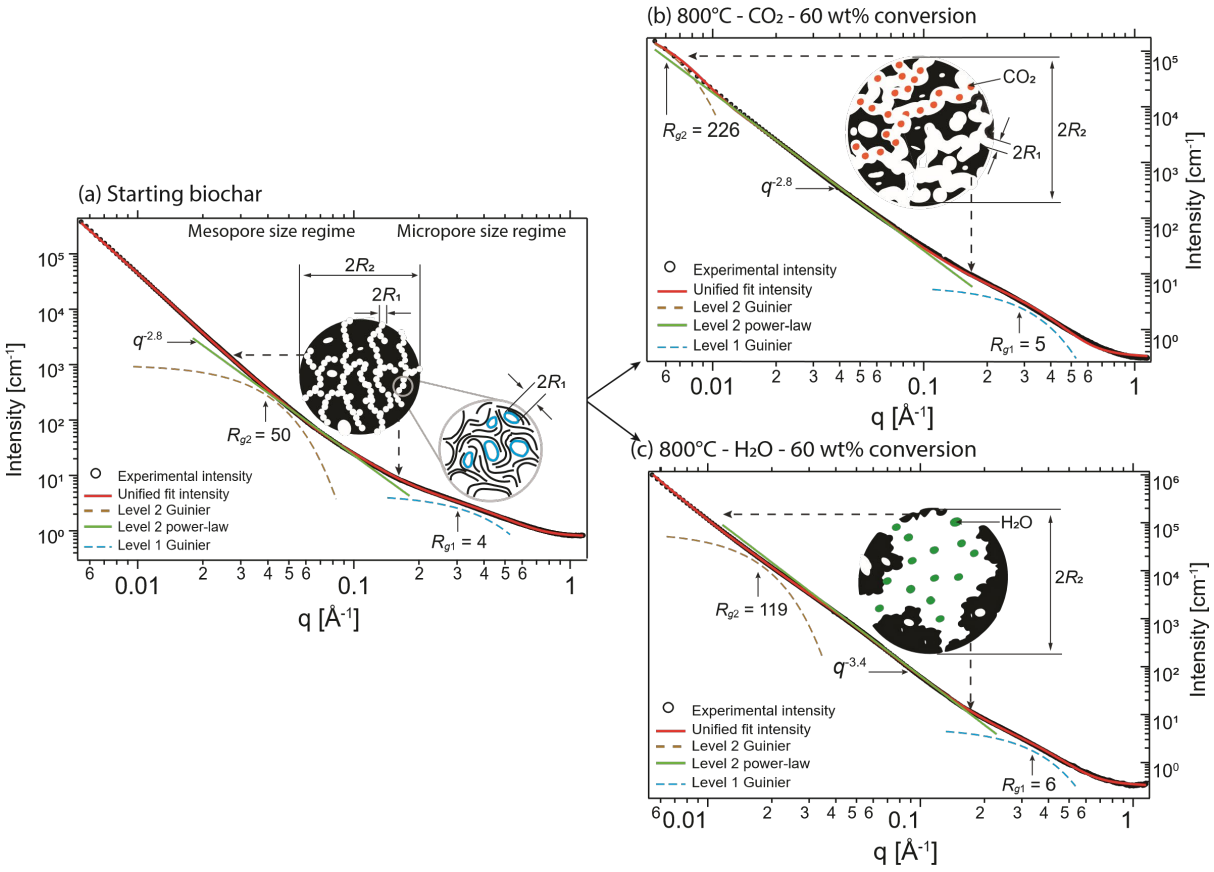

Figure 4. 7. Fitted SAXS patterns along with schematic representations of the fractal network in the mesopore size regime (middle *q*, level 2) for (a) biochar precursor, (b) biochar gasified in CO_2 to around 60 wt% conversion and (c) biochar gasified in H_2O to about 60 wt% conversion. The microstructural features on micro- and mesoscopic length scales are shown by R_{g1} and R_{g2} (± 0.5 Å). The dashed arrows indicate the symbolic range (the relative length scale of fractal network) of the respective power law regime at middle *q* (level 2). Note: the radius of pores can be calculated through $r = \sqrt{5/3}\ R_g$ if the pores are spherical.

In the case of H_2O gasification/activation (*Figure* 4. 7c), a slight increase in the micropore size (measured by R_{g1}) is also observed. More importantly, the pore network transforms from pore fractal to surface fractal with a dimension near 3, representing mesopores with extremely rough surfaces (consisting of an old network of micropores that has been etched into a larger mesopore). The average size of the mesopores (measured by R_{g2}) gradually increases with the extension of biochar conversion. During the process, considerable solids are removed from the sponge-like clusters, leaving behind a larger mesopore with little solids across the pore (instead, showing rough surfaces, *Figure* 4. 7c).

The mechanism could be the removal of layer after layer of carbon and/or the growth of pores of various sizes, giving rise to the collapse and destruction of channel walls. As a consequence, the widening of micropores into the mesopore range is more prevalent, explaining the more significant decrease in the micropore volume along with the higher mesopore volume for H_2O gasified biochar (*Figure* 4. 4). The results imply that carbon removal during gasification in H_2O is less selective than that in CO_2. H_2O molecules attack carbon sites in biochar located almost anywhere.

4.3.2.3 Correlations between the pore structure and the chemical structure of biochar

The SAXS data revealed that the evolutionary pathway of pore structure for H_2O gasified biochar is different from biochar gasified in CO_2. The differences become more significant after 40-50 wt% of conversion (30 minutes of reaction). Moreover, pore development in H_2O/CO_2 gasified biochar follows a similar pattern to H_2O gasified biochar. The pore evolution is either more selective (CO_2), resulting in larger networks of micropores, or less selective (H_2O), resulting in a breakdown of micropore clusters into mesopores. To have a better understanding of the correlation between the pore structure and the underlying carbon skeleton in biochar, the transformation of the carbon skeleton in biochar was also characterized using FT-Raman spectroscopy. *Figure* 4. 8a shows the changes of the band ratio $I_{(Gr+Vl+Vr)}/I_D$ with biochar conversion. Decreases in the band ratio indicate that small aromatic ring systems (less than 6 fused rings) are and preferentially consumed and/or converted to larger ones [30]. During biochar gasification/activation, some atoms such as O are preferably removed, inducing the growth of the aromatic structures, presumably through a carbon re-combination process. However, judging from the band area ratio, it can be seen that the aromatic structures in H_2O gasified biochar change differently to those in CO_2 gasified biochar. This indicates differences in carbon sites preferably attacked by H_2O and CO_2 molecules, causing the different structural evolution of biochar under these gases. The aromatic structures in biochar gasified in H_2O/CO_2 and H_2O are similar, suggesting a reason why similar pathways of carbon removal are seen under H_2O/CO_2 and H_2O. The development of the pore structure produced by various gasifying agents is paralleled by the evolution of the aromatic structures characterized by Raman spectroscopy. Therefore, the evolution of the aromatic structures can be used as a guide to understanding the changes in the pore structure of biochar.

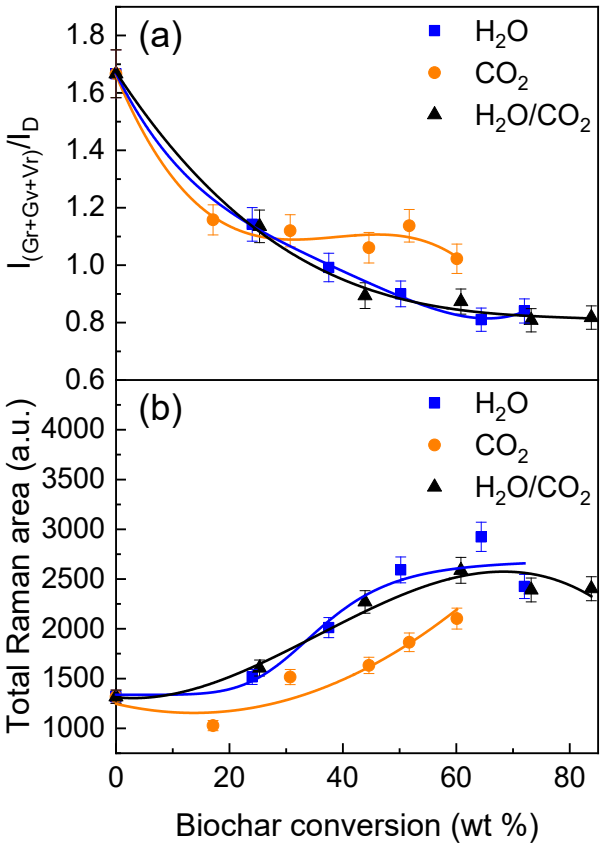

Figure 4. 8. Raman spectroscopic data. (a) the ratio of band areas $I_{(Gr+Vl+Vr)}/I_D$ and (b) the total Raman peak area (800 – 1800 cm^{-1}) of biochar as a function of biochar conversion.

The explanation for the differences in the porous structure of biochar developed by H_2O and CO_2 is complex. As stated before, pore structure evolvement in biochar is the result of the selective consumption of carbon atoms during gasification/activation. Therefore, the differences in the evolution of pore structure between H_2O and CO_2 gasified biochar is a result of the different selectivity in carbon consumption by each gas, which depends on variations in the reactivity between biochar with H_2O and CO_2.

One of the reasons for the different reactivity between H_2O-char and CO_2-char reactions could be the different reactivity of H_2O and CO_2 [14,15,49]. For a given temperature, H_2O is more reactive than CO_2 as a higher energy is needed to dissociate a CO_2 molecule than that for a H_2O molecule [14,15]. Thus, H_2O molecules are less selective than CO_2 molecules in attacking carbon atoms. H_2O-char reactions would take place at an extensive number of active

sites whilst the active sites that are appropriate for CO_2-char reactions are limited. Accordingly, H_2O molecules tend to interact with active sites located almost anywhere within the porous structure. Whereas the local etching in existing pore channels is a more prevalent process during gasification/activation with CO_2.

Another possible reason for the differences in carbon selectivity between H_2O and CO_2 could be related to the amount and properties of O-containing functional groups on the biochar surface [17]. The continuous formation and decomposition of O-containing functional groups is an important feature of gasification reactions [46]. Some of these O-containing functional groups behave as reaction intermediates in gasification/activation processes. Along the gasification/activation pathway, oxygen is firstly adsorbed on the carbon surface and then removed along with the carbon atoms to which the oxygen is attached [17]. As the process repeats, a certain degree of porosity in biochar is achieved. The evolution of the O-containing functional groups in biochar was characterized using Raman spectroscopy [30] and included in *Figure* 4. 8b. The content of O-containing functional groups is higher (indicated by the higher total Raman area) in biochar produced by H_2O than CO_2. This is expected since the reactivity of gases with biochar is associated with the amount of O-containing functional groups [17,31,32,35]. When H_2O is used, more surface O-containing functional groups are formed and a greater number of active sites are available for H_2O-char reactions to take place. In other words, the elimination of carbon by H_2O would take place at more sites in the carbon network. Whereas in CO_2, the lower content of O-containing functional groups limits where carbon atoms can be extracted. The content of O-containing functional groups in biochar produced in H_2O/CO_2 is nearly identical to that in H_2O gasified biochar, indicating that the process of carbon removal by H_2O could be the dominant process. This explains the similarity in how the pore structure evolves between biochar gasified in H_2O and H_2O/CO_2. Additionally, our previous work [35] found that different types of O-containing functional groups are formed in biochar during gasification with H_2O or CO_2. The different thermal stabilities of various O-containing functional groups could also be one of the reasons for the selective removal of carbon, as the relatively less stable O-containing functional groups would be decomposed first. Therefore, the amount and type of O-containing groups in biochar affect the selection of carbon atoms during gasification/activation reactions, thereby controlling the pathways of pore structure evolution and hence the final porosity developed.

Since the nature of gasification/activation lies in the selectivity of carbon consumption, it is reasonable to assume that gasifying agents tend to attack the relatively more reactive and less stable structures. Accordingly, the weak pore walls would be removed in preference to the relatively strong walls. As carbon conversion proceeds, the selectivity for the remnant structures by H_2O and CO_2 would become more pronounced as they become, on average, more stable and less reactive.

4.3.3 Effects of temperature and biomass particle sizes on the pore structure of biochar

Figure 4. *9* shows some major pore structure parameters acquired from SAXS measurements for biochar gasified at different temperatures for 4 minutes (biochar B). Overall, the increase of temperature gives rise to a significant increase in SSA and pore volume as the biochar conversion increases, especially the mesopore volume, irrespective of the type of gasifying agent. It seems that the development of both micro- and mesopores is enhanced with increasing temperature. This could be attributed to the enhanced thermal breakdown and the higher reaction rate at higher temperature, leading to a higher level of biochar conversion. The average size of micro- and mesopores are similar for biochars gasified at different temperatures. Moreover, when the temperature increased from 700 to 900 ˚C, the values of micro- and mesopore volumes produced by H_2O and CO_2 become more similar when the biochar conversion reached a similar level (7% and 8% of char yield were obtained for biochar gasified in CO_2 and H_2O). The decreased differences in porosity development between H_2O and CO_2 gasified biochar suggests that the differences in carbon removal by H_2O and CO_2 becomes less significant at higher temperature. At an elevated temperature, the reaction rate of carbon sites with H_2O or CO_2 increases rapidly especially for those carbon sites with higher activation energies [4]. When different carbon sites have closer gasification rates, carbon removal become less selective. As a result, the differences in the pore structure of biochar produced by H_2O and CO_2 become smaller.

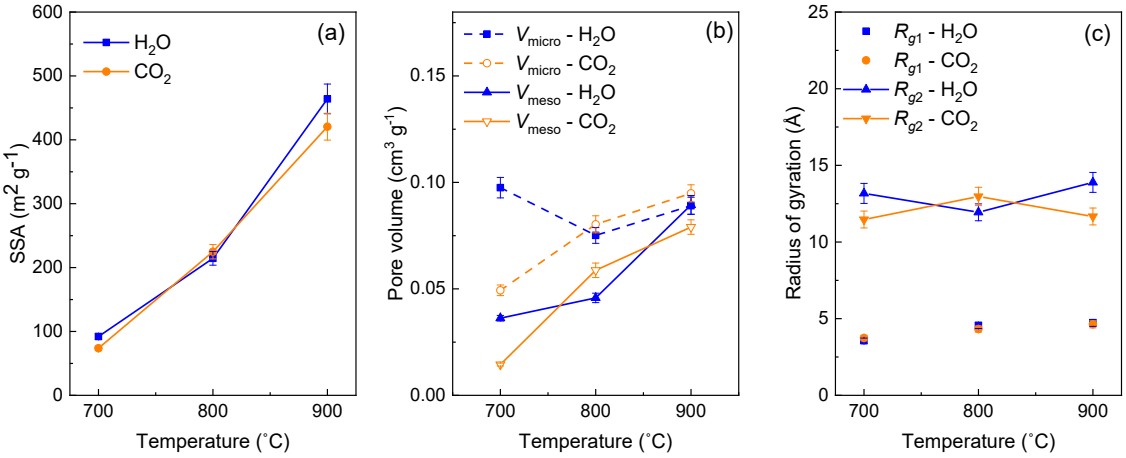

Figure 4. 9. SAXS derived (a) SSA, (b) pore volume and (c) radius of gyration for biochar gasified in H_2O (closed symbols) and CO_2 (open symbols) at different temperatures (700, 800 and 900 ˚C).

Figure 4. 10 shows the SAXS curves of biochar samples prepared from Mallee wood with various particle sizes (biochar C). As expected, for gasification both in H_2O and CO_2, little change in the SAXS patterns among different biomass particle sizes is observed. This demonstrates that the biomass particle size has almost no effect on the pore structure development. In our previous study [36], the Raman characterization of samples with different particle sizes revealed that there is no significant changes in the aromatic ring systems and the content of O-containing functional groups in biochar. The results, therefore, again confirm that the evolution of pore structure in biochar is closely linked to the changes in the aromatic ring systems and the O-containing functional groups. The gasifying agents and gasification temperature are the most important in defining the gasification reactions and processes rather than bulk particle size of biomass feedstock.

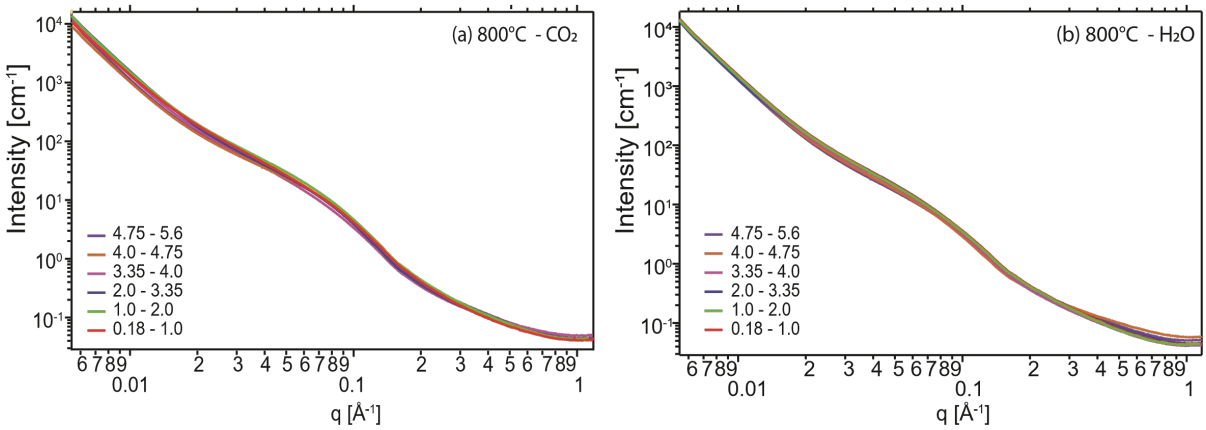

Figure 4. 10. SAXS curves of biochar gasified in (a) CO_2 and (b) H_2O with biomass of different particle sizes (mm).

4.4 Conclusions

The evolution of the pore structure in biochar during gasification/activation in H_2O, CO_2 and H_2O/CO_2 was investigated using SAXS. The three gasifying agents develop micro- and mesopores in biochar through different mechanisms that can be visualised from SAXS analysis. The overall pore development in H_2O/CO_2 gasified biochar is akin to that in H_2O gasified biochar. The CO_2 activated biochars display pore fractal features (representing a network of branched micropore clusters) in the mesopore size regime up to a 60 wt% conversion. An increase in conversion level gives rise to a remarkable growth in the size of the pore fractal network. Whereas for the H_2O gasified biochar, the mesoporous network is dominated by mesopores with extremely rough surfaces after 10 min gasification (conversion level higher than 20 wt%), presenting as surface fractals, rather than networks of micropores. The development of the pore structure produced by various gasifying agents is paralleled by the evolution of the aromatic structures characterized by Raman spectroscopy. The different porous structure of biochar from H_2O and/or CO_2 gasification/activation is a consequence of the differences in carbon removal by H_2O and CO_2, which is determined by the reactivity of various carbon sites with H_2O and CO_2. Carbon removal in biochar is less selective when gasified with H_2O than with CO_2. This could be due to the higher content of O-containing functional groups in H_2O gasified biochar, together with higher reactivity of H_2O. Besides, the differences in pore structure caused by H_2O and CO_2 decreases at higher temperature. The

pore structure of biochar is barely affected by the biomass particle sizes. These findings provide valuable information for a deeper understanding of gasification process as well as for optimizing the preparation conditions of activated carbons.

4.5 References

[1] Li C-Z. Special issue—gasification: a route to clean energy. Process Saf Environ Prot 2006;84:407–8.

[2] Li C-Z. Importance of volatile-char interactions during the pyrolysis and gasification of low-rank fuels - A review. Fuel 2013;112:609–23.

[3] Foster MD, Jensen KF. SAXS investigation of model carbon pore structure and its change with gasification. Carbon N Y 1991;29:271–82.

[4] Liu Y, Paskevicius M, Sofianos MV, Parkinson G, Li C-Z. In situ SAXS studies of the pore development in biochar during gasification. Carbon N Y 2021;172:454–62.

[5] Qian K, Kumar A, Zhang H, Bellmer D, Huhnke R. Recent advances in utilization of biochar. Renew Sustain Energy Rev 2015;42:1055–64.

[6] Hurt RH, Sarofim AF, Longwell JP. Effect of Nonuniform Surface Reactivity on the Evolution of Pore Structure and Surface-Area During Carbon Gasification. Energy & Fuels 1991;5:463–8.

[7] Gibaud A, Xue JS, Dahn JR. A small angle X-ray scattering study of carbons made from pyrolyzed sugar. Carbon N Y 1996;34:499–503.

[8] Arenas E, Chejne F. The effect of the activating agent and temperature on the porosity development of physically activated coal chars. Carbon N Y 2004;42:2451–5.

[9] Ostafiychuk BK, Mandzyuk VI, Kulyk YO, Nagirna NI. SAXS investigation of nanoporous structure of thermal-modified carbon materials. Nanoscale Res Lett 2014;9:160.

[10] McEnaney B, Mays TJ. Chapter 5 – Porosity in Carbons and Graphites. Butterworth & Co. (Publishers) Ltd; 1989.

[11] Guizani C, Jeguirim M, Gadiou R, Escudero Sanz FJ, Salvador S. Biomass char gasification

by H_2O, CO_2 and their mixture: Evolution of chemical, textural and structural properties of the chars. Energy 2016;112:133–45.

[12] Coetzee GH, Sakurovs R, Neomagus HWJP, Morpeth L, Everson RC, Mathews JP, Bunt JR. Pore development during gasification of South African inertinite-rich chars evaluated using small angle X-ray scattering. Carbon N Y 2015;95:250–60.

[13] Rodríguez-Reinoso F. Controlled gasification of carbon and pore structure development. In: Lahaye J. EP, editor. Fundam. Issues Control Carbon Gasif. React., Springer, Dordrecht; 1991, p. 533–71.

[14] González JF, Román S, González-García CM, Nabais JMV, Ortiz AL. Porosity development in activated carbons prepared from walnut shells by carbon dioxide or steam activation. Ind Eng Chem Res 2009;48:9354.

[15] Rodríguez-Reinoso F, Molina-Sabio M, González MT. The use of steam and CO_2 as activating agents in the preparation of activated carbons. Carbon N Y 1995;33:15–23.

[16] Pastor-Villegas J, Durán-Valle CJ. Pore structure of activated carbons prepared by carbon dioxide and steam activation at different temperatures from extracted rockrose. Carbon N Y 2002;40:397–402.

[17] Molina-Sabio M, González MT, Rodriguez-Reinoso F, Sepúlveda-Escribano A. Effect of steam and carbon dioxide activation in the micropore size distribution of activated carbon. Carbon N Y 1996;34:505–9.

[18] Alcañiz-Monge J, Cazorla-Amorós D, Linares-Solano A, Yoshida S, Oya A. Effect of the activating gas on tensile strength and pore structure of pitch-based carbon fibres. Carbon N Y 1994;32:1277–83.

[19] Wigmans T. Industrial aspects of production and use of activated carbons. Carbon N Y 1989;27:13–22.

[20] Walker PL. Production of activated carbons: use of CO_2 versus H_2O as activating agent. Carbon N Y 1996;34:1297–9.

[21] Pastor AC, Marsh H. Preparation of activated carbon cloths from viscous rayon. Part II : physical activation processes. Carbon N Y 2000;38:379–95.

[22] Bahadur J, Medina CR, He L, Melnichenko YB, Rupp JA, Blach TP, Mildner DFR. Determination of closed porosity in rocks by small-angle neutron scattering. J Appl Crystallogr 2016;49:2021–30.

[23] Härk E, Petzold A, Goerigk G, Risse S, Tallo I, Härmas R, Lust E, Ballauff M. Carbide derived carbons investigated by small angle X-ray scattering: Inner surface and porosity vs. graphitization. Carbon N Y 2019;146:284–92.

[24] Pfeifer P. Fractal dimension as working tool for surface-roughness problems. Appl Surf Sci 1984;18:146–64.

[25] Pfeifer P, Ehrburger-Dolle F, Rieker TP, González MT, Hoffman WP, Molina-Sabio M, Rodríguez-Reinoso F, Schmidt PW, Voss DJ. Nearly space-filling fractal networks of carbon nanopores. Phys Rev Lett 2002;88:115502.

[26] Bale HD, Schmidt PW. Small-Angle X-Ray-Scattering Investigation of Submicroscopic Porosity with Fractal Properties. Phys Rev Lett 1984;53:596–9.

[27] Beaucage G, IUCr. Small-Angle Scattering from Polymeric Mass Fractals of Arbitrary Mass-Fractal Dimension. J Appl Crystallogr 1996;29:134–46.

[28] Beaucage G. Determination of branch fraction and minimum dimension of mass-fractal aggregates. Phys Rev E - Stat Physics, Plasmas, Fluids, Relat Interdiscip Top 2004;70:10.

[29] Reich MH, Russo SP, Snook IK, Wagenfeld HK. The application of SAXS to determine the fractal properties of porous carbon-based materials. J Colloid Interface Sci 1990;135:353–62.

[30] Li X, Hayashi J-I, Li C-Z. Volatilisation and catalytic effects of alkali and alkaline earth metallic species during the pyrolysis and gasification of Victorian brown coal. Part VII. Raman spectroscopic study on the changes in char structure during the catalytic gasification in air. Fuel 2006;85:1509–17.

[31] Liu Y, Paskevicius M, Wang H, Parkinson G, Veder JP, Hu X, Li C-Z. Role of O-containing functional groups in biochar during the catalytic steam reforming of tar using the biochar as a catalyst. Fuel 2019;253:441–8.

[32] Liu Y, Paskevicius M, Wang H, Fushimi C, Parkinson G, Li C-Z. Difference in tar reforming activities between biochar catalysts activated in H_2O and CO_2. Fuel 2020;271:117636.

[33] Advanced biomass gasification technology, Australian Renewable Energy Agency.

[34] Grinding pyrolysis, Renergi Pty Ltd. http://www.renergi.net/grinding_pyrolysis. (accessed December 20, 2020).

[35] Wang S, Wu L, Hu X, Zhang L, O'Donnell KM, Buckley CE, Li C-Z. An X-ray photoelectron spectroscopic perspective for the evolution of O-containing structures in char during gasification. Fuel Process Technol 2018;172:209–15.

[36] Wang S, Wu L, Hu X, Zhang L, Li T, Li C-Z. Effects of the particle size and gasification atmosphere on the changes in the char structure during the gasification of mallee biomass. Energy and Fuels 2018;32:7678–84.

[37] Kirby NM, Mudie ST, Hawley AM, Cookson DJ, Mertens HDT, Cowieson N, Samardzic-Boban V. A low-background-intensity focusing small-angle X-ray scattering undulator beamline. J Appl Crystallogr 2013;46:1670–80.

[38] Dreiss CA, Jack KS, Parker AP. On the absolute calibration of bench-top small-angle X-ray scattering instruments: A comparison of different standard methods. J Appl Crystallogr 2006;39:32–8.

[39] Spalla O, Lyonnard S, Testard F. Analysis of the small-angle intensity scattered by a porous and granular medium. J Appl Crystallogr 2003;36:338–47.

[40] SAXS Software - scatterBrain.

[41] Beaucage G. Approximations leading to a unified exponential power-law approach to small-angle scattering. J Appl Crystallogr 1995;28:717–28.

[42] Ilavsky J, Jemian PR. Irena : tool suite for modeling and analysis of small-angle scattering. J Appl Crystallogr 2009;42:347–53.

[43] Hurd AJ, Schaefer DW, Smith DM, Ross SB, Le Méhauté A, Spooner S. Surface areas of fractally rough particles studied by scattering. Phys Rev B 1989;39:9742–5.

[44] Paskevicius M. A nanostructural investigation of mechanochemically synthesised hydrogen storage materials, PhD thesis, Curtin University of Technology, Australia. 2009.

[45] Román S, González JF, González-García CM, Zamora F. Control of pore development

during CO_2 and steam activation of olive stones. Fuel Process Technol 2008;89:715–20.

[46] Marsh H, Rodríguez-Reinoso F. CHAPTER 5 - Activation Processes (Thermal or Physical). In: Marsh H, Rodríguez-Reinoso FBT-AC, editors. Act. Carbon, vol. 2, Elsevier Science & Technology Books; 2006, p. 243–321.

[47] Marsh H, Rodríguez-Reinoso F. CHAPTER 2 - Activated Carbon (Origins). In: Marsh H, Rodríguez-Reinoso FBT-AC, editors. Act. Carbon, Oxford: Elsevier Science & Technology Books; 2006, p. 13–86.

[48] Jafta CJ, Petzold A, Risse S, Clemens D, Wallacher D, Goerigk G, Ballauff M. Correlating pore size and shape to local disorder in microporous carbon : A combined small angle neutron and X-ray scattering study. Carbon N Y 2017;123:440–7.

[49] González JF, Encinar JM, González-García CM, Sabio E, Ramiro A, Canito JL, Gañán J. Preparation of activated carbons from used tyres by gasification with steam and carbon dioxide. Appl Surf Sci 2006;252:5999–6004.

Chapter 5

Role of O-containing functional groups in biochar during the catalytic steam reforming of tar using the biochar as a catalyst

Y. Liu, M. Paskevicius, H. Wang, G. Parkinson, J.P. Veder, X. Hu, C.-Z. Li, Role of O-containing functional groups in biochar during the catalytic steam reforming of tar using the biochar as a catalyst, Fuel. 253 (2019) 441–448. https://doi.org/10.1016/j.fuel.2019.05.037.

Abstract

Tar formation is practically unavoidable during gasification. Catalytic tar forming is one of the most promising techniques for producing high-quality syngas at a commercial scale. Biochar has great potential to be used as a catalyst for the removal of tar from the syngas produced from the pyrolysis/gasification of biomass. The structure of biochar is a critical factor affecting its catalytic performance. This study investigates the role of O-containing functional groups in biochar during steam reforming of tar using biochar as a catalyst. Mallee wood biochar (106 - 250 um) was activated in H_2O for different times (0 – 50 mins) and then used as a catalyst for the steam reforming of tar at 800 °C. The chemical structural features of biochars were characterized with Raman spectroscopy and X-ray photoelectron spectroscopy (XPS). It was found that H_2O activation increased the concentration of O-containing functional groups, mainly the aromatic C-O structures in biochar, which enhanced the catalytic destruction of tar. During the catalytic reforming of tar, the content of aromatic C-O groups decreased while the catalyst activity decreased. It is believed that the aromatic C-O functional groups in biochar play a vital role in the steam reforming of tar.

5.1 Introduction

The presence of tar in the syngas during gasification is one of the major factors limiting the commercialization of many biomass gasification technologies. The condensation and polymerization of tar in downstream equipment can easily cause plugging and subsequent shutdown of the entire system [1–3]. Therefore, tar removal from the product gas is crucial for the development and commercialization of gasification technologies.

Generally, key technologies of removing tar are classified into physical treatment using scrubbers or filters [4,5], cleaning using plasma [6], and thermochemical conversion methods that convert tar into syngas through thermal cracking at high temperature or catalytic reforming using a catalyst [7–9]. Among these methods, catalytic steam reforming has been considered as one of the most attractive techniques due to its high efficiency. Moreover, during this process, the conversion of tar can produce more useful gases (H_2, CO and CH_4) [3,10,11].

Various catalysts including nickel-based catalysts, zeolite, dolomite, alkali metals and biochar have been widely employed in the catalytic steam reforming of tar [7,12–16]. Compared with other catalysts, biochar has attracted more attention recently not only because it shows a high catalytic activity for tar destruction, but also due to its low cost and the fact that it can be continuously produced inside the gasifier. Furthermore, the deactivated biochar catalyst can be directly burned or gasified without the need of expensive disposal while its energy value is recovered [13,17,18]. Studies have shown that the catalytic activity of biochar for tar destruction relates to the porous structure (large specific surface area), the characteristics of inherent alkali and alkaline earth metallic (AAEM) species, as well as its amorphous carbon structures [18,19]. However, the exact catalytic mechanism of tar reforming over biochar remains unclear, primarily due to the chemical complexity of tar compounds and biochar structure. The biochar produced from gasification usually has a high content of O-containing functional groups, making the biochar extremely active [20]. However, the role of O-containing functional groups in biochar in the catalytic conversion of tar remains unclear.

While our previous studies have identified the importance of O-containing functional groups in biochar catalyst to its catalytic activity during the catalytic reforming of tar [9,18], it remains unclear as to the specific structures/types of O-containing functional groups that are important for its catalytic activity. More importantly, it remains unclear how these catalytically active O-containing functional groups in biochar might change/evolve during the reforming process. To further investigate the exact role of various O-containing functional groups of biochar in tar conversion, herein we have studied the changes in biochar structure during the reforming of tar with an emphasis on the relation between the O-containing functional groups in biochar and its catalytic activity in the destruction of tar.

5.2 Experimental

5.2.1 Biochar and bio-oil samples

Biochar sample was obtained from the pyrolysis of Mallee biomass and its subsequent gasification in Renergi's gasification demonstration plant at Curtin University, Australia

[21,22]. It should be noted that the gasification of this sample took place for only about 5-10 minutes at 750 - 850 °C. The biochar sample was sieved to obtain a particle size distribution of 106 - 250 µm. A part of the sieved biochar was activated in 15 vol. % H_2O balanced with argon at 800 °C for different times (10-50 mins) before being used as a catalyst for tar reforming. These treated biochar samples are termed as activated biochar. The biochar sample without pretreatment in steam was referred to as raw biochar in this study. The chemical analysis of the raw biochar and activated biochar samples with different activation times is shown in *Table 5. 1*.

Bio-oil was produced from the pyrolysis of Mallee biomass from the Renergi's grinding pyrolysis pilot plant [22]. In this work, the bio-oil was used to generate volatiles (including tar) that would be reformed using the biochar samples as catalysts. Biomass pyrolysis and the succeeding reforming of bio-oil is also an attractive route for syngas production. The properties of bio-oil used in this work are also included in *Table 5. 1*.

Table 5. 1. Elemental analysis of biochar catalysts and bio-oil.

	Elemental analysis (daf basis)			
	C	H	N	O[a]
Raw biochar (0 min activated)	91.5	1.0	0.7	6.8
10 mins activated biochar	96.4	0.3	0.3	3.0
20 mins activated biochar	95.7	0.2	0.4	3.7
30 mins activated biochar	91.9	0.4	0.3	7.4
40 mins activated biochar	90.4	0.5	0.2	8.9
50 mins activated biochar	88.5	0.1	0.2	11.2
Bio-oil	58.5	6.7	0.4	34.5

daf: dry and ash free, [a] by difference.

Note: no sulphur was detected in all biochar and bio-oil samples

5.2.2 Steam reforming of tar using biochar as a catalyst

A three-frit two-stage fluidized-bed/fixed-bed quartz reactor [23,24] was used for the catalytic steam reforming of tar, as is shown in *Figure* 5. *1*. The flow rate of the feeding gas (argon) and fluidizing gas (argon) was fixed at 1.0 L min^{-1} and 0.7 L min^{-1} respectively. Before heating up the reactor in a furnace, biochar catalyst was preloaded on the middle frit. 1 g of raw or activated biochar was used in each experiment. It should be noted that the activated biochar samples were activated *in-situ* using the same reactor prior to starting the reforming experiments.

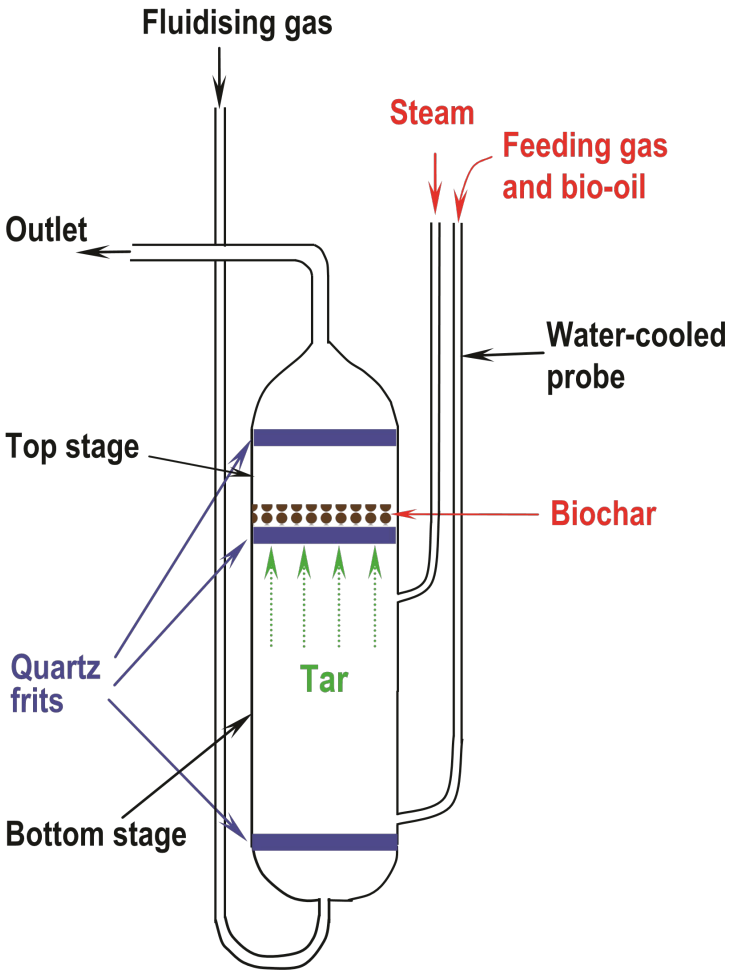

Figure 5. 1. A schematic diagram of the three-frit fluidized-bed/fixed-bed quartz reactor (modified from Ref. [23] with permission from Elsevier).

The reforming experiments were performed at 800 °C. After the temperature inside the reactor had raised to and stabilized at 800 °C, 15 vol. % steam of the total gas flow was generated by continually injecting deionized water (beneath the middle frit) using a high performance liquid chromatography (HPLC) pump. At the same time, bio-oil was also fed into the reactor with an HPLC pump through a water-cooled probe at 0.20 ml min^{-1}. The generated volatiles from bio-oil were mixed with steam before passing through the biochar bed. The reforming time of tar over biochar was controlled by the feeding times of bio-oil and steam.

At the final stage, the reactor was elevated out of the furnace to terminate the experiment after stopping feeding bio-oil and steam. Argon gas continued to pass through the reactor until the reactor was cooled to room temperature. To facilitate comparison, two control experiments were also carried out without using biochar as a catalyst whilst keeping other conditions the same.

5.2.3 Tar sampling and analysis

Tar was condensed and collected by passing the outlet gas through three traps filled with 50, 40 and 30 ml HPLC-grade $CHCl_3$/CH_3OH mixture (4:1 by vol) respectively [8]. The first trap was put in an ice-water bath (0 °C) and the last two traps were placed in a dry ice bath (-78 °C). After the completion of a reforming experiment, these tar solutions were collected for further analysis. A detailed description of this method of tar capture can be found in our previous studies [8,25].

As described previously [8,24,26], tar yield was determined by measuring the concentration of tar dissolved in the chloroform/methanol solvent. Tar is experimentally defined as the material soluble in the chloroform/methanol mixture that does not evaporate at 35 °C within 4 h. A blank experiment was also carried out to exclude the non-evaporative residues in the solvents themselves. Tar yield is defined as the ratio of the amount of tar to the amount of bio-oil used in the experiments.

An UV-fluorescence spectroscopy (Perkin-Elmer LS50B spectrometer) was used to characterize the collected tar samples. The synchronous spectra were recorded with a slit width of 2.5 nm and a scan speed of 200 nm min^{-1} at a constant energy difference of -2800 cm^{-1}. Before characterization, the tar solutions were diluted with methanol (Uvasol for spectroscopy; purity: 99.9% by GC) to 4 ppm (wt). To facilitate comparison, the fluorescence

intensity of the same concentration (4 ppm) was multiplied by the tar yield to be presented on the same basis of per gram of bio-oil [27,28]. The ‘‘wavelength’’ in the spectra briefly indicates the relative sizes of the aromatic rings (e.g., <290 nm corresponds to mono-aromatics, 290–320 nm represents for aromatic compounds containing two fused rings, etc.), although a strict correlation between wavelength and the size of aromatic ring is impossible [8,27].

5.2.4 Characterization of biochar

Raman spectroscopy has been extensively employed to identify the chemical structures of biochar [20,29–31]. In this study, a Perkin–Elmer Spectrum GX FT-IR/Raman spectrometer was used to characterize the structural features of the aromatic ring systems and the O-containing functional groups of biochar. The measurement procedure has been described in detail in previous works [20,29]. Briefly, 0.25 wt.% biochar was mixed with KBr and then ground before being scanned for 200 times. Afterwards, the Raman spectrum in the range of 800 - 1800 cm^{-1} was baseline-corrected before being fitted with 10 Gaussian bands. The assigned D band (1300 cm^{-1}) represents for the large aromatic ring systems containing 6 or more rings. The G_R (1540 cm^{-1}), V_L (1465 cm^{-1}) and V_R (1380 cm^{-1}) bands correspond to small aromatic ring systems containing 3-5 rings. The band area ratio $I_{(GR+VL+VR)}/I_D$ reflects the relative content of small and large aromatic ring systems. The total Raman peak area in the range of 800 -1800 cm^{-1} was used to indicate the relative amount of O-containing functional groups that, together with their attached aromatic ring systems, can generate a resonance effect.

Although the relative content of the O-containing functional groups in biochar can be reflected by the total Raman peak area, the evolution of the specific types of O-containing functional groups cannot be obtained by Raman spectroscopy. X-Ray Photoelectron Spectroscopy (XPS) can characterize the elemental composition and the chemical state of elements present on the material surface; it has been widely employed to characterize the composition of various functional groups in biochar. Our previous work [32] has shown that XPS-derived carbon and oxygen relative contents broadly reflect the bulk biochar composition. A Kratos AXIS Ultra DLD XPS spectrometer equipped with an Al-Kα X-ray source (energy

1486.7 eV) was used to study the evolution of O-containing functional groups on biochar surface in this study. An XPS survey spectrum was obtained over an energy range from 0 - 1200 eV. High-resolution spectra of C 1s and O 1s were obtained at a pass energy of 40 eV [33]. The CasaXPS software was used to analyze the obtained XPS spectra. The spectra was calibrated using the adventitious C 1s peak at 284.5 eV. After calibration and Shirley background subtraction, the O 1s spectra were curve-fitted following our previous procedure [32]. The aromatic C=O groups and C-O groups were assigned to 531.4 eV 533.4 eV respectively. The band at 536.0 eV was assigned to the adsorbed oxygen on biochar surface.

It is noteworthy that the conversion level of biochar catalysts after tar reforming couldn't be determined accurately under our experimental conditions. However, the ash yield of biochar after tar reforming was found to stay almost unchanged within experiment error. Thus, the extent of biochar gasification is minimal during tar reforming.

5.3. Results and discussion

5.3.1 Tar destruction using biochar as a catalyst

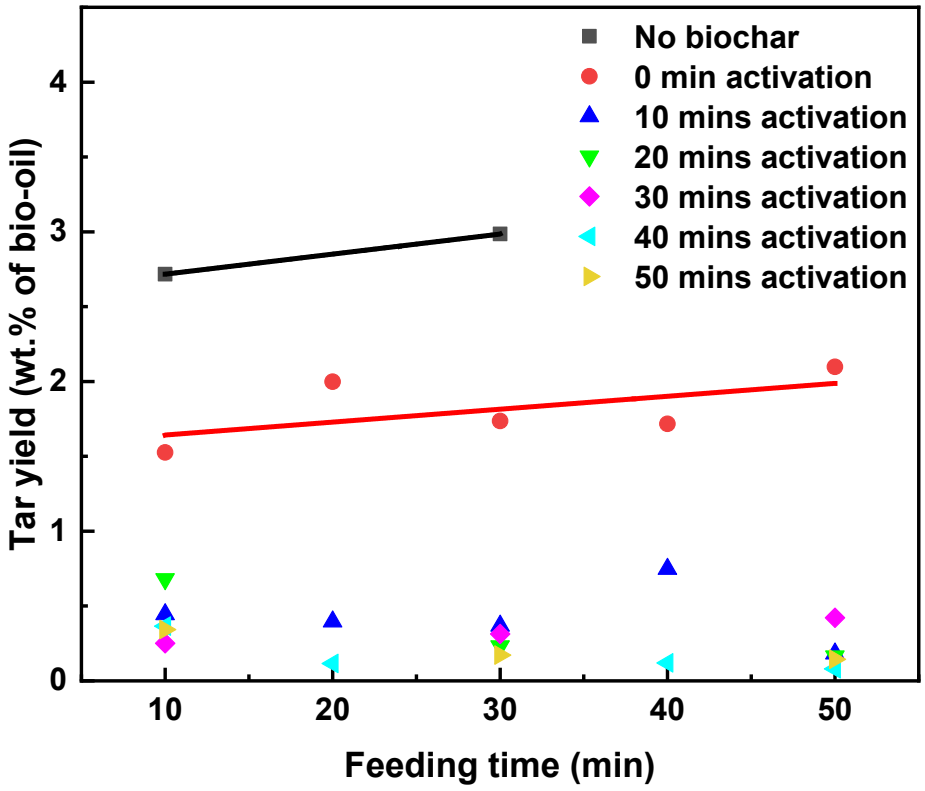

Figure 5. 2. Tar yields after steam reforming with and without using raw/activated biochar as a catalyst.

Figure 5. *2* shows the tar yields after steam reforming with or without using biochar as a catalyst at 800 °C as a function of the feeding time of bio-oil, which is the same time for tar reforming. It should be pointed out that the tar yields after reforming with the activated biochars were very low, so clear trendlines of these tar yields were not discernable and thus were not shown in the figure. After the same reforming time, the tar yields from the catalytic steam reforming with biochar were significantly lower than that from steam reforming without biochar. The results demonstrate the high catalytic activity of biochar in tar destruction, which is in agreement with the literature [13,17,33]. Additionally, the tar yield after steam reforming using activated biochar as a catalyst is nearly half of that when using

raw biochar. The activated biochar samples are clearly more effective in tar reforming than the raw biochar. The results indicate that the activation of biochar by H_2O can enhance its catalytic activity and then promote the steam reforming of tar over biochar.

Tar is a very complicated mixture which consists of hundreds of components containing benzene, naphthalene, heterocyclic compounds, phenols and polycyclic aromatic hydrocarbons (PAHs) with many O-containing functional groups [34]. The existence of aromatic structures in tar impacts the product gas quality during gasification and can be used to monitor the performance of biochar in the catalytic steam reforming of tar. UV-fluorescence spectroscopy was employed for identifying the features of aromatic structures in tar. *Figure* 5. *3* shows the UV-fluorescence spectra of tars from steam reforming without/with biochar for different times. The fluorescence intensity of *Figure* 5. *3*(a), 3(b) and 3(c) is expressed on a same tar concentration (4ppm) basis for comparison. For the same reforming time, the tar processed with biochar catalysts had lower fluorescence intensity than that processed without biochar. The fluorescence intensities from tar reformed with the activated biochar also dropped compared with those reformed with the raw biochar. Besides, a further decrease in the fluorescence intensity was observed when the biochars activated for long time (40-50 mins) were employed. These results indicate that the tar became less aromatic when utilising increasingly activated biochar. More specifically, the activated biochar preferentially enhanced the destruction of the aromatic ring systems in tar.

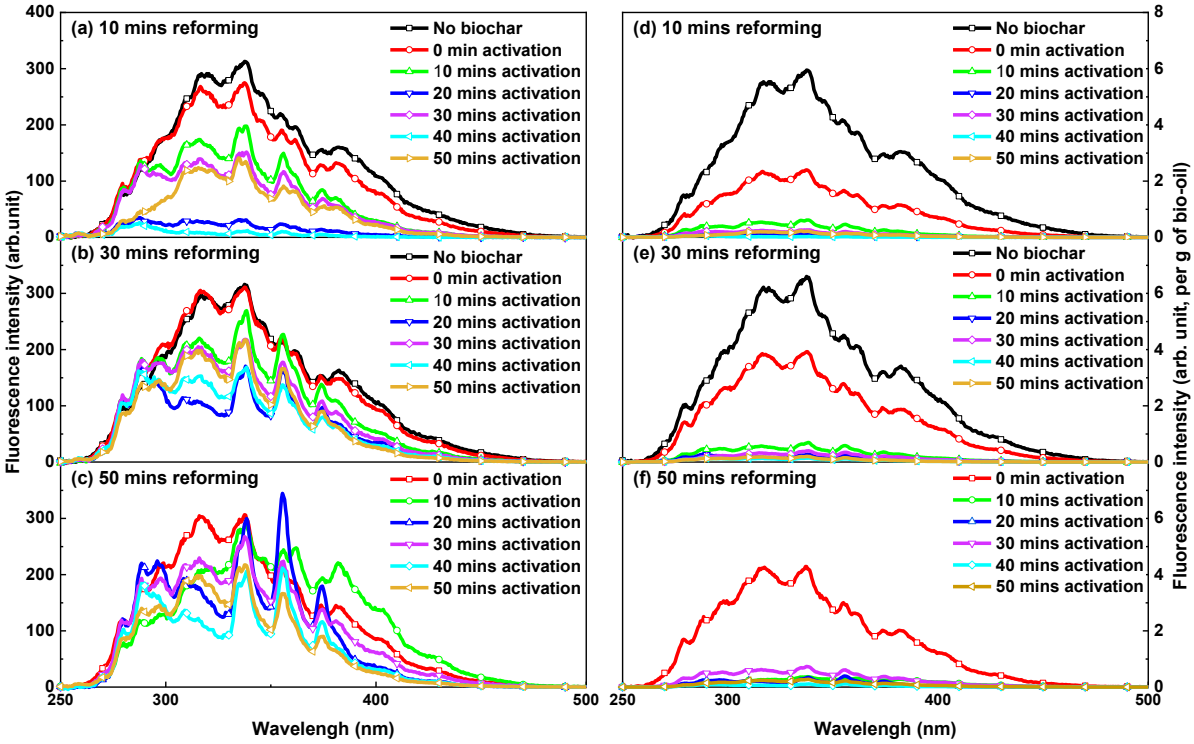

Figure 5. 3. Constant energy (-2800 cm^{-1}) synchronous spectra of tars after steam reforming with/without biochar for the same time. (a) and (d) 10 mins reforming; (b) and (e) 30 mins reforming; (c) and (f) 50 mins reforming. The fluorescence intensity in (a), (b) and (c) is expressed on a same tar concentration (4ppm) basis. The fluorescence intensity in (d), (e) and (f) is displayed on a per gram of bio-oil basis.

An alternative way of comparison of the catalytic effects of various biochars on the destruction of aromatic ring systems in tar can be obtained from *Figure* 5. *3*d-f, in which the fluorescence intensity is displayed on a per gram of bio-oil basis. The intensities in *Figure 5. 3*d-f can semi-quantitatively indicates the "yields" of the aromatic ring systems in tars from per unit mass of bio-oil used in the experiments, therefore giving a better comparison of the relative amount of aromatic ring systems left in different tars after reforming experiments. From *Figure* 5. *3*d-f, for a certain amount of bio-oil used in the experiments, the "yields" of aromatic structures dropped significantly when biochar was employed as a catalyst. In addition, as was expected, the activated biochar resulted in much lower "yields" than the raw biochar. The data imply that the breakdown of the aromatic structures in tar during the steam reforming with the activated biochar was more significant than that with the raw biochar,

which was in turn more significant than that without biochar. The effectiveness of biochar in tar removal conversion was significantly enhanced by the steam activation of biochar.

The “yields” of the aromatic structures in tar reflect the catalytic activity of biochar in tar reforming. Higher catalytic activity will lead to lower “yields” of aromatic structures in tar. Therefore, theese data from *Figure* 5. *3*d-f reveals that the activated biochars have higher catalytic activity in tar destruction than the raw biochar. The chemical structure of biochar has been considered to play a vital role in tar conversion [18]. Therefore, it is proposed that the treatment of biochar in H_2O must have changed its chemical structure, leading to increased catalytic activity in the steam reforming of tar.

It has been known that the structure of biochar changes drastically during tar reforming with the continuous tar destruction over biochar, as well as the gasification of biochar simultaneously in the presence of steam [3]. The structural changes of biochar may therefore alter the catalytic activity of biochar and then affect the destruction of tar [18]. To clearly show the relationship between biochar catalytic efficiency of biochar and the reforming time, the fluorescence intensities are plotted as a function of reforming time for different biochar activation periods in *Figure* 5. *4*. The intensity is displayed on a per gram of bio-oil basis. For the same biochar catalyst, the fluorescence intensity of tar increased as the reforming progressing, indicating increased “yields” of the aromatic ring systems in tars. Both the activated biochar and raw biochar show the same trend. The data demonstrate that the destruction of the aromatic structures in tars became less significant as the reforming progressed. The results indicate that the catalytic activity of biochar decreased as the reforming reactions progress, which could be caused by the changes in the structure of biochar [18]. For the purpose of better understanding the role of biochar structure in tar conversion, we investigated the changes in the chemical structure of biochar, which will be discussed in the following section.

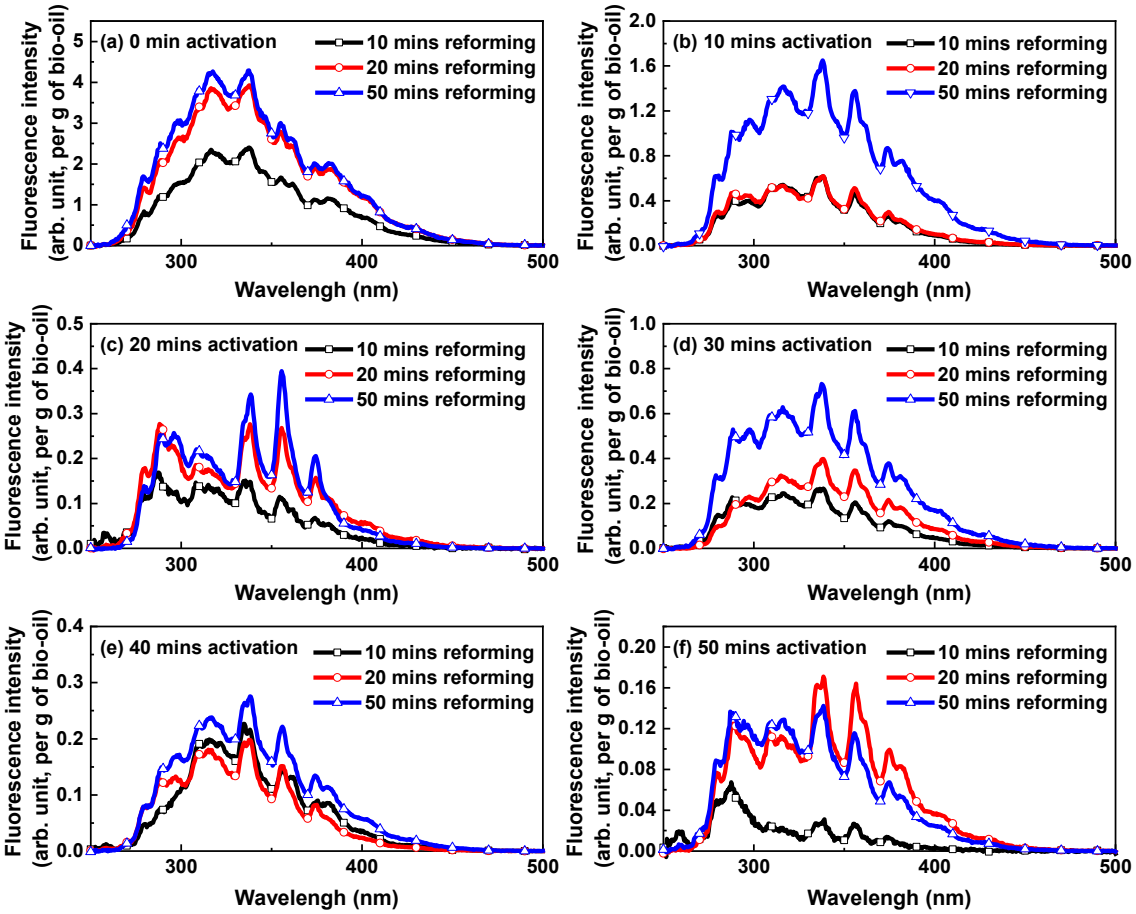

Figure 5. 4. Constant energy (−2800 cm^{-1}) synchronous spectra of tars after steam reforming with raw or activated biochar for different times. The fluorescence intensity is displayed on a per gram of bio-oil basis.

5.3.2 Changes in the chemical structure of biochar

5.3.2.1 Raman spectroscopic characterization of biochar

Figure 5. *5* shows the ratio $I_{(Gr+Vl+Vr)}/I_D$ between band peak areas and the total Raman peak area (800-1800 cm^{-1}) of biochar samples before and after being activated or used as a catalyst. The ratio of band peak areas $I_{(Gr+Vl+Vr)}/I_D$ of biochar represents changes of the carbon skeleton in biochar. The decrease of the ratio $I_{(Gr+Vl+Vr)}/I_D$ reflects a reduction of the relative quantity of the small aromatic ring systems and/or an relative growth of the amount of large aromatic ring systems in biochar [29]. All the data in *Figure* 5. *5*a roughly fall into the same trendline: the ratios $I_{(Gr+Vl+Vr)}/I_D$ for all the biochar samples decreased in a similar manner as the reactions progressed. Specifically, the biochar samples that went through tar reforming (0 min

activation) show a similar trend to the biochar samples that did not go through tar reforming (no bio-oil). The ratios $I_{(Gr+Vl+Vr)}/I_D$ declined in the first 30 mins and leveled off. In addition, both the activated biochar and raw biochar samples followed this trend. The ratios $I_{(Gr+Vl+Vr)}/I_D$ remained nearly at the same level and kept almost unchanged after tar reforming. These data indicate that the conversion of the aromatic ring systems in biochar broadly follows the same inherent change during tar reforming, which agrees well with our previous works [18,35]. That is to say, the chemical changes in the aromatic ring systems themselves in biochar were not closely linked to the destruction of tar.

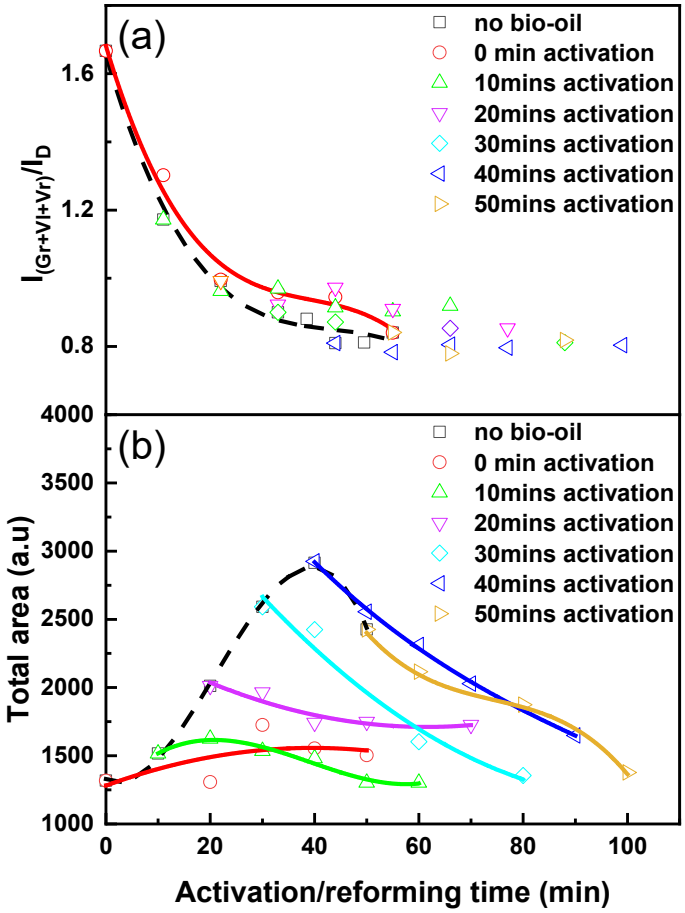

Figure 5. 5. Raman spectroscopic data. (a) ratio of band peak areas $I_{(Gr+Vl+Vr)}/I_D$ and (b) total Raman peak area (800 - 1800cm^{-1}) of biochar as a function of activation time (no-bio-oil) and/or reforming time (0 - 50 mins activation). The dashed line and solid line show the changes with the increase of activation and reforming time, respectively.

The total Raman peak areas of the biochars are shown in *Figure* 5. *5*b. The results show that the activated biochar has a higher content of O-containing functional groups (showing higher peak areas) than the raw biochar, indicating that the activation of biochar by H_2O increased the content of O-containing functional groups in biochar. Moreover, the amounts of O-containing functional groups in biochars without going through tar reforming (no bio-oil) were much higher than those in the biochars that went through tar reforming. Interestingly, after going through tar reforming, the content of O-containing functional groups in the activated biochar could drop down very significantly, in some cases even to almost the same level as that in the raw biochar. Thus, the O-containing functional groups in biochar were consumed after being employed as a catalyst for tar reforming.

The content of O-containing functional groups in activated biochar increased with the increasing time of activation, and lead to enhanced destruction of tar. As a result, lower tar yields (*Figure* 5. *2*), as well as lower fluorescence intensities (*Figure* 5. *3*) were achieved after using the activated biochar as a catalyst than the raw biochar. These spectroscopic results imply that the O-containing functional groups present in biochar can enhance the catalytic activity of biochar for tar reforming. Besides, the O-containing functional groups may serve as activated intermediates for tar conversion and they take part in the reactions [3]. During catalytic steam reforming, tar molecules may be adsorbed on the biochar surface through those active O-containing functional groups and can be decomposed over biochar by coking [8,36]. The tar compounds may interact with the active O-containing functional groups through H radicals, leading to the breakdown of tar compounds and the consumption of the active O-containing functional groups. Thus, the active O-containing functional groups are continuously consumed during tar reforming. As a result, the catalytic activity of biochar decreased, which caused the significantly lower rates of tar destruction with increasing reforming time. This conclusion explains the increasing average “yields” of the aromatic ring systems in tars with increasing reforming time as shown in *Figure* 5. *4*.

The peak area of UV-fluorescence spectra was further used to assess the catalytic activity of biochar [3,13]. The relationships between the total Raman peak area (or the ratio of band peak areas $I_{(Gr+Vl+Vr)}/I_D$) of biochar and the peak area of UV-fluorescence spectra from tar are shown in *Figure* 5. *6*. The peak areas of the UV-fluorescence spectra decrease with the increase of the total Raman area (*Figure* 5. *6*a), whilst the ratio of band peak areas $I_{(Gr+Vl+Vr)}/I_D$

is relatively constant as a function of the UV-fluorescence spectra peak area. The results further confirmed that the change of the aromatic ring systems (ratio of $I_{(Gr+Vl+Vr)}/I_D$) in biochar is not the key reason for the catalytic activities of biochar catalysts, while the O-containing functional groups (total Raman area) are the main reason for the increased catalytic activity of biochar. In conclusion, the activation of biochar by H_2O is an oxygenation process of biochar [32,37], where an increased content of O-containing functional groups enhances the catalytic activity of biochar, which then enhances tar destruction. Similarly, because the catalytic steam reforming of tar using biochar as a catalyst is a de-oxygenation process of biochar, the decrease of O-containing functional groups results in the subsequent lower catalytic activity of biochar. In summary, although the importance of O-containing functional groups in biochar for tar reforming has been inferred in previous studies [3,18,37], our results clearly demonstrated that the O-containing functional groups enhanced tar reforming and were consumed in the meantime.

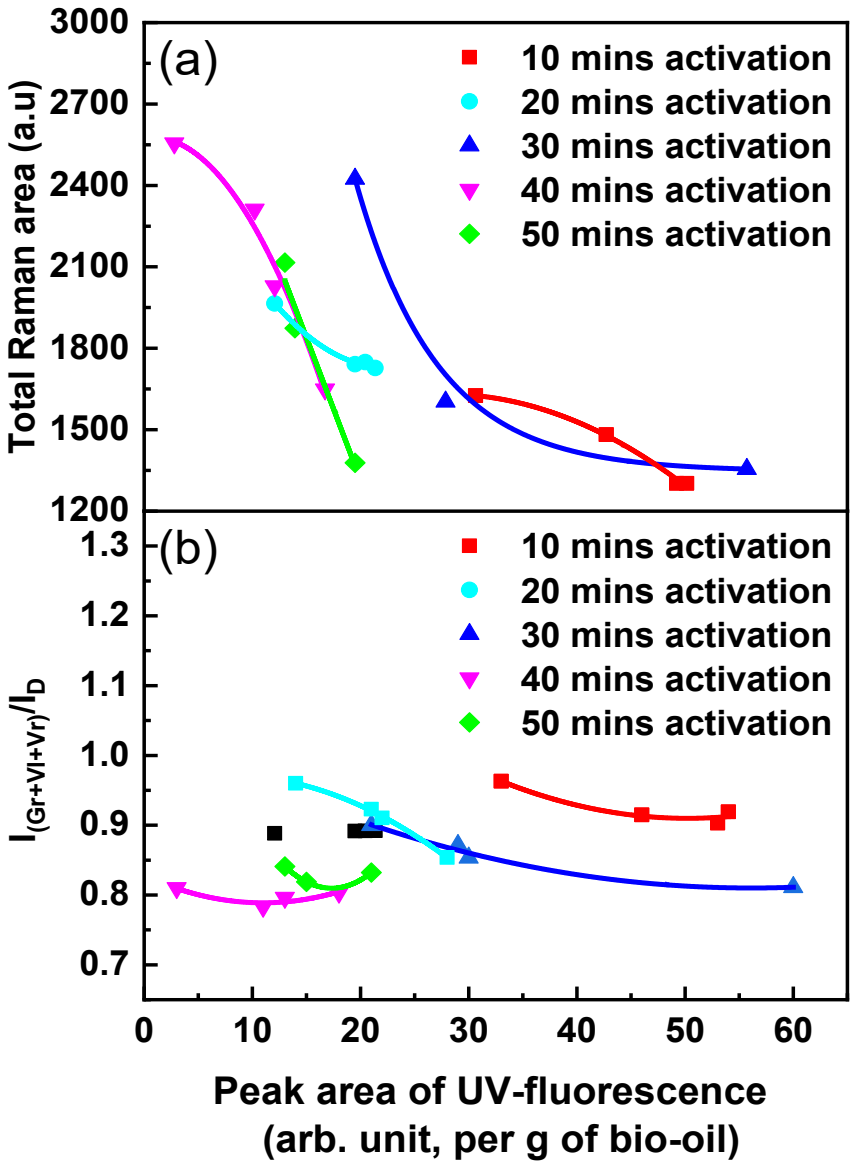

Figure 5. 6. (a) Total Raman peak area (800-1800 cm^{-1}) and (b) ratio of band peak areas $I_{(Gr+Vl+Vr)}/I_D$ of biochar as a function of the total peak area of constant energy (-2800 cm^{-1}) synchronous spectra of tar solutions (4 ppm).

5.3.2.2 XPS characterization of biochar

To further discover the specific types of O-containing functional groups in biochar that are primarily responsible for tar conversion, we used XPS to characterize the chemical structures of biochar. *Figure* 5. *7* shows the relative distribution of various O-containing species from the

high-resolution O 1s spectra of biochars. Overall, the relative content of aromatic C-O structures in the activated biochars increased after activation by H_2O, while the aromatic C=O structures reduced, see the data for 'no bio-oil' in *Figure* 5. *7* (the dashed black lines). These observations are in broad agreement with our previous study [38]. Furthermore, after acting as catalysts for tar reforming, the concentration of the aromatic C-O structures generally has a decreasing trend as tar reforming time increases, while an overall increase in the relative amount of C=O groups was observed. The trendline of the aromatic C-O structures (*Figure* 5. *7*a) was very similar to that of the O-containing functional groups obtained from Raman spectroscopy (*Figure* 5. *5*b).

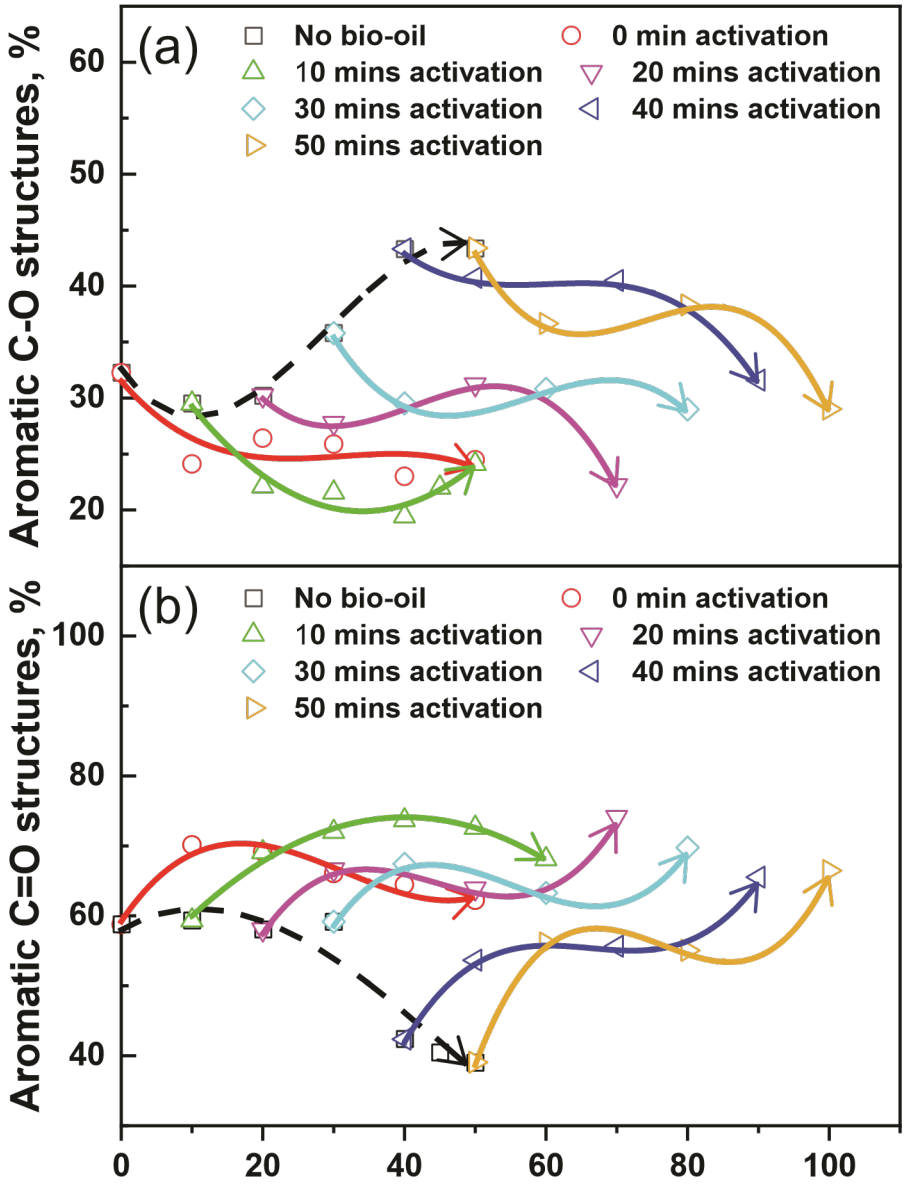

Figure 5. 7. Relative contents of (a) aromatic C-O structures and (b) aromatic C=O structures in O 1s spectra obtained by XPS analysis as a function of activation time (no bio-oil), reforming time (0 - 50 mins activation). The dashed line and solid line show the changes with the increase of activation and reforming time, respectively.

During the activation of biochar, the dominated breakage of aromatic ring systems leads to the formation of a significant amounts of O-containing functional groups especially the aromatic C-O groups, which contribute to the increases in the total Raman intensity (*Figure* 5. *5*b). The generated aromatic C-O groups give rise to the higher catalytic activities of the activated biochar than the raw biochar. As a result, the tar reforming was enhanced and a decreased tar yield (*Figure* 5. *2*) and UV-fluorescence intensity (*Figure* 5. *3*) were observed

after the catalytic steam reforming. Those aromatic C-O groups may be on (partially) broken aromatic ring systems, which are active sites for tar reforming. During tar reforming, the unstable aromatic ring systems with C-O groups react with tar molecules, to promote the destruction of tar and the production of gases including CO, H_2 and CO_2. The consumption of the C-O groups results in the reduction in the number of active sites for tar conversion, leading to the reduction in the catalytic activity of biochar. Therefore, an increasing trend for the fluorescence intensity with the increasing reforming time (*Figure* 5. *4*) was observed. As mentioned previously, the ash yield of biochar stayed almost unchanged after tar reforming, so it is believed that the aromatic C-O groups are a key reason for enhancing the catalytic activity of biochar. Meanwhile, in the presence of a considerable amount of H radicals, the C-O structure tends to convert to C=O structure and produce H_2. As a consequence of the consumption and conversion of C-O structure, an overall decrease of the C-O structure (*Figure* 5. *7*a) and an overall increase of the C=O structure (*Figure* 5. *7*b) were observed with the progress of reforming. There are a slight increase of the C-O structure and decrease of the C=O structures between 10 and 30 minutes of reforming. This is possibly because that the equilibrium between the C-O and C=O structures is also affected by other factors, which deserves further investigation. Our XPS results showed that the aromatic C-O groups are particularly important for enhancing the catalytic activity of biochar in tar reforming.

5.4 Conclusions

A series of experiments were carried out at 800 °C to understand the evolution and role of O-containing functional groups on the catalytic steam reforming of tar using biochar as a catalyst. Raw biochar and biochar activated by H_2O were employed as catalysts. The performance of different biochars as well as their chemical structures were investigated before and after treatment. Our results reveal that the activated biochar has better performance in tar reforming than the raw biochar. Moreover, the rate of tar reforming became slower as the reforming time increased. The activation of biochar by H_2O increased the content of the O-containing functional groups, in particular the aromatic C-O groups. During steam reforming of tar, the relative content of aromatic C-O groups decreased while the aromatic C=O groups slightly increased. It is believed that the O-containing functional groups, especially the

aromatic C-O groups, are the key to enhancing the catalytic activity of biochar for tar reforming. Moreover, the aromatic C-O groups may act as active intermediates that take part in the reforming reactions with tar.

5.5 References

[1] Li C-Z. Importance of volatile-char interactions during the pyrolysis and gasification of low-rank fuels - A review. Fuel 2013;112:609–23.

[2] Li C, Suzuki K. Tar property, analysis, reforming mechanism and model for biomass gasification-An overview. Renew Sustain Energy Rev 2009;13:594–604.

[3] Song Y, Wang Y, Hu X, Xiang J, Hu S, Mourant D, Li T, Wu L, Li C-Z. Effects of volatile-char interactions on in-situ destruction of nascent tar during the pyrolysis and gasification of biomass. Part II. Roles of steam. Fuel 2015;143:555–62.

[4] Paethanom A, Nakahara S, Kobayashi M, Prawisudha P, Yoshikawa K. Performance of tar removal by absorption and adsorption for biomass gasification. Fuel Process Technol 2012;104:144–54.

[5] Phuphuakrat T, Namioka T, Yoshikawa K. Tar removal from biomass pyrolysis gas in two-step function of decomposition and adsorption. Appl Energy 2010;87:2203–11.

[6] Tao K, Ohta N, Liu G, Yoneyama Y, Wang T, Tsubaki N. Plasma enhanced catalytic reforming of biomass tar model compound to syngas. Fuel 2013;104:53–7.

[7] Wang Y, Hu X, Song Y, Min Z, Mourant D, Li T, Gunawan R, Li C-Z. Catalytic steam reforming of cellulose-derived compounds using a char-supported iron catalyst. Fuel Process Technol 2013;116:234–40.

[8] Min Z, Asadullah M, Yimsiri P, Zhang S, Wu H, Li C-Z. Catalytic reforming of tar during gasification. Part I. Steam reforming of biomass tar using ilmenite as a catalyst. Fuel 2011;90:1847–54.

[9] Min Z, Zhang S, Yimsiri P, Wang Y, Asadullah M, Li C-Z. Catalytic reforming of tar during gasification. Part IV. Changes in the structure of char in the char-supported iron catalyst during reforming. Fuel 2013;106:858–63.

[10] Li C, Hirabayashi D, Suzuki K. Steam reforming of biomass tar producing H_2-rich gases over Ni/MgO_x/CaO_{1-x} catalyst. Bioresour Technol 2010;101.

[11] Cao JP, Shi P, Zhao XY, Wei XY, Takarada T. Catalytic reforming of volatiles and nitrogen compounds from sewage sludge pyrolysis to clean hydrogen and synthetic gas over a nickel catalyst. Fuel Process Technol 2014;123:34–40.

[12] Guan G, Kaewpanha M, Hao X, Abudula A. Catalytic steam reforming of biomass tar: Prospects and challenges. Renew Sustain Energy Rev 2016;58:450–61.

[13] Min Z, Yimsiri P, Asadullah M, Zhang S, Li C-Z. Catalytic reforming of tar during gasification. Part II. Char as a catalyst or as a catalyst support for tar reforming. Fuel 2011;90:2545–52.

[14] Abu El-Rub Z, Bramer E a. a., Brem G. Review of Catalysts for Tar Elimination in Biomass Gasification Processes. Ind Eng Chem Res 2004;43:6911–9.

[15] Chang G, Xie J, Huang Y, Liu H, Yin X, Wu C. Gasification Reactivity and Pore Structure Development: Effect of Intermittent Addition of Steam on Increasing Reactivity of PKS Biochar with CO_2. Energy and Fuels 2017;31:2887–95.

[16] Román Galdámez J, García L, Bilbao R. Hydrogen production by steam reforming of bio-oil using coprecipitated Ni-Al catalysts. Acetic acid as a model compound. Energy and Fuels 2005;19:1133–42.

[17] Song Y, Zhao Y, Hu X, Zhang L, Sun S, Li C-Z. Destruction of tar during volatile-char interactions at low temperature. Fuel Process Technol 2018;171:215–22.

[18] Song Y, Wang Y, Hu X, Hu S, Xiang J, Zhang L, Zhang S, Min Z, Li C-Z. Effects of volatile-char interactions on in situ destruction of nascent tar during the pyrolysis and gasification of biomass. Part I. Roles of nascent char. Fuel 2014;122:60–6.

[19] Zhang S, Song Y, Song YC, Yi Q, Dong L, Li TT, Zhang L, Feng J, Li WY, Li C-Z. An advanced biomass gasification technology with integrated catalytic hot gas cleaning. Part III: Effects of inorganic species in char on the reforming of tars from wood and agricultural wastes. Fuel 2016;183:177–84.

[20] Li X, Hayashi J, Li C-Z. FT-Raman spectroscopic study of the evolution of char structure during the pyrolysis of a Victorian brown coal. Fuel 2006;85:1700–7.

[21] Advanced biomass gasification technology, Australian Renewable Energy Agency. https://arena.gov.au/projects/advanced-biomass-gasification-technology/. (accessed January 29, 2019).

[22] Grinding pyrolysis, Renergi Pty Ltd. http://www.renergi.net/grinding_pyrolysis. (accessed January 29, 2019).

[23] Wu H, Quyn DM, Li C-Z. Volatilisation and catalytic effects of alkali and alkaline earth metallic species during the pyrolysis and gasification of Victorian brown coal. Part III. The importance of the interactions between volatiles and char at high temperature. Fuel 2002;81:1033–9.

[24] Min Z, Yimsiri P, Zhang S, Wang Y, Asadullah M, Li C-Z. Catalytic reforming of tar during gasification. Part III. Effects of feedstock on tar reforming using ilmenite as a catalyst. Fuel 2013;103:950–5.

[25] Jiang S, Hu X, Xia D, Li C-Z. Formation of aromatic ring structures during the thermal treatment of mallee wood cylinders at low temperature. Appl Energy 2016;183:542–51.

[26] Sathe C, Pang Y, Li C-Z. Effects of heating rate and ion-exchangeable cations on the pyrolysis yields from a Victorian brown coal. Energy and Fuels 1999;13:748–55.

[27] Li C-Z, Sathe C, Kershaw JR, Pang Y. Fates and roles of alkali and alkaline earth metals during the pyrolysis of a Victorian brown coal. Fuel 2000;79:427–38.

[28] Li CZ, Wu F, Cai HY, Kandiyoti R. UV-Fluorescence Spectroscopy of Coal Pyrolysis Tars. Energy and Fuels 1994;8:1039–48.

[29] Li X, Hayashi J ichiro, Li C-Z. Volatilisation and catalytic effects of alkali and alkaline earth metallic species during the pyrolysis and gasification of Victorian brown coal. Part VII. Raman spectroscopic study on the changes in char structure during the catalytic gasification in air. Fuel 2006;85:1509–17.

[30] Tay HL, Kajitani S, Zhang S, Li C-Z. Effects of gasifying agent on the evolution of char structure during the gasification of Victorian brown coal. Fuel 2013;103:22–8.

[31] Tay HL, Kajitani S, Zhang S, Li C-Z. Inhibiting and other effects of hydrogen during gasification: Further insights from FT-Raman spectroscopy. Fuel 2014;116:1–6.

[32] Wang S, Wu L, Hu X, Zhang L, O'Donnell KM, Buckley CE, Li C-Z. An X-ray photoelectron spectroscopic perspective for the evolution of O-containing structures in char during gasification. Fuel Process Technol 2018;172:209–15.

[33] Shen Y. Chars as carbonaceous adsorbents/catalysts for tar elimination during biomass pyrolysis or gasification. Renew Sustain Energy Rev 2015;43:281–95.

[34] Milne TA, Evans RJ, Abatzaglou N. Biomass Gasifier "Tars": Their Nature, Formation, and Conversion. Technical Report (NREL/TP-570-25357). National Energy Laboratory. United states. 1998.

[35] Zhang S, Min Z, Tay H-L, Asadullah M, Li C-Z. Effects of volatile–char interactions on the evolution of char structure during the gasification of Victorian brown coal in steam. Fuel 2011;90:1529–35.

[36] Hosokai S, Kumabe K, Ohshita M, Norinaga K, Li C-Z, Hayashi J-I. Mechanism of decomposition of aromatics over charcoal and necessary condition for maintaining its activity. Fuel 2008;87:2914–22.

[37] Feng D, Zhao Y, Zhang Y, Gao J, Sun S. Changes of biochar physiochemical structures during tar H_2O and CO_2 heterogeneous reforming with biochar. Fuel Process Technol 2017;165:72–9.

[38] Wang S. Evolution of Char Structure and Reactivity during Gasification (thesis). Curtin University, 2016.

Chapter 6

Difference in tar reforming activities between biochar catalysts activated in H_2O and CO_2

Y. Liu, M. Paskevicius, H. Wang, C. Fushimi, G. Parkinson, C.-Z. Li, Difference in tar reforming activities between biochar catalysts activated in H_2O and CO_2, Fuel, 271 (2020) 117636. https://doi.org/10.1016/j.fuel.2020.117636.

Abstract

This study investigates the difference in the activities between biochar catalysts activated in H_2O and CO_2 for *in situ* tar reforming. The experiments were performed in a two-stage fluidized-bed/fixed-bed at 800 °C. Mallee wood biochar (106 - 250 µm) was activated in pure CO_2 or 15 vol. % H_2O balanced with Ar (15 vol. %H_2O/Ar) for different times (0 – 50 mins) before being used as a catalyst for tar reforming. Based on the analysis of tar samples, it was found that H_2O-activated biochar showed higher catalytic activity than CO_2-activated biochar in both steam reforming and dry reforming of tar. Moreover, under otherwise identical conditions, reforming in steam was always more rapid than that in CO_2 regardless of the atmosphere in which biochar was activated. The characterisation of biochar showed that H_2O activation resulted in a biochar with a higher content of O-containing functional groups and aromatic C-O structures than that from CO_2 activation. In addition, the content of O-containing functional groups and aromatic C-O structures of biochar after the steam reforming were higher than those after the dry reforming of tar. The different catalytic activities between the biochars activated by H_2O and CO_2 could be attributed to the different amounts of O-containing functional groups and aromatic C-O structures in biochar generated by H_2O or CO_2 activation. An extra supply of H_2O plays an important role in improving and maintaining the catalytic activity of biochar during tar reforming.

6.1 Introduction

Growing attention has been focussed on renewable bioenergy to combat the concerns over global warming. Biomass, as an abundant and carbon-neutral resource, is believed to be an important constituent of the global energy system. One of the most promising technologies to utilise biomass is gasification by converting biomass into syngas that can be further used for the generation of base-load electricity and the production of hydrogen (H_2), liquid fuels and chemicals [1–3]. The removal of tar from a raw syngas is one of the biggest challenges for developing and commercialising advanced gasification technologies [2,4,5].

Many methods have been developed for removing tar from syngas. Catalytic tar reforming is an efficient and technically feasible route [6–8]. Biochar, a carbon-rich product

from biomass pyrolysis or gasification, has been considered to be a cost-effective catalyst for tar reforming [9–11]. The catalytic activity of biochar for tar reforming is closely related to its physicochemical properties, which are, for example, reflected by its porous morphology (high surface area and pore volume distribution) [12,13], O-containing functional groups [11,14] and inherent alkali and alkaline earth metallic (AAEM) species [15]. However, it remains unclear whether there are any interactions between those properties, leading to questions surrounding which property is the ultimate one for improving the catalytic activity of biochar. In other words, it remains unclear what are the fundamental structural properties of a biochar that ultimately govern(s) its reactivity for the reforming of tar.

In particular, our previous study [14] has revealed the significance of O-containing functional groups in biochar on its catalytic activities for tar reforming. The ways by which oxygen is introduced into the biochar, which may in turn influence the exact chemical structure of O-containing functional groups, may be an important factor influencing the biochar catalytic activity. The structural properties of biochar may be strongly affected by the gasification conditions. H_2O and CO_2 are the two most commonly used gasifying agents and they generate biochar with different properties, e.g. in terms of porosity [16] and/or oxygen complexes [17,18]. A number of studies [10,11,19,20] have shown that the biochar produced/activated in H_2O is very effective in tar removal, but little is known about the catalytic performance of CO_2-activated biochar for tar reforming. A full understanding of the mechanism of tar reforming employing biochar as a catalyst requires further study of the correlation between the structural characteristics of activated biochar and its catalytic activity. This understanding would help to optimise the conditions to produce biochar catalysts for tar reforming in commercial gasifiers. This study is part of our ongoing efforts to develop a biochar-based hot gas cleaning system for biomass gasification.

Therefore, the aim of this study was to investigate the catalytic activity of CO_2-activated biochar for tar reforming, followed by differentiating between CO_2 and H_2O activation of biochar with respect to their effects on the catalytic activity of biochar in tar reforming. The study provides useful information about some key biochar structural features for understanding the reforming mechanism of tar employing biochar as a catalyst, which in turn would help to optimize the design and operation of a gasifier.

6.2 Experimental

6.2.1 In situ tar reforming employing H_2O and CO_2-activated biochar as a catalyst

The biochar (106-250 μm) used in this study was prepared from the pyrolysis and gasification (5-10 mins) of Mallee biomass at 750-850 °C in Renergi's gasification demonstration plant [21,22]. The bio-oil sample was prepared from Mallee biomass using the Renergi's grinding pyrolysis demonstration plant [22]. The reforming experiments [14] were carried out in a three-frit two-stage fluidized-bed/fixed-bed quartz reactor [23,24], as is shown in *Figure* 6. *1*.

The biochar was placed on the middle frit prior to being heated in argon. After the reactor had stabilized at 800 °C, CO_2 or 15 vol% steam in argon was flowed into the reactor from the bottom at a total flow rate of 2.0 L min^{-1} to activate the biochar for different times (10-50 mins). After the activation was finished, CO_2 or 15 vol% steam was switched to the reforming agent, which may be CO_2 or 15 vol % H_2O in argon, while the feeding of bio-oil at 0.20 mL min^{-1} into the reactor with a high performance liquid chromatography (HPLC) pump also commenced simultaneously to begin the dry reforming or steam reforming of tar. Volatiles including tar were generated immediately after bio-oil reached the reaction zone at 800 °C. In other words, the tar for reforming, the focus of this study, was generated *in situ* from the reactions of bio-oil. It should be noted that, based on the relationships between biochar conversion and activation time that had been experimentally determined separately, the amount of biochar left after activation was controlled to be 1 g [14].

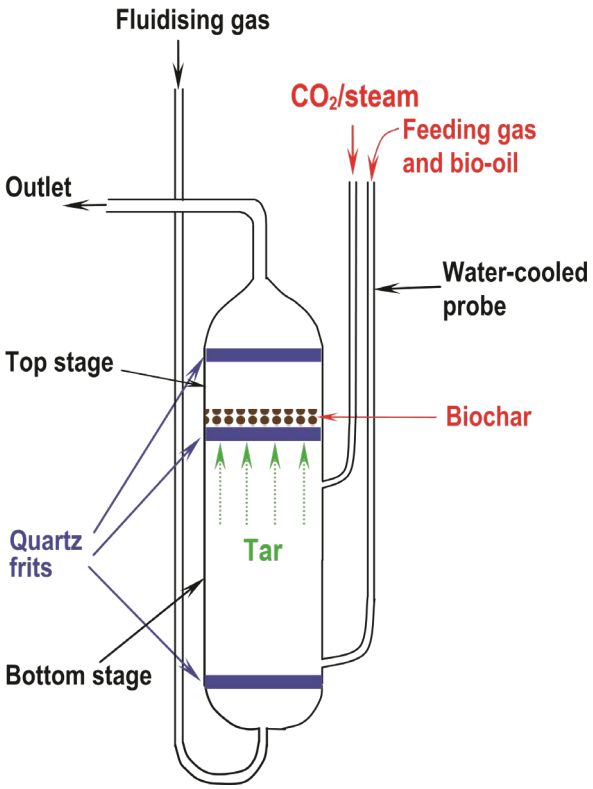

Figure 6. 1. A schematic diagram of the three-frit fluidized-bed/fixed-bed quartz reactor (modified from Ref. [23] with permission from Elsevier).

During reforming, the reactor outlet was connected to a series of three condensation traps to collect the condensable compounds from the outlet stream. These traps were filled with a mixture of HPLC-grade chloroform and methanol (4:1 by vol) [7,25]. When the required reforming time has elapsed, the feeding of bio-oil was stopped and the flow of reforming agent was switched to argon. The reactor was then lifted out of the furnace and cooled down under argon flow. The biochar and tar solutions were then collected for further analysis.

Moreover, a series of four experiments was also performed in order to investigate the different catalytic activities of biochar catalysts activated by H_2O or CO_2 for steam or dry reforming of tar. The experimental details are shown in *Table 6. 1*.

Table 6. 1. Experimental details for steam or dry reforming of tar using biochar catalysts activated in H_2O or CO_2.

Experiment	Conditions of tar reforming at 800 °C
CO_2 - H_2O R	Biochar was activated in CO_2 for 30 mins followed by 30 mins of tar reforming in 15 vol. % H_2O mixed with Ar.
CO_2 - CO_2 R	Biochar was activated in CO_2 for 30 mins followed by 30 mins of tar reforming in pure CO_2.
H_2O - H_2O R	Biochar was activated in 15 vol. % H_2O mixed with Ar for 30 mins followed by 30 mins tar reforming in 15 vol. % H_2O mixed with Ar.
H_2O - CO_2 R	Biochar was activated by 15 vol. % H_2O mixed with Ar for 30 mins followed by 30 mins tar reforming in pure CO_2.

Note: R means reforming

6.2.2 Tar analysis

The yield of tar was determined by dividing the amount of tar collected by the quantity of bio-oil fed into the reactor, according to the method used in our previous studies [7,26]. UV-fluorescence spectroscopy was employed to characterise the aromatic ring systems in tar solutions. A detailed description of the instrument and measurement can be found in our previous studies [7,14,27]. The fluorescence intensities are presented and compared on the basis of ‘‘per gram of bio-oil’’ [27,28]. Some of the tar yields and UV-fluorescence intensities of tar samples after steam reforming with H_2O activated biochars were reported previously [14] and used in this study for comparison purpose.

6.2.3 Biochar characterisation

The chemical structure of biochar was analysed by employing a Perkin–Elmer Spectrum GX FT-IR/Raman spectrometer and a Kratos AXIS Ultra DLD X-ray photoelectric spectra (XPS) spectrometer, following the procedures given in our previous work [14]. Briefly, each Raman spectrum (800–1800 cm^{-1}) was deconvoluted to understand the structural evolution of carbon matrix by looking at the ratios of areas of various Raman bands as well as the total O-containing functional groups (total Raman peak area) in biochar [14,29]. The XPS O 1s spectra were curve-fitted to obtain the relative contents of various O-containing functional groups following the methods described previously [18]

6.3 Results and discussion

6.3.1 Steam tar reforming employing CO_2 activated biochar as a catalyst

Figure 6. *2* shows the UV-fluorescence spectra of tars after steam reforming with non-activated (no CO_2) or biochar activated in CO_2 for different times (10-50 mins). The fluorescence intensity is expressed on a "per gram of bio-oil" basis and can semi-quantitatively reflect the relative "yields" of aromatic ring systems in tar from steam reforming. For the same reforming times (30 mins in *Figure 6. 2*a and 50 mins in *Figure 6. 2*b), the "yields" of aromatic ring systems in tar from the reforming with CO_2-activated biochars were much lower than those after reforming with the non-activated biochar. The data indicate that more aromatic ring systems in tar were reformed/removed after employing CO_2-activated biochar as a catalyst, which further implies that the CO_2 activation of biochar enhanced the catalytic activity of biochar for the reforming of the aromatic ring systems in tar. The reason for this enhancement can be that CO_2 activation changes the physicochemical properties of biochar, giving rise to its catalytic activity for the reforming of tar, as will be discussed later.

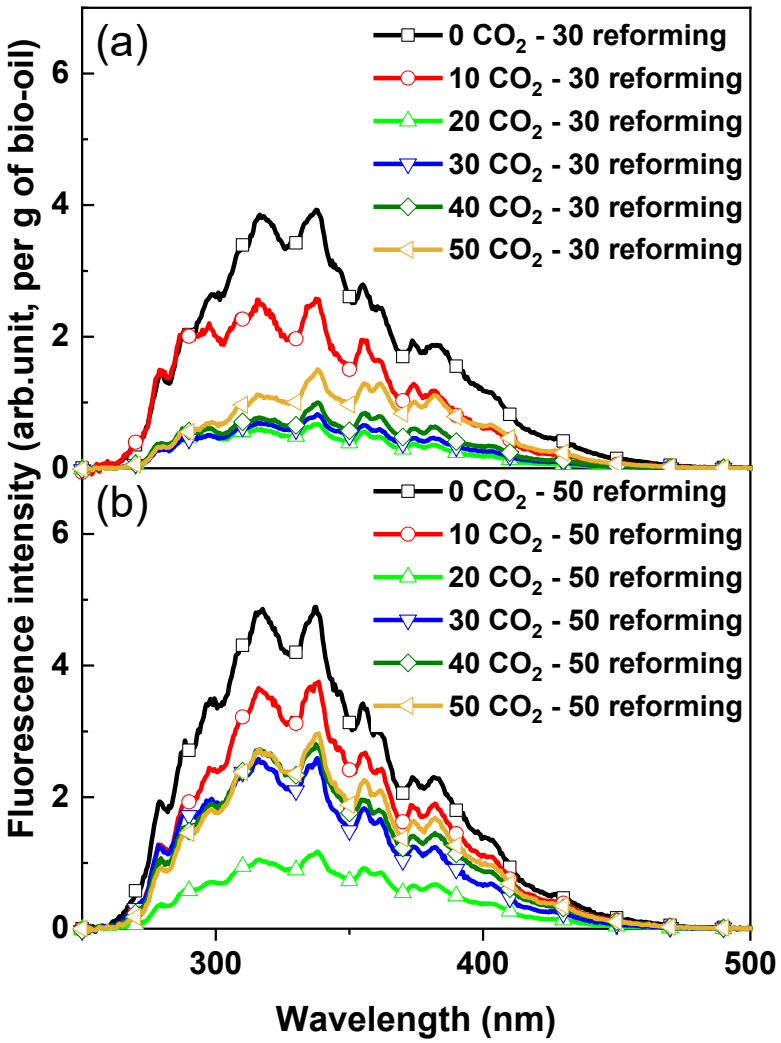

Figure 6. 2. Constant energy (−2800 cm^{-1}) synchronous spectra of tars after steam reforming for (a) 30 mins (shown as "30 reforming") and (b) 50 mins ("50 reforming") with the non-activated biochar ("0 CO_2") or biochars that had been activated in CO_2 for different times (e.g. "10 CO_2" represents 10 mins activation in CO_2). The fluorescence intensity is displayed on the "per gram of bio-oil" basis.

Figure 6. *3* displays the changes in fluorescence intensity with reforming time for the biochar with the same activation time in CO_2. As expected, for the same biochar activation time in CO_2, the fluorescence intensities of tar after 50 mins of reforming (i.e. after feeding bio-oil for 50 min) were higher than those after 30 mins of reforming. The trend is the same as that in our previous study using H_2O-activated biochar as a catalyst [14]. The data suggest

that the catalytic activity of biochar reduced with the progression of reforming time. The decreases in the catalytic activity of biochar could be due to the structural changes as well as the mass loss of biochar due to the steam gasification of biochar [11,14,30,31], as discussed later.

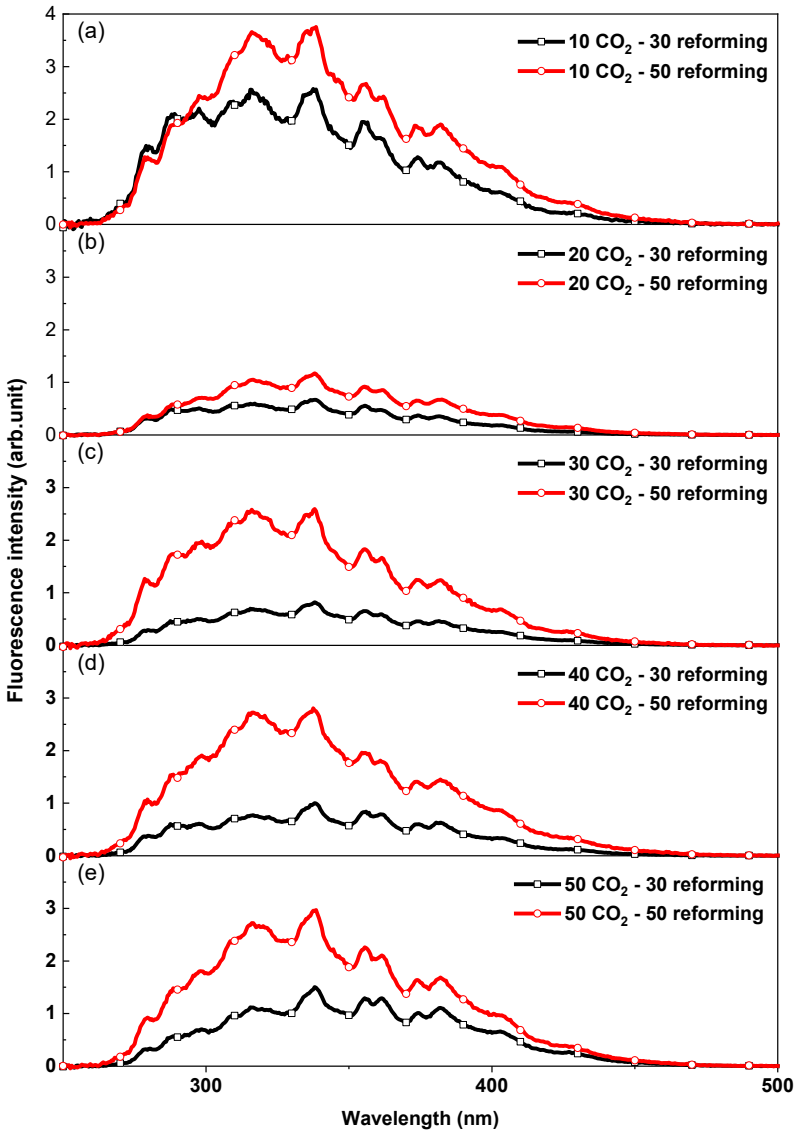

Figure 6. 3. Constant energy (−2800 cm^{-1}) synchronous spectra of tars from steam reforming with CO_2-activated biochars. The fluorescence intensity is displayed on a "per gram of bio-oil" basis.

6.3.2. Evolution of the chemical structure of CO_2-activated biochar

Figure 6. *4* shows the Raman spectroscopic data of biochar: (a) the ratio of band areas $I_{(Gr+Vl+Vr)}/I_D$ and (b) the total Raman peak area (800–1800 cm^{-1}). The band area ratio $I_{(Gr+Vl+Vr)}/I_D$ and total Raman area, represent, respectively, the relative ratio of small (containing 3-5 aromatic rings) to large aromatic ring systems (containing 6 or more rings) and the relative content of the O-containing functional group in biochar [32]. The ratio $I_{(Gr+Vl+Vr)}/I_D$ of biochar tar reforming with steam remained almost unchanged. This result was expected and indicates that the conversion of small aromatic ring systems to large ones in biochar was not closely related to tar reforming and, more specifically, the catalytic activity of biochar. These data are in line with our previous works [11,14,29,33]. In contrast, the total Raman area showed increases with increasing activation time (dash line) and subsequent decreases as *in situ* steam reforming progressed (solid line) in *Figure 6. 4*(b). The trends of the total Raman peak area were similar to that observed in our previous study [14], in which H_2O-activated biochars were used as catalysts for tar reforming. CO_2 activation added extra content of O-containing functional groups in biochar. After reforming with tar, the content decreased. The results have further confirmed our previous finding [14] that the content of O-containing functional groups in biochar is directly linked to its catalytic activity for tar removal. Here, the catalytic activity of biochar was enhanced by the increase in the content of O-containing functional groups caused by CO_2 activation. As a result, lower UV-fluorescence intensities from tar (*Figure* 6. *2*) were observed when the activation time of biochar increased within the range investigated. Likewise, the reduced O-containing functional groups in the process of reforming also leaded to the reduced catalytic activity of biochar, causing a rise of fluorescence intensity from aromatic species (per gram of bio-oil) with extended reforming time (*Figure 6. 3*).

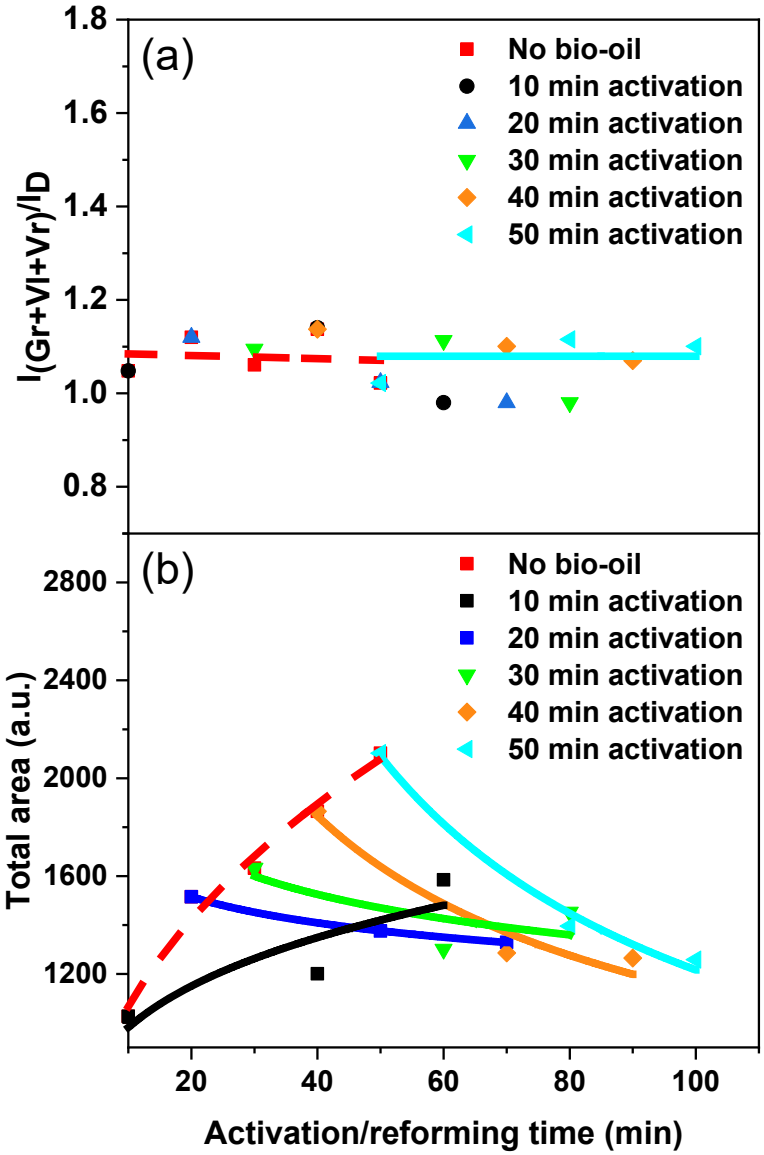

Figure 6. 4. Raman spectroscopic data. (a) the ratio of band areas $I_{(Gr+Vl+Vr)}/I_D$ and (b) the total Raman peak area (800 – 1800 cm^{-1}) of biochar changes with increasing activation time in CO_2 (dashed line) or reforming time in steam (solid line).

6.3.4 Different catalytic activities between CO_2 and H_2O activated biochar for tar reforming

The above observations have demonstrated that CO_2 activation, similar to H_2O activation, can also lead to the enhancement of catalytic activity of biochar for steam tar reforming by increasing the content of O-containing functional groups in biochar. It has also been known that H_2O activation and CO_2 activation can lead to different structural features of biochar [17]. It is reasonable to assume that the catalytic activities of CO_2-activated biochars are different

from that of biochars activated by H_2O for the same time. Therefore, we compared with our previous work [14] to assess the catalytic activities of biochars activated by H_2O or CO_2.

6.3.4.1 Different catalytic activities between H_2O- and CO_2-activated biochars for the reforming of tar in steam

Figure 6. 5 and *Figure 6. 6* show the tar yields and UV-fluorescence intensities from steam reforming employing H_2O- or CO_2-activated biochars as catalysts. After the same reforming time in steam, the tar yields (*Figure* 6. *5*) after reforming with H_2O-activated biochar were much lower than those with the biochar activated by CO_2 for the same activation time. The difference was greater when the reforming time extended from 30 to 50 mins. Clearly, the deactivation of CO_2-activated biochar was faster than that of H_2O-activated biochar during the reforming of tar in steam. Similarly, the UV-fluorescence intensities (*Figure* 6. *6*) after steam reforming using H_2O-activated biochar catalysts were much lower than those after reforming with CO_2-activated biochar. These results show that, after activation for the same time, the CO_2-activated biochar showed lower catalytic activity than the biochar activated by H_2O. The different catalytic activities between CO_2-activated and H_2O-activated biochar could be attributed to the different contents of O-containing functional groups in biochar resulting from CO_2 and H_2O activation, as will be discussed later.

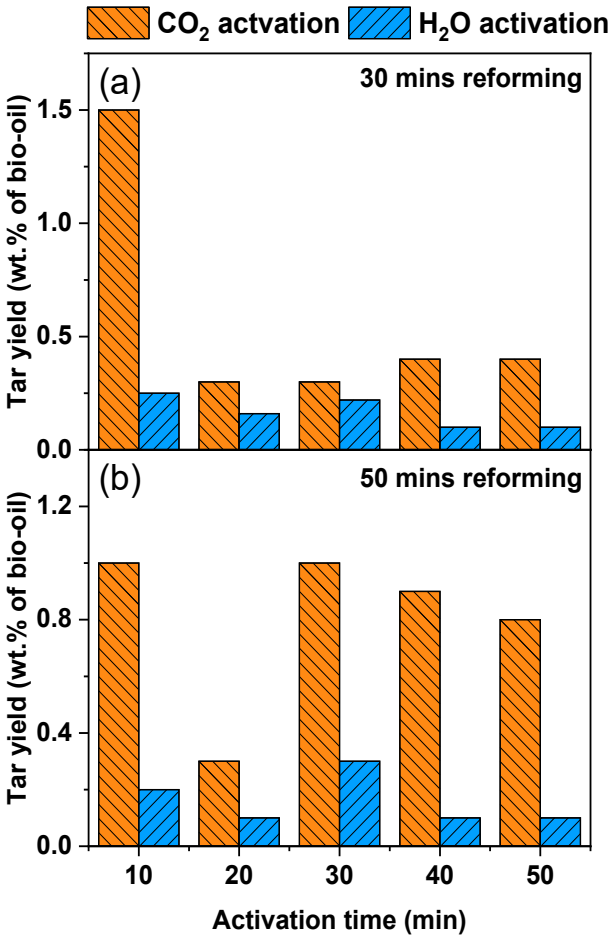

Figure 6. 5**.** Tar yields after the reforming of tar in steam for (a) 30 mins and (b) 50 mins with biochars activated by CO_2 or H_2O for 10-50 mins. The data for biochars activated in steam were published before [14] and are used here for comparison.

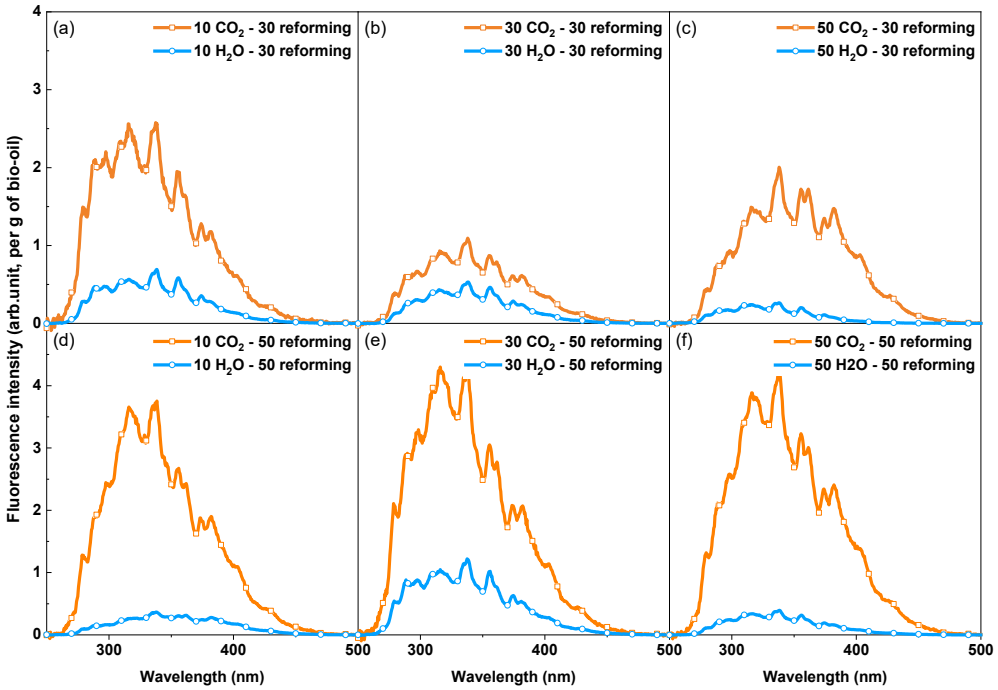

Figure 6. 6. Constant energy (−2800 cm^{-1}) synchronous spectra of tar samples after steam reforming for (a)–(c) 30 mins and (d)-(f) 50 mins with CO_2- or H_2O-activated biochars. The data for biochars activated in steam were published before [14] and are used here for comparison.

6.3.4.2 The effects of reforming agent on the catalytic activities of H_2O- or CO_2-activated biochar catalysts

The catalytic activities of biochar catalysts activated by H_2O or CO_2 for subsequent steam or dry reforming of tar are further compared in *Figure* 6. *7*. In each legend (e.g. "H_2O – CO_2 R") in *Figure* 6. *7*, the first part (e.g. "H_2O") refers to the atmosphere for biochar activation and the second part (e.g. "CO_2 R") refers to the atmosphere for the subsequent *in situ* reforming of tar. The detailed experimental conditions for each legend have been included in *Table 6. 1*. As can be seen in *Figure* 6. *7*, the order of both the tar yield and the UV-fluorescence intensity of tars is: CO_2 – CO_2 R > CO_2 – H_2O R > H_2O – CO_2 R > H_2O - H_2O R. For the reforming of tar in H_2O or CO_2, the H_2O-activated biochar has higher catalytic activity (lower yield of tar and of aromatic ring systems) than the CO_2-activated biochar. The UV-fluorescence intensity indicates the relative yields of the relatively large aromatic ring systems in tar [14,28]. The lower fluorescence intensities of tar after reforming with H_2O-activated biochar suggest that

the H_2O-activated biochar has higher catalytic activities with respect to the destruction of relatively large aromatic ring systems in tar than the CO_2-activated biochar.

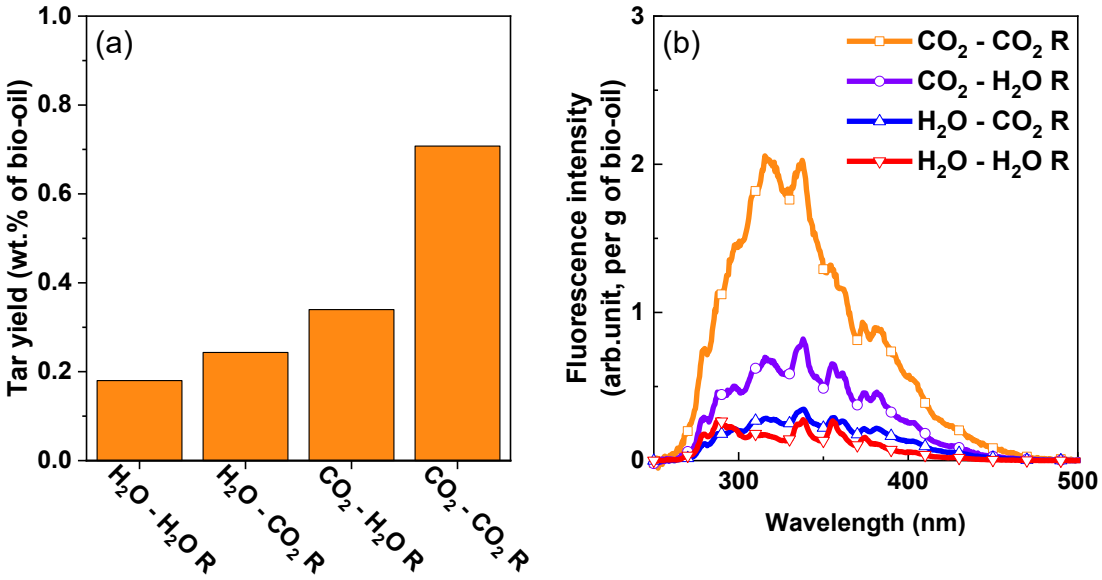

Figure 6. 7. (a) Tar yields and (b) constant energy (−2800 cm^{-1}) synchronous spectra of tars after steam or dry reforming with biochar catalysts activated in H_2O or CO_2. The data for biochars activated in steam were published before [14] and are used here for comparison.

Interestingly, the results in *Figure* 6. *7* show that the gas used for biochar activation play a more important role in tar destruction than that used for reforming under the experimental conditions used in this study. For example, when CO_2-activated biochar was used, the tar yield and fluorescence intensity after reforming in H_2O were much lower than those after reforming in CO_2. The supply of H_2O during tar reforming has clearly improved tar cracking when CO_2-activated biochar was used. The results have further confirmed that steam plays an important role in improving and maintaining the catalytic activity of biochar during tar reforming [5]. With the supply of H_2O, the gasification of biochar by H_2O during tar reforming could change its structure and then improve the catalytic activity of biochar [5].

6.3.4.3 Differences in the chemical structure between H_2O- or CO_2-activated biochar catalysts before and after tar reforming in H_2O or CO_2

Overall, tar reforming is the result of complex reactions occurring in the gas phase and at the gas-solid interface, which can be affected by the structural properties of biochar (partly

affected by biochar activation in H_2O or CO_2), the structural properties of tar compounds, as well as the reforming agent. Our previous study [14] has illustrated that O-containing functional groups, especially the aromatic C-O structures, in biochar can enhance the catalytic activity of biochar for steam tar reforming. As a continuation, this study examined the contents of the O-containing functional groups and the aromatic C-O structures of H2O- or CO2-activated biochar catalysts before and after reforming in H_2O or CO_2, as is shown in *Figure* 6. *8*.

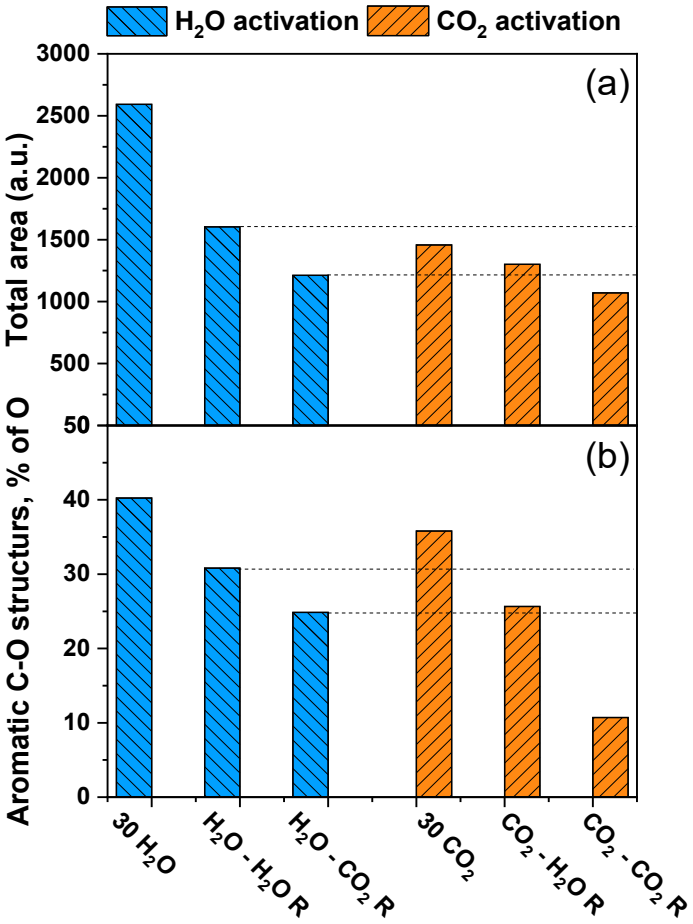

Figure 6. 8. (a) Total Raman area (800 – 1800 cm^{-1}) from Raman spectroscopy and (b) relative content of aromatic C-O structures obtained from XPS O 1s spectra of the biochars activated by H_2O or CO_2 before and after H_2O or CO_2 reforming. "30 H_2O (CO_2) means "after 30 min of activation with H_2O (CO_2) before tar reforming". The data for biochars activated in steam were published before [14] and are used here for comparison.

From *Figure* 6. 8(a), it is clear that, after the same activation time, a higher total Raman area was achieved in biochar activated in H_2O than that in CO_2-activated biochar. After tar reforming in H_2O (or CO_2), the total Raman area in H_2O-activated biochar is still higher than that in CO_2-activated biochar. As mentioned above, a higher total Raman area, in the region measured, represents a higher content of O-containing functional groups in biochar. Therefore, H_2O activation has resulted in a biochar with higher content of O-containing functional groups than that produced by CO_2 activation. Moreover, the content of O-containing functional groups in the H_2O activated biochar was still higher than that in the CO_2 activated biochar after H_2O or CO_2 reforming. Similar trends were observed for the evolution in the relative content of aromatic C-O structures from *Figure* 6. *8*(b). The higher contents of O-containing functional groups and aromatic C-O structures in H_2O-activated biochar compared to CO_2-activated biochar corresponds to the higher catalytic activity of biochar activated in H_2O than that activated in CO_2, as discussed above.

Furthermore, for both the H_2O and CO_2-activated biochars, the contents of O-containing functional groups (total Raman area) and aromatic C-O structure are higher after reforming in H_2O than those after reforming in CO_2. This means that the reduction of O-containing functional groups and aromatic C-O structures in H_2O reforming was slower than was the case in CO_2 reforming. Consequently, the reduction in the catalytic activity of biochar during reforming in H_2O was slower than it was in CO_2. This explains the more rapid reforming in H_2O than in CO_2 observed in.*Figure* 6. *7*. These results imply that steam plays an important role in improving and maintaining the catalytic activity of biochar during reforming. During H_2O reforming, extra O-containing functional groups and aromatic C-O structures could be generated with the continuous gasification of biochar with added excess H_2O [5,34]. Consequently, the decrease in the catalytic activity of biochar which resulted from the reduction of O-containing functional groups and aromatic C-O structures was slowed down.

6.4 Conclusions

The different catalytic activities between H_2O and CO_2-activated biochars for tar reforming were investigated. During both steam and dry reforming of tar, the CO_2-activated biochar showed lower catalytic activities than the biochar activated in H_2O for the same time. After

the same activation time, the CO_2-activated biochar had a lower content of O-containing functional groups and aromatic C-O structures than the H_2O-activated biochar. This could be the reason for the lower catalytic activities of CO_2-activated biochar compared to H_2O-activated biochar. Besides, tar reforming in CO_2 was always slower than that in H_2O irrespective of the gasifying agent that used for biochar activation. The content of O-containing functional groups and aromatic C-O structures in biochar after steam reforming was higher than that after dry reforming. It is believed that extra supply of H_2O during reforming is essential for improving and maintaining the catalytic activities of biochar.

6.5 References

[1] Li C-Z. Special issue—gasification: a route to clean energy. Process Saf Environ Prot 2006;84:407–8.

[2] Li C-Z. Importance of volatile-char interactions during the pyrolysis and gasification of low-rank fuels - A review. Fuel 2013;112:609–23.

[3] Sikarwar VS, Zhao M, Clough P, Yao J, Zhong X, Memon MZ, Shah N, Anthony EJ, Fennell PS. An overview of advances in biomass gasification. Energy Environ Sci 2016;9:2939–77.

[4] Li C, Suzuki K. Tar property, analysis, reforming mechanism and model for biomass gasification-An overview. Renew Sustain Energy Rev 2009;13:594–604.

[5] Song Y, Wang Y, Hu X, Xiang J, Hu S, Mourant D, Li T, Wu L, Li C-Z. Effects of volatile-char interactions on in-situ destruction of nascent tar during the pyrolysis and gasification of biomass. Part II. Roles of steam. Fuel 2015;143:555–62.

[6] Wang Y, Hu X, Song Y, Min Z, Mourant D, Li T, Gunawan R, Li C-Z. Catalytic steam reforming of cellulose-derived compounds using a char-supported iron catalyst. Fuel Process Technol 2013;116:234–40.

[7] Min Z, Asadullah M, Yimsiri P, Zhang S, Wu H, Li C-Z. Catalytic reforming of tar during gasification. Part I. Steam reforming of biomass tar using ilmenite as a catalyst. Fuel 2011;90:1847–54.

[8] Min Z, Zhang S, Yimsiri P, Wang Y, Asadullah M, Li C-Z. Catalytic reforming of tar during gasification. Part IV. Changes in the structure of char in the char-supported iron catalyst during reforming. Fuel 2013;106:858–63.

[9] Min Z, Yimsiri P, Asadullah M, Zhang S, Li C-Z. Catalytic reforming of tar during gasification. Part II. Char as a catalyst or as a catalyst support for tar reforming. Fuel 2011;90:2545–52.

[10] Song Y, Zhao Y, Hu X, Zhang L, Sun S, Li C-Z. Destruction of tar during volatile-char interactions at low temperature. Fuel Process Technol 2018;171:215–22.

[11] Song Y, Wang Y, Hu X, Hu S, Xiang J, Zhang L, Zhang S, Min Z, Li C-Z. Effects of volatile-char interactions on in situ destruction of nascent tar during the pyrolysis and gasification of biomass. Part I. Roles of nascent char. Fuel 2014;122:60–6.

[12] Hosokai S, Norinaga K, Kimura T, Nakano M, Li C-Z, Hayashi J-I. Reforming of volatiles from the biomass pyrolysis over charcoal in a sequence of coke deposition and steam gasification of coke. Energy and Fuels 2011;25:5387–93.

[13] Ravenni G, Elhami OH, Ahrenfeldt J, Henriksen UB, Neubauer Y. Adsorption and decomposition of tar model compounds over the surface of gasification char and active carbon within the temperature range 250–800 °C. Appl Energy 2019;241:139–51.

[14] Liu Y, Paskevicius M, Wang H, Parkinson G, Veder JP, Hu X, Li C-Z. Role of O-containing functional groups in biochar during the catalytic steam reforming of tar using the biochar as a catalyst. Fuel 2019;253:441–8.

[15] Feng D, Zhao Y, Zhang Y, Sun S, Meng S, Guo Y, Huang Y. Effects of K and Ca on reforming of model tar compounds with pyrolysis biochars under H_2O or CO_2. Chem Eng J 2016;306:422–32.

[16] Guizani C, Jeguirim M, Gadiou R, Escudero Sanz FJ, Salvador S. Biomass char gasification by H_2O, CO_2 and their mixture: Evolution of chemical, textural and structural properties of the chars. Energy 2016;112:133–45.

[17] Wang S, Wu L, Hu X, Zhang L, Li T, Li C-Z. Effects of the Particle Size and Gasification Atmosphere on the Changes in the Char Structure during the Gasification of Mallee Biomass. Energy and Fuels 2018;32:7678–84.

[18] Wang S, Wu L, Hu X, Zhang L, O'Donnell KM, Buckley CE, Li C-Z. An X-ray photoelectron spectroscopic perspective for the evolution of O-containing structures in char during gasification. Fuel Process Technol 2018;172:209–15.

[19] Dong L, Asadullah M, Zhang S, Wang XS, Wu H, Li C-Z. An advanced biomass gasification technology with integrated catalytic hot gas cleaning Part I. Technology and initial experimental results in a lab-scale facility. Fuel 2013;108:409–16.

[20] Ravenni G, Sárossy Z, Ahrenfeldt J, Henriksen UB. Activity of chars and activated carbons for removal and decomposition of tar model compounds – A review. Renew Sustain Energy Rev 2018;94:1044–56.

[21] Advanced biomass gasification technology, Australian Renewable Energy Agency. https://arena.gov.au/projects/advanced-biomass-gasification-technology/. (accessed October 28, 2019).

[22] Grinding pyrolysis, Renergi Pty Ltd. http://www.renergi.net/grinding_pyrolysis. (accessed October 28, 2019).

[23] Wu H, Quyn DM, Li C-Z. Volatilisation and catalytic effects of alkali and alkaline earth metallic species during the pyrolysis and gasification of Victorian brown coal. Part III. The importance of the interactions between volatiles and char at high temperature. Fuel 2002;81:1033–9.

[24] Min Z, Yimsiri P, Zhang S, Wang Y, Asadullah M, Li C-Z. Catalytic reforming of tar during gasification. Part III. Effects of feedstock on tar reforming using ilmenite as a catalyst. Fuel 2013;103:950–5.

[25] Jiang S, Hu X, Xia D, Li C-Z. Formation of aromatic ring structures during the thermal treatment of mallee wood cylinders at low temperature. Appl Energy 2016;183:542–51.

[26] Sathe C, Pang Y, Li C-Z. Effects of heating rate and ion-exchangeable cations on the pyrolysis yields from a Victorian brown coal. Energy and Fuels 1999;13:748–55.

[27] Li C-Z, Sathe C, Kershaw JR, Pang Y. Fates and roles of alkali and alkaline earth metals during the pyrolysis of a Victorian brown coal. Fuel 2000;79:427–38.

[28] Li C-Z, Wu F, Cai HY, Kandiyoti R. UV-Fluorescence Spectroscopy of Coal Pyrolysis Tars.

Energy and Fuels 1994;8:1039–48.

[29] Li X, Hayashi J-I, Li C-Z. Volatilisation and catalytic effects of alkali and alkaline earth metallic species during the pyrolysis and gasification of Victorian brown coal. Part VII. Raman spectroscopic study on the changes in char structure during the catalytic gasification in air. Fuel 2006;85:1509–17.

[30] Hosokai S, Kumabe K, Ohshita M, Norinaga K, Li C-Z, Hayashi J-I. Mechanism of decomposition of aromatics over charcoal and necessary condition for maintaining its activity. Fuel 2008;87:2914–22.

[31] Feng D, Zhao Y, Zhang Y, Gao J, Sun S. Changes of biochar physiochemical structures during tar H2 O and CO2 heterogeneous reforming with biochar. Fuel Process Technol 2017;165:72–9.

[32] Li X, J-I. H, Li C-Z. FT-Raman spectroscopic study of the evolution of char structure during the pyrolysis of a Victorian brown coal. Fuel 2006;85:1700–7.

[33] Zhang S, Min Z, Tay H-L, Asadullah M, Li C-Z. Effects of volatile–char interactions on the evolution of char structure during the gasification of Victorian brown coal in steam. Fuel 2011;90:1529–35.

[34] Feng D, Zhang Y, Zhao Y, Sun S, Gao J. Improvement and maintenance of biochar catalytic activity for in-situ biomass tar reforming during pyrolysis and H_2O/CO_2 gasification. Fuel Process Technol 2018;172:106–1

Chapter 7

Insights into the mechanism of tar reforming using biochar as a catalyst

Y. Liu, M. Paskevicius, H. Wang, G. Parkinson, J. Wei, A. M.A, C.-Z. Li, Insights into the mechanism of tar reforming using biochar as a catalyst, Fuel, 296 (2021) 120672. https://doi.org/10.1016/j.fuel.2021.120672.

Abstract

Biochar is an efficient catalyst for tar removal from syngas during biomass gasification. The aim of this research is to investigate the mechanism of tar reforming using biochar as a catalyst. A series of in situ steam tar reforming experiments were carried out using a two-stage fluidized-bed/fixed-bed reactor at 800 °C. Mallee wood biochar (106–250 μm) was activated in 15 vol. % H_2O balanced with Ar for different times (0–50 min) and then used as a catalyst for tar reforming. The on-line gas composition, light tar composition and the pore structure of biochar were analysed using mass spectrometer (MS), GC-MS and synchrotron small angle X-ray scattering (SAXS) respectively. An increased ratio of H_2/CO was observed after reforming with biochar compared to reforming without biochar. The destruction of light tar compounds, especially the non-oxygen-containing compounds, was significantly enhanced when activated biochars were used. Steam activation increased the specific surface area (SSA), micro- and mesopore volumes in biochar while the values stayed almost unchanged during tar reforming. Results indicate that the micro- and mesopores in biochar promote the diffusion of both small and large tar molecules into the internal surface of biochar. However, the catalytic activity of biochar for tar reforming mainly depends on the content of O-containing functional groups in biochar. The O-containing functional groups facilitate the dissociation of tar molecules to form tar radicals, giving rise to the enhanced tar removal efficiency. Moreover, the formation of tar radicals over O-containing functional groups appears as the rate-limiting step in the process of catalytic reforming of tar over biochar catalysts.

7.1 Introduction

Biomass gasification is considered to be one of the most promising technologies to expand the contribution of biomass to the world's renewable energy supply [1,2]. However, tar formation is practically unavoidable during gasification, and the removal of tar from syngas is one of the major technical barriers that limits the commercialization of gasification technologies [3]. Extensive gas cleaning is required before the product gas is used for electricity generation, as well as for the synthesis of chemicals and transportation fuels.

Amongst the various methods used for tar removal, catalytic steam reforming appears to be the most promising technique [4,5]. The use of biochar as a catalyst is particularly attractive due to its high catalytic efficiency and low cost [6–9]. In addition, the energy value of spent biochar can be recovered simply by further gasifying or burning. Understanding the reaction mechanism of tar reforming over biochar is critical for optimizing the catalytic performance of biochar, as well as for the development of gasification technologies.

It has been proposed that the two main reaction pathways of tar during steam reforming are homogeneous and heterogeneous reforming [10,11]. However, due to the complex composition of tar as well as the complex properties of biochar, the reforming mechanism of tar using biochar as a catalyst has not yet been fully elucidated. Particularly, little is known about the interactions between tar molecules and the active sites in biochar in the heterogeneous reforming process. Great efforts [10,12–19] have been made to study the factors that influence the catalytic activities of tar removal over biochar catalysts. Apart from the experimental conditions such as temperature [17,20] and gasifying agents [12,16], the physicochemical properties of biochar, particularly the porous structure (large specific surface area) [14,21], the surface chemistry [6,12,13], as well as the inherent alkali and alkaline earth metallic (AAEM) species [15] are considered to be the main factors that affect the catalytic activity of biochar. However, the results [14,21,22] are not consistent regarding the relative importance of the micro- and mesopores in biochar. The exact role of the active sites in biochar for heterogeneous tar reforming is also ambiguous. Above all, it remains unclear which step involved in the heterogeneous reforming process is the rate-determining step. Therefore, further studies are needed to fully understand the mechanism of tar reforming over biochar catalysts.

In our previous studies [12,13], the O-containing functional groups, especially the aromatic C-O structures, in biochar have been recognized to be a key factor influencing its catalytic activity. It is also critical to investigate the evolution of the pore structure of biochar during tar reforming in order to identify the key property of biochar that limits its catalytic activity for tar reforming. Moreover, the distribution of product gas and the formation rate of each gas is directly related to the reaction types and reaction rate. The behaviour of various tar molecules during tar reforming would be also differ with their own structural features and activities. For example, some tar compounds would be preferentially reformed over biochar,

whereas some may mainly be destructed in the gas phase [16]. Therefore, a comprehensive analysis of tar composition and the product gas composition is also essential for a better understanding the reaction mechanism of tar reforming.

For these reasons, following our previous study [13], we investigate the evolution in the pore structure of biochar catalysts as well as the gas composition during reforming in this work. Moreover, the tar composition after steam reforming was also analysed with the aim to identify the main tar compounds that are preferentially destructed over biochar surface. In the end, a reforming mechanism is proposed, taking into consideration the interactions between O-containing functional groups and tar components. The possible deactivation mechanism of biochar catalyst during steam tar reforming is also considered. Our results would provide critical information on identifying the decisive factor influencing the catalytic activity of biochar, as well as on the understanding of the mechanism of tar destruction over biochar catalysts.

7.2 Experimental

7.2.1 In situ steam reforming of tar using biochar as a catalyst

Steam tar reforming experiments were carried out using a three-frit two-stage fluidised-bed/fixed bed quartz reactor [23,24], as shown in *Figure 7. 1*. The experimental conditions (800 °C, 15 vol. % H_2O mixed with Ar), biochar (106–250 µm) and bio-oil samples used in this study were the same as those in our previous work [13]. Briefly, biochar samples were preloaded on the middle frit and in-situ activated in a 15 vol. % H_2O mixed with Ar before acting as a catalyst. After the activation time (0 - 50 min) was reached, bio-oil was injected into the reactor at a rate of 0.20 ml min-1. Tar was generated immediately when the bio-oil reached the reaction zone at 800 °C. The generated tar was mixed with steam before passing through the biochar bed and going through catalytic steam reforming. When the required time was reached, the experiments were terminated by stopping the feeding of bio-oil and steam. The reactor was then lifted out of the furnace and cooled down under argon flow.

The same method in our previous studies [24,25] was used to collect tar samples after reforming. Briefly, the reactor outlet was connected to three condensation traps filled with a

mixture of HPLC-grade chloroform and methanol (4:1 by vol). Tar was then condensed in the mixture and collected for further analysis.

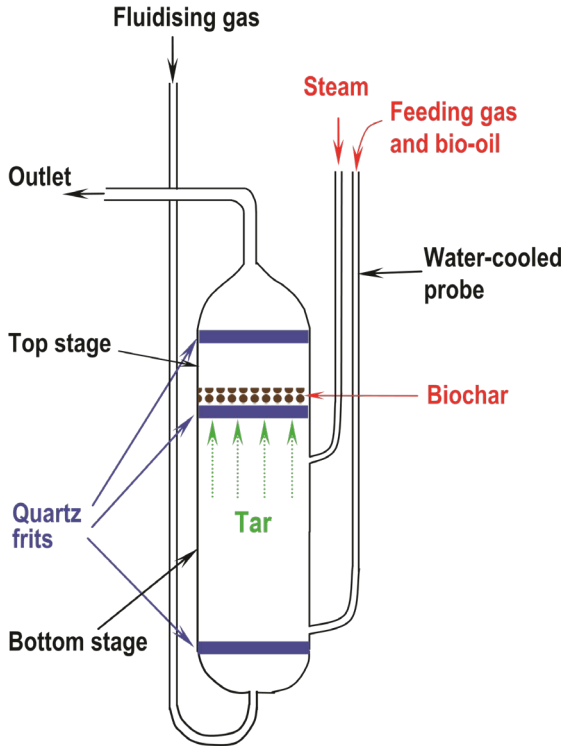

Figure 7. 1. A schematic diagram of the three-frit fluidized-bed/fixed-bed quartz reactor (modified from Ref. [22] with permission from Elsevier).

7.2.2 Characterisation of reforming products

After tar condensation and gas cooling, the outlet gas stream was connected to a QMS Prisma™ 200 mass spectrometer (MS) in order to monitor the real-time gas composition [26]. The MS was calibrated using a standard gas mixture (ISO Guide 34 accredited) before using. As stated in our previous work [26], the CO signal was deconvoluted by subtracting the contribution of CO_2 at m/z = 28 as the mass fragment of CO_2 at m/z = 28 overlaps with CO signal. The molar/volume ratios of H_2, CO, CO_2, and CH_4 were calculated respectively afterwards.

Tar samples were analysed using an Agilent GC–MS (a 6890 series GC plus a 5973 MS detector) with helium as the carrier gas. Detailed parameters of the measurement can be found elsewhere [27,28]. The detected compounds corresponding to each GC peak were

identified based on the standard spectra of compounds in the National Institute of Standards and Technology (NIST) library and/or the spectra of known species injected. The relative yield of each compound (X) was calculated by multiplying the peak area by the ratio of the amount of total tar solution collected and bio-oil injected (Eq.7.1). Therefore, the relative yield of each compound was based on per g of bio-oil.

$$Relative\ yield\ of\ tar\ compound\ X\ = \frac{mass\ of\ total\ tar\ solution}{mass\ of\ bio{-}oil\ fed}\ integrated\ peak\ area\ of\ compound\ X \quad (7.1)$$

The porosity of biochar was characterised using Small Angle X-ray Scattering (SAXS) with a Pilatus 1-M detector at the Australian Synchrotron in Melbourne [29]. The procedures of measurement and data processing were detailed included in our previous studies [30,31]. Briefly, the measurements were conducted at two camera lengths (3343 mm and 959 mm) to achieve a wide q (q is the scattering vector $q = (4\pi/\lambda)\sin(\theta/2)$, λ (λ = 1.03 $Å^{-1}$) and θ are the wavelength and scattering angle) range from 0.005 to 1.5 $Å^{-1}$, respectively, which are appropriate for an approximate pore diameter ranging from 0.4 to 125 nm. The SAXS intensities on absolute scale [32,33] were further processed with the unified model [34] in Irena [35] to obtain the specific surface area (SSA) and pore size distribution of biochar samples.

7.2 Results and discussion

7.2.1 Evolution in the gas composition

Before analysis, it should be noted that the gas composition is the combined result of both tar reforming and the simultaneous gasification of biochar. The gas composition after 30 mins steam reforming with and without biochar is given as an example to study the effect of a biochar catalyst on the gas composition, as shown in *Table 7. 1*. Compared with reforming without biochar, the content of H_2 greatly increased when reforming with biochar. The content of CO_2 also increased while the content of CO and CH_4 decreased after using biochar as a catalyst. As such, the ratio of H_2/CO increased after reforming with biochar. It seems that the formation rate of H_2 was increased in the presence of biochar. This could be due to the

enhanced catalyst (biochar)-gas (tar molecules) reactions, leading to the increased production of H_2.

Table 7. 1. Product gas composition after steam reforming for 30 min with and/or without biochar.

Experiment conditions	Molar gas composition[a]				
	CO	CO_2	H_2	CH_4	H_2/CO molar ratio
Bio-oil only	62%	14%	4%	21%	0.07
Biochar only	37%	30%	20%	13%	0.55
Reforming with 0A biochar	38%	26%	22%	14%	0.58
Reforming with 10A biochar	35%	31%	22%	12%	0.63
Reforming with 20A biochar	33%	32%	23%	12%	0.70
Reforming with 30A biochar	30%	38%	21%	11%	0.70
Reforming with 40A biochar	29%	37%	25%	9%	0.80
Reforming with 50A biochar	29%	32%	28%	11%	0.83

Note: [a] dry basis; 0-50A biochar represent the biochar that was activated by steam for 0-50 min.

7.2.2 Evolution of light tar composition

Tar is a complex mixture of a large number of single aromatics (1 benzene ring), polycyclic aromatic hydrocarbon (PAH) compounds, along with other heterocyclic compounds such as O-containing tar compounds. Our previous study [13] investigated the evolution of relatively large PAH compounds in tar using UV-fluorescence spectroscopy. To obtain a more comprehensive understanding of the transformation and conversion of tar during steam reforming using biochar as a catalyst, we used GC-MS to investigate the evolution of light tar composition in the present study. It should be pointed out that GC-MS has limitations in detecting tar with high molecular mass and highly polar compounds, thus only the relatively light tar compounds can be detected.

Figure 7. 2 and *Figure* 7. 3 show the GC-MS total ion chromatograms of tar samples after steam reforming with/without biochar with some relevant tar compounds marked. The

peak height can roughly represent the content of the corresponding compound. It should be kept in mind that, in the process of tar reforming, some tar molecules such as phenol, indene and styrene can be formed from the breakdown of larger tar molecules. Therefore, the GC-MS detected tar compounds are the net results of their reforming/removal and formation. *Figure 7. 2* compares the effect of steam activation time of biochar on the light tar composition. After steam reforming for 30 min, there is a clear trend when reforming with biochar that has been activated for different times, where the more activated biochar results in lower yields of these tar compounds. That is to say, longer biochar activation enhances the reforming/removal of light tar compounds. The light tar compounds were nearly completely reformed/removed after reforming for 10 - 30 min with biochar activated for 40 min in *Figure 7. 3.* However, peaks of styrene and naphthalene appear when the reforming time is increased to 50 min, as shown in *Figure 7. 3*c. This means that the activity of biochar on the reforming of light tar compounds decreased when the reforming time extended to 50 min. In our previous work [13], similar trend on the tar yield and the yield of relatively large aromatic ring system was observed. Thus, steam activation can enhance the catalytic activity of biochar on both the destruction of relatively large aromatic ring systems [13] and the removal of light tar compounds. Moreover, the catalytic activity of biochar decreases over the course of tar reforming [13]. The reduced catalytic activity of biochar at longer reforming time (e.g. 50 min) resulted in lower reforming rate of light tar compounds detected by GC-MS compared to the rate of their formation. As such, increase in the contents of light tar compounds was observed here.

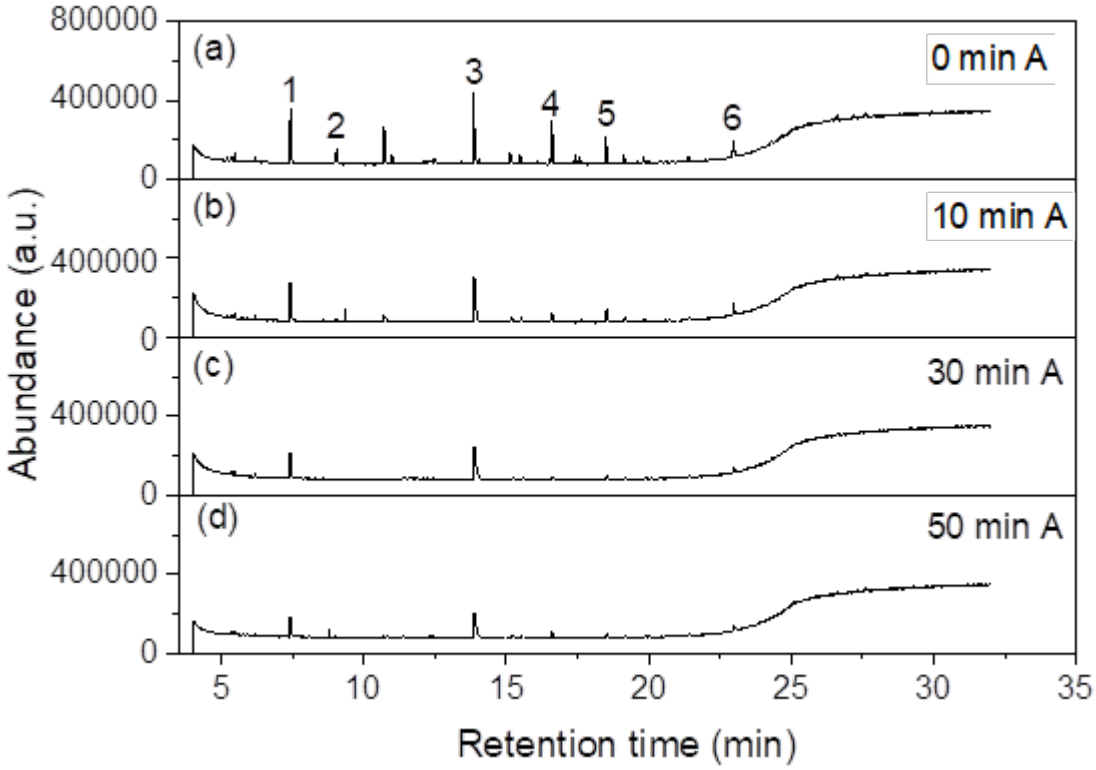

Figure 7. 2. GC–MS total ion chromatograms of the tars after reforming for 30 min with biochar activated for (a) 0 min, (b) 10 min, (c) 30 min and (d) 50 min. Note: A for activation; peak 1-styrene, peak 2-phenylacetylene, peak 3-naphthalene, peak 4-phenol, peak 5-acenaphthylene, peak 6-phenanthrene.

Studies [6,16,37] have found that the structure of tar molecules (aromatic ring sizes, functional groups, etc.) can affect its reactivity during reforming. For example, the aromatics with substituted groups or O-containing groups were reformed/removed relatively easily [16]. For this reason, the major light tar compounds detected by GC-MS were classified and categorized into five component groups based on the structural features of tar compounds in this study, as shown in Table 7. 2.

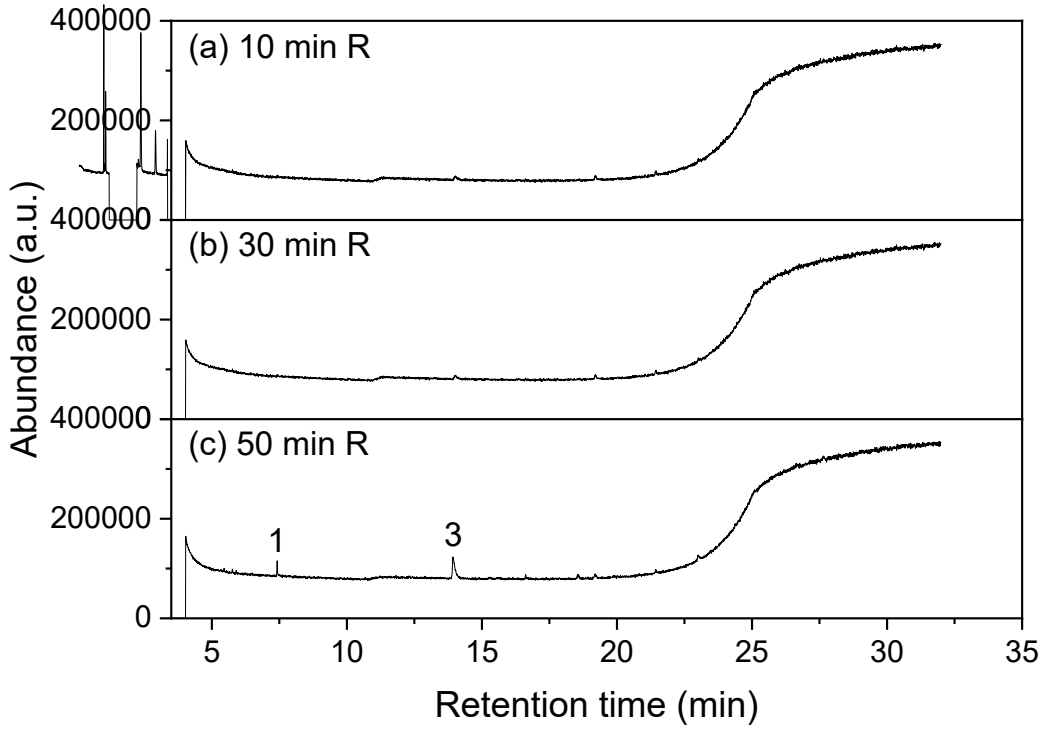

Figure 7. 3. GC–MS total ion chromatograms of the tars after reforming for (a) 10 min, (b) 30 min and (c) 50 min with biochar activated for 40 min. Note: R for reforming; peak 1-styrene, peak 3-naphthalene.

Table 7. 2. Classification of light tar compounds based on their structural features.

Group number	Compound groups	Compounds
1	naphthalene	naphthalene
2	phenanthrene	phenanthrene
3	aromatics (1-3 benzene rings) with penta-cycled ring or substituted groups	styrene, phenylacetylene, acenaphthylene, fluorene, indene, 1-methyl naphthalene, 2-methyl naphthalene
4	O-containing compounds	phenol, 3,4,5-trimethoxybenzaldehyde, dibenzofuran, benzofuran

The relative yield of different component groups in tars obtained from steam reforming with or without biochar are displayed in *Figure 7. 4.* The relative yields are

presented on the basis of per g of bio-oil. For all the tar samples from steam reforming, with or without biochar, the relative yields of naphthalene, and aromatics with penta-cycled ring or substituted groups, were much higher than those of phenanthrene or O-containing tar compounds. This has again indicated that the reactivity of tar molecules depends on their structural features. The aromatics with larger rings or O-containing groups were easier to be reformed/removed than smaller hydrocarbon aromatics [6,37,38].

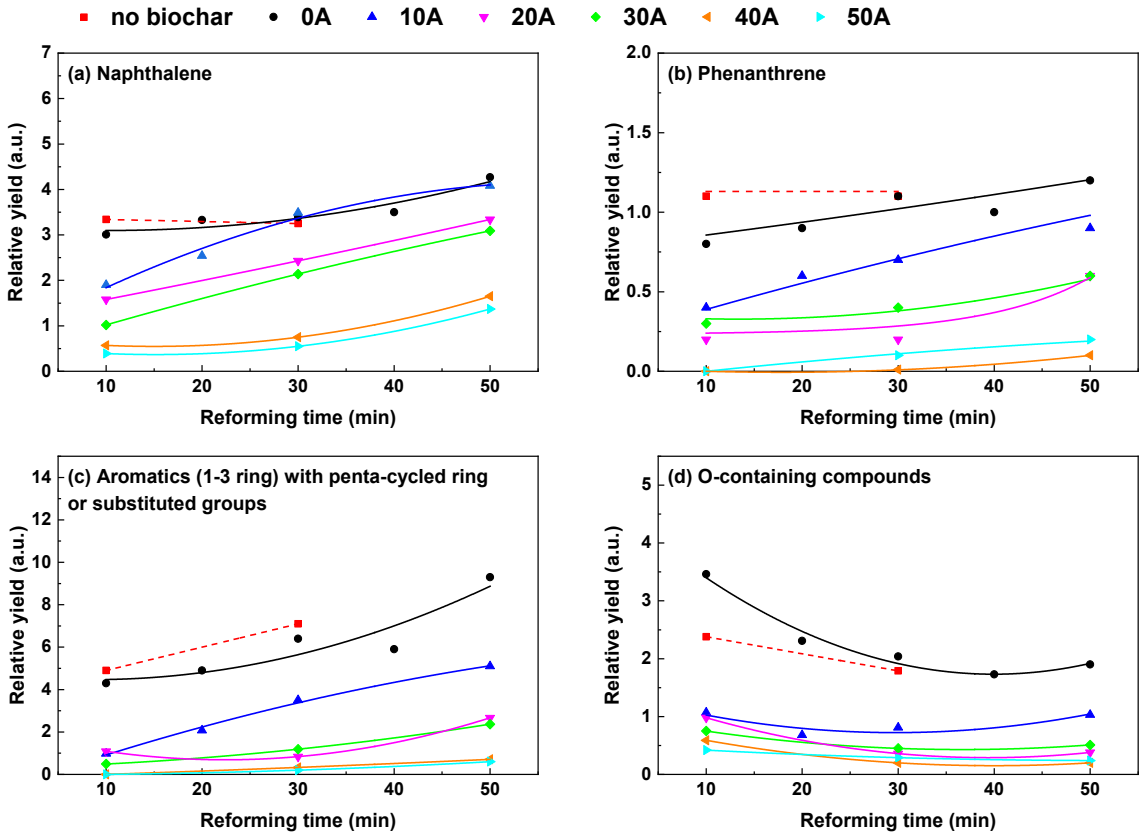

Figure 7. 4. Relative yield of the classified component groups from GC-MS: (a) naphthalene, (b) phenanthrene, (c) aromatics (1-3 benzene rings) with penta-cycled ring or substituted groups, (d) O-containing tar compounds. Note: 0-50A represents for 0-50 min activation.

The relative yield of light tar compounds all clearly decrease after reforming with activated biochars compared to reforming with raw biochar (0A) and/or without biochar (no biochar). The longer the activation time of biochar, the lower the yield of non-oxygen-containing compounds (*Figure 7. 4*a, b and c), with the same reforming time. Additionally, the yield of these compounds increased as a function of the reforming time. The results show that the activation of biochar has enhanced the removal of light tar compounds. Particularly, the

decrease of light aromatics with penta-cycled ring or substituted groups (*Figure 7. 4*c) was greater than other component groups such as naphthalene when using biochar activated for longer times. On the contrary, the variation in the activation time of biochar showed little effect on the reduction of the O-containing tar compounds (*Figure 7. 4*d). Moreover, the yield of O-containing tar compounds almost stabilised at the same level as the reforming proceeded.

The trends of non-oxygen-containing groups illustrated by GC-MS are similar to that of the relatively large aromatic ring systems illustrated by UV-fluorescence spectroscopy in our previous study [13]. It was found that the yield of relatively large aromatic ring systems decreased when the activation time of biochar increased. The extension of reforming time led to a reduction in the yield of the relatively large aromatic ring systems. It was also confirmed that the steam activation of biochar greatly enhances its catalytic activity by increasing the content of O-containing functional groups. Besides, the catalytic activity of biochar reduces with increasing reforming time, with a decreasing content of O-containing functional groups in biochar. It seems that the catalytic activities of biochar in reforming light non-oxygen-containing tar compounds are also closely related to the content of O-containing functional groups in biochar. Whereas, the destruction of O-containing tar compounds is not greatly affected by the reduction in the O-containing functional groups of biochar.

The observations from UV-fluorescence spectroscopy [13] and GC-MS imply that the O-containing functional groups in biochar could be the main active sites for the reforming of large aromatic systems and light non-oxygen-containing tar compounds. In contrast, there could be other types of active sites in biochar on which the breakdown of O-containing tar compounds mainly take place. As such, the breakdown of O-containing tar compounds is not significantly improved with the increase of the O-containing functional groups in biochar, which result from longer activation times. Moreover, the active sites for O-containing tar compounds seem to show no sign of deactivation with the extension of reforming time (*Figure 7. 4*d). One possible explanation is that these O-containing tar compounds are reformed mainly through conversion into gases rather than coke formation by condensation over biochar. Also, it's possible that O-containing tar compounds are mainly adsorbed and reformed over other active sites (such as carbon) instead of O-containing functional groups in biochar.

7.2.3 Evolution in the pore structure of biochar catalysts

It has been suggested that that the pore structure of a porous catalyst is an important factor influencing its catalytic activity [39]. Therefore, it is necessary to study the changes in pore structure of biochar during steam activation and tar reforming.

Figure 7. 5 shows changes in the specific surface area (SSA), micropore volume (pore width < 2 nm) and mesopore volume (2 nm < pore width < 50 nm) of biochar during the steam activation and/or tar reforming processes. During activation/gasification (no bio-oil, dashed line in *Figure 7. 5*), the SSA (*Figure 7. 5*) of biochar increases with increasing activation time and reaches a maximum in 40 min before decreasing when the activation was prolonged to 50 min. The micropore volume (*Figure 7. 5*b) and mesopore volume (*Figure 7. 5*c) also show an increasing trend at the early stage of activation before reaching a limiting size. The increased SSA, micro- and mesopore volumes are the result of carbon removal by steam activation/gasification of biochar, generating new pores, especially micropores [40,41]. The decreased SSA and micropore volume at the late stage of activation/gasification are attributed to the enlargement of micropores to mesopores and mesopores to macropores (pore width > 50 nm), meaning that fewer micro- and mesopores are left after a certain conversion level [40].

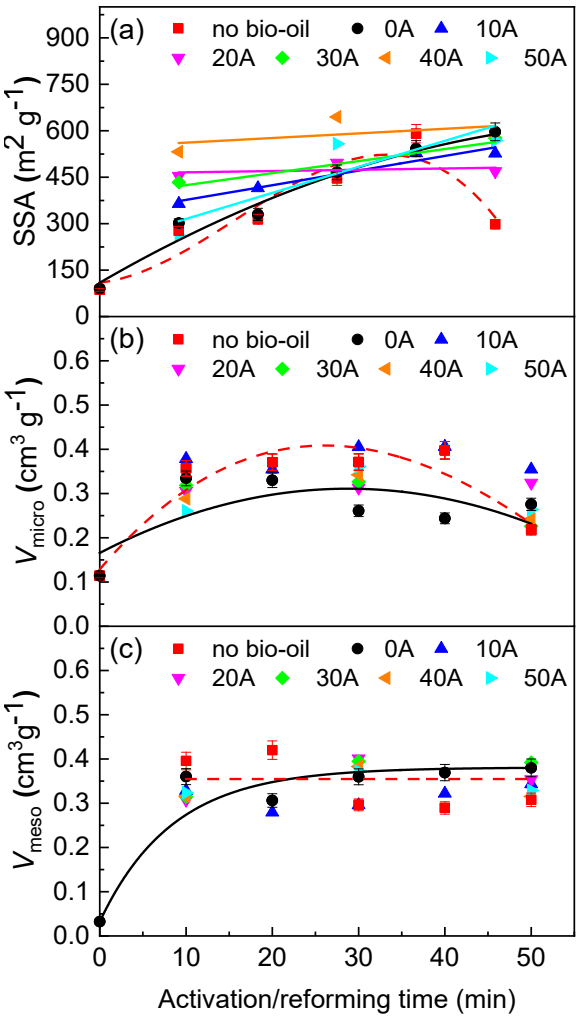

Figure 7. 5. Evolution of (a) SSA, (b) micropore volume (V_{micro}) and (c) mesopore volume (V_{meso}) of biochar during steam activation (dashed line) and reforming (solid line and data points) from SAXS data. Note: 0-50A represents for 0-50 min activation, the dotted and plain lines are referred to 0A.

The pores developed during activation could enhance the diffusion of tar molecules to the internal catalytically active sites (e.g. O-containing functional groups), improving the efficiency of tar destruction. It is also reasonable to believe that both the micro- and mesopores in biochar are important in providing channels for the diffusion of the small and large tar molecules considering that big tar molecules couldn't diffuse into micropores. Moreover, as stated above, an abundance of O-containing functional groups were found to be produced during steam activation of biochar previously [12,13]. The simultaneous generation of O-containing functional groups and pores in biochar during steam activation

suggests that these O-containing functional groups are likely to distributed in the newly created pores.

For the raw biochar that went through tar reforming (black solid line, 0A), the development of increased SSA and pore volume with increasing time is analogous to that in biochar that only underwent gasification (red dash line), where the values of SSA and pore volumes are similar between the two cases. The presence of tar seems to have little effect on the development of the pore structure in raw biochar. In the cases of activated biochars (0-50A), the SSA and pore volumes stayed similar to one another and almost unchanged in the process of tar reforming. This indicates that a high surface area and pore volume of biochar does not always lead to a high efficiency of tar removal, which is quite dependent on the activation time (Figure 7. *4*). Furthermore, a good trend between the content of O-containing functional groups in biochar and its catalytic activity for tar reforming was observed previously [13]. When the O-containing functional groups dramatically reduce with increasing reforming time [13], regardless of the surface area and pore volumes observed here, the overall catalytic activity of the biochar decreases. The results suggest that the O-containing functional groups play a more important role than surface morphology in influencing the catalytic activity of biochar for tar reforming. It can also be inferred that, under the experimental conditions in this work, the access and diffusion of tar molecules through pores is not a key step in determining the efficiency of tar removal over biochar. Our results disagree with some previous studies [14,21], in which they reported that the specific surface area is the crucial factor determining the catalytic activity of biochar. Therefore, focus should be directed towards optimising the O-containing functional groups when producing a highly active biochar catalyst.

7.2.4 Mechanism of tar reforming over biochar catalyst

Based on the above discussion, the following mechanism of tar reforming over biochar is proposed. As illustrated in *Figure 7. 6*, the main steps involved in the reforming process include the diffusion of tar molecules to internal catalytically active sites followed by the adsorption and decomposition of tar molecules (C_nH_m) over active sites. The O-containing functional groups in biochar would act as primary active sites, especially for the reforming of relatively large aromatic ring systems and non-oxygen-containing tar compounds. The overall

efficiency of this reforming process is related to the pore structure and the content of O-containing functional groups of biochar [13], with the latter being the dominant factor. The small and large tar molecules firstly diffuse into the internal surface of biochar through the micro- and mesopores in biochar.

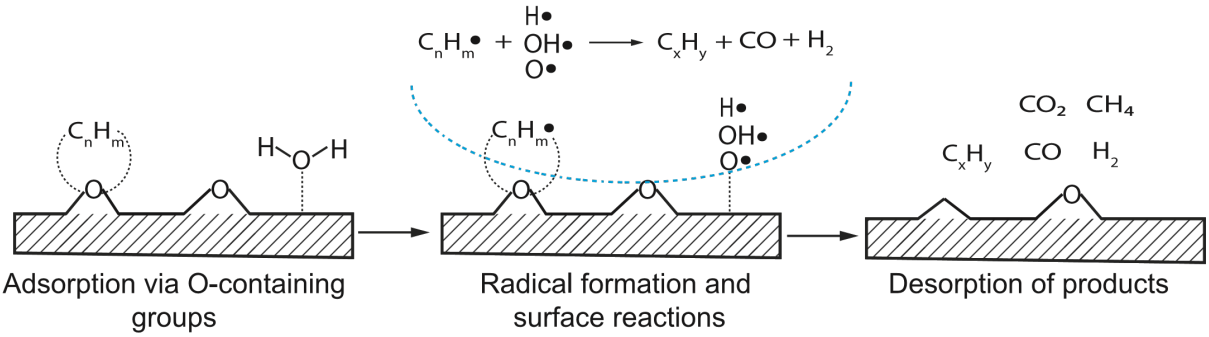

Figure 7. 6. Simplified mechanism of tar reforming via O-containing functional groups on biochar surface.

The tar molecules are then adsorbed on biochar surface via O-containing functional groups and dissociated into radicals. The formation of radicals is most likely to be the step in the mechanism that determines the reaction rate [3]. The presence of O-containing functional groups in biochar would facilitate the destabilisation of tar compounds, making them extremely active and easy to break into radicals. The breakdown of tar molecules is also associated with the structure of tar itself, where various tar structures would have different activation energies. The aromatics with more fused rings or penta-cycled rings/substituted groups tend to breakdown more easily as they are relatively active. In parallel to tar adsorption, H_2O present in the atmosphere is also adsorbed and dissociated on biochar, forming active radicals such as H, OH, and O, which could also react with each other.

The radicals from tar dissociation can react with the active radicals from H_2O to also form some small tar molecules (C_xH_y), as well as gases including CO and H_2, leading to the reforming/removal of tar compounds. Generated tar radicals could also react with each other to form larger tar molecules through polymerization and ultimately form coke. The presented H_2 in the system could also react with the tar radicals to form a stable tar molecule and a hydrogen radical. As a result, a certain concentration of small and stable PAHs (polycyclic aromatic hydrocarbons) such as naphthalene is observed. Therefore, the final tar composition

and the gas product distribution of tar reforming is the net result of all these parallel reactions that take place simultaneously in the reforming process.

As the complex reforming reaction proceeds, deactivation of a biochar catalyst will occur with the reduction of the O-containing functional groups. The binding between tar molecules and O-containing functional groups in biochar could also cause the O-containing functional groups to be decomposed with oxygen atoms being released from the biochar surface. Due to the lack of sufficient active sites at the late stage of reforming, the formation rate of tar radicals is significantly reduced, causing a decrease in the efficiency of tar removal. The mass loss of biochar caused by continuous gasification can lead to the reduction in the holding capacity of O-containing functional groups in biochar, resulting in the decrease of its the catalytic efficiency as well.

7.3 Conclusions

Mallee wood biochar was activated in situ by steam and then used as a catalyst for steam tar reforming at 800 °C. The gas composition, light tar composition, as well as the SSA and pore volume of biochar were comprehensively analysed. Results showed that the H_2/CO ratio increased after employing biochar as catalyst when compared with steam reforming without biochar. Steam activation of biochar greatly improved its catalytic activities in reforming of light tar compounds. The yields of these light tar compounds, especially the non-oxygen-containing compounds, increased with increasing reforming time. The SSA, micro- and mesopore volumes in biochar raised during steam activation while stayed almost unchanged during tar reforming. The developed micro- and mesopores in biochar would enhance the diffusion of both small and large tar molecules into the internal surface of biochar. The simultaneously generated O-containing functional groups during biochar activation are likely distributed in the newly created pores. Above all, it was found that the content of O-containing functional groups in biochar plays a more important role than the SSA and pore volume in determining its catalytic activity for tar reforming. Besides, the O-containing functional groups in biochar are likely to act as main active sites for the destruction of large aromatic ring systems and light non-oxygen-containing tar compounds. The O-containing

functional groups enhance the breakdown of tar molecules to form tar radicals, promoting the rate of tar removal.

7.5 References

[1] Li C-Z. Special issue—gasification: a route to clean energy. Process Saf Environ Prot 2006;84:407–8.

[2] Sikarwar VS, Zhao M, Clough P, Yao J, Zhong X, Memon MZ, Shah N, Anthony EJ, Fennell PS. An overview of advances in biomass gasification. Energy Environ Sci 2016;9:2939–77.

[3] Vreugdenhil BJ, Zwart RWR. Tar formation in pyrolysis and gasification, report (ECN-E--08-087), Energy Research Centre of the Netherlands (ECN) 2009.

[4] Abdoulmoumine N, Adhikari S, Kulkarni A, Chattanathan S. A review on biomass gasification syngas cleanup. Appl Energy 2015;155:294–307.

[5] Guan G, Kaewpanha M, Hao X, Abudula A. Catalytic steam reforming of biomass tar: Prospects and challenges. Renew Sustain Energy Rev 2016;58:450–61.

[6] Song Y, Wang Y, Hu X, Hu S, Xiang J, Zhang L, Zhang S, Min Z, Li C-Z. Effects of volatile-char interactions on in situ destruction of nascent tar during the pyrolysis and gasification of biomass. Part I. Roles of nascent char. Fuel 2014;122:60–6.

[7] Ravenni G, Sárossy Z, Ahrenfeldt J, Henriksen UB. Activity of chars and activated carbons for removal and decomposition of tar model compounds – A review. Renew Sustain Energy Rev 2018;94:1044–56.

[8] Min Z, Yimsiri P, Asadullah M, Zhang S, Li C-Z. Catalytic reforming of tar during gasification. Part II. Char as a catalyst or as a catalyst support for tar reforming. Fuel 2011;90:2545–52.

[9] Abu El-Rub Z, Bramer EA, Brem G. Experimental comparison of biomass chars with other catalysts for tar reduction. Fuel 2008;87:2243–52.

[10] Hosokai S, Kumabe K, Ohshita M, Norinaga K, Li C-Z, Hayashi J-I. Mechanism of decomposition of aromatics over charcoal and necessary condition for maintaining its activity. Fuel 2008;87:2914–22.

[11] Buentello-Montoya DAA, Zhang X, Li J. The use of gasification solid products as catalysts for tar reforming. Renew Sustain Energy Rev 2019;107:399–412.

[12] Liu Y, Paskevicius M, Wang H, Fushimi C, Parkinson G, Li C-Z. Difference in tar reforming activities between biochar catalysts activated in H_2O and CO_2. Fuel 2020;271:117636.

[13] Liu Y, Paskevicius M, Wang H, Parkinson G, Veder JP, Hu X, Li C-Z. Role of O-containing functional groups in biochar during the catalytic steam reforming of tar using the biochar as a catalyst. Fuel 2019;253:441–8.

[14] Nestler F, Burhenne L, Amtenbrink MJ, Aicher T. Catalytic decomposition of biomass tars: The impact of wood char surface characteristics on the catalytic performance for naphthalene removal. Fuel Process Technol 2016;145:31–41.

[15] Zhang S, Song Y, Song YC, Yi Q, Dong L, Li TT, Zhang L, Feng J, Li WY, Li C-Z. An advanced biomass gasification technology with integrated catalytic hot gas cleaning. Part III: Effects of inorganic species in char on the reforming of tars from wood and agricultural wastes. Fuel 2016;183:177–84.

[16] Song Y, Wang Y, Hu X, Xiang J, Hu S, Mourant D, Li T, Wu L, Li C-Z. Effects of volatile-char interactions on in-situ destruction of nascent tar during the pyrolysis and gasification of biomass. Part II. Roles of steam. Fuel 2015;143:555–62.

[17] Song Y, Zhao Y, Hu X, Zhang L, Sun S, Li C-Z. Destruction of tar during volatile-char interactions at low temperature. Fuel Process Technol 2018;171:215–22.

[18] Buentello-Montoya D, Zhang X, Marques S, Geron M. Investigation of competitive tar reforming using activated char as catalyst. Energy Procedia 2019;158:828–35.

[19] Milne TA, Evans RJ, Abatzaglou N. Biomass gasifier “tars”: their nature, formation, and conversion. technical report (NREL/TP-570-25357). National Energy Laboratory.The United states. 1998.

[20] Fuentes-Cano D, Gómez-Barea A, Nilsson S, Ollero P. Decomposition kinetics of model tar compounds over chars with different internal structure to model hot tar removal in biomass gasification. Chem Eng J 2013;228:1223–33.

[21] Hervy M, Weiss-Hortala E, Pham Minh D, Dib H, Villot A, Gérente C, Berhanu S,

Chesnaud A, Thorel A, Le Coq L, Nzihou A. Reactivity and deactivation mechanisms of pyrolysis chars from bio-waste during catalytic cracking of tar. Appl Energy 2019;237:487–99.

[22] Zhang S, Asadullah M, Dong L, Tay HL, Li C-Z. An advanced biomass gasification technology with integrated catalytic hot gas cleaning. Part II: Tar reforming using char as a catalyst or as a catalyst support. Fuel 2013;112:646–53.

[23] Wu H, Quyn DM, Li C-Z. Volatilisation and catalytic effects of alkali and alkaline earth metallic species during the pyrolysis and gasification of Victorian brown coal. Part III. The importance of the interactions between volatiles and char at high temperature. Fuel 2002;81:1033–9.

[24] Min Z, Yimsiri P, Zhang S, Wang Y, Asadullah M, Li C-Z. Catalytic reforming of tar during gasification. Part III. Effects of feedstock on tar reforming using ilmenite as a catalyst. Fuel 2013;103:950–5.

[25] Min Z, Asadullah M, Yimsiri P, Zhang S, Wu H, Li C-Z. Catalytic reforming of tar during gasification. Part I. Steam reforming of biomass tar using ilmenite as a catalyst. Fuel 2011;90:1847–54.

[26] Jiang S, Hu X, Xia D, Li C-Z. Formation of aromatic ring structures during the thermal treatment of mallee wood cylinders at low temperature. Appl Energy 2016;183:542–51.

[27] Akhtar MA, Zhang S, Shao X, Dang H, Liu Y, Li T, Zhang L, Li C-Z. Kinetic compensation effects in the chemical reaction-controlled regime and mass transfer-controlled regime during the gasification of biochar in O_2. Fuel Process Technol 2018;181:25–32.

[28] Wang Y, Hu X, Mourant D, Song Y, Zhang L, Lievens C, Xiang J, Li C-Z. Evolution of aromatic structures during the reforming of bio-oil: Importance of the interactions among bio-oil components. Fuel 2013;111:805–12.

[29] Wang Y, Li X, Mourant D, Gunawan R, Zhang S, Li C-Z. Formation of aromatic structures during the pyrolysis of bio-oil. Energy and Fuels 2012;26:241–7.

[30] Kirby NM, Mudie ST, Hawley AM, Cookson DJ, Mertens HDT, Cowieson N, Samardzic-Boban V. A low-background-intensity focusing small-angle X-ray scattering undulator beamline. J Appl Crystallogr 2013;46:1670–80.

[31] Liu Y, Paskevicius M, Sofianos MV, Parkinson G, Li C-Z. In situ SAXS studies of the pore

development in biochar during gasification. Carbon N Y 2021;172:454–62.

[32] Liu Y, Paskevicius M, Sofianos MV, Parkinson G, Wang S, Li C-Z. A SAXS study of the pore structure evolution in biochar during gasification in H_2O, CO_2 and H_2O/CO_2. Fuel 2021;292:120384.

[33] Dreiss CA, Jack KS, Parker AP. On the absolute calibration of bench-top small-angle X-ray scattering instruments: A comparison of different standard methods. J Appl Crystallogr 2006;39:32–8.

[34] Spalla O, Lyonnard S, Testard F. Analysis of the small-angle intensity scattered by a porous and granular medium. J Appl Crystallogr 2003;36:338–47.

[35] Beaucage G. Approximations leading to a unified exponential power-law approach to small-angle scattering. J Appl Crystallogr 1995;28:717–28.

[36] Ilavsky J, Jemian PR. Irena : tool suite for modeling and analysis of small-angle scattering. J Appl Crystallogr 2009;42:347–53.

[37] Hu M, Laghari M, Cui B, Xiao B, Zhang B, Guo D. Catalytic cracking of biomass tar over char supported nickel catalyst. Energy 2018;145:228–37.

[38] Jess A. Mechanisms and kinetics of thermal reactions of aromatic hydrocarbons from pyrolysis of solid fuels. Fuel 1996;75:1441–8.

[39] J.M.Thomas, W.J.Thomas. Principles and Practice of Heterogeneous Catalysis. Second. Wiley-VCH.

[40] Coetzee GH, Sakurovs R, Neomagus HWJP, Morpeth L, Everson RC, Mathews JP, Bunt JR. Pore development during gasification of South African inertinite-rich chars evaluated using small angle X-ray scattering. Carbon N Y 2015;95:250–60.

[41] Hosokai S, Norinaga K, Kimura T, Nakano M, Li C-Z, Hayashi J-I. Reforming of volatiles from the biomass pyrolysis over charcoal in a sequence of coke deposition and steam gasification of coke. Energy and Fuels 2011;25:5387–93.

Chapter 8

Conclusions and Recommendations

8.1 Conclusions

The first part (chapter 3 and 4) of this thesis was dedicated to the different evolution pathways of the pore structure in biochar during gasification in H_2O, CO_2 and H_2O/CO_2, to better understand the reaction mechanisms of biochar gasification. The second part (chapter 5, 6 and 7) systemically investigated the catalytic activities of biochar catalysts during tar reforming, aiming to gain insight into the mechanism of tar reforming using biochar as a catalyst. The main conclusions/findings of this study are summarised below.

8.1.1 Insights into the reaction mechanisms of biochar gasification.

- CO_2 tends to produce a highly microporous biochar but micropore enlargement is more remarkable during gasification in H_2O and H_2O/CO_2. Pore development in biochar during gasification in H_2O/CO_2 mixtures is similar to that in H_2O alone. This could be the result of the more dominant biocar-H_2O reaction than the biochar- CO_2 reaction.
- When gasified in H_2O and H_2O/CO_2, the pore structure of biochar evolved from a porous network of branched micropore clusters (pore fractal) to being dominated by rough surfaced mesopores (surface fractal). Whereas the CO_2 gasified biochar exhibited a pore fractal network on the mesopore size scale.
- The evolution of pore structures result from the different ways in which carbon atoms were removed by either H_2O or CO_2. H_2O is more reactive and less selective towards reacting with biochar, resulting in a less worm-like network of pores than CO_2. H_2O is more reactive and less selective towards reacting with biochar, resulting in a less sponge-like network of pores than CO_2.

- The pore development in various gasifying agents is paralleled by the evolution of the aromatic structures in biochar. The different pore structures produced by H_2O and CO_2 could also be attributed to the different amounts of O-containing groups.
- An increase in reaction temperature leads to faster rates of pore generation and pore enlargement due to the enhanced reaction rates and less selective removal of carbon atoms.
- Increasing reaction temperature reduced the differences in the pore structure between biochars gasified in H_2O and CO_2.
- Biomass particle size has little impact on the pore structure of biochar.

8.1.2 Insights into the mechanism of tar reforming employing biochar as a catalyst.

- H_2O activation enhanced the catalytic activity of biochar for the reforming of tar by increasing the concentration of O-containing functional groups, mainly the aromatic C-O structures in biochar.
- The O-containing functional groups in biochar are likely to act as the main active sites for the destruction of large aromatic ring systems and light non-oxygen-containing tar compounds.
- The O-containing functional groups would facilitate the dissociation of tar molecules to form tar radicals, which is most likely to be the rate-limiting step in the process of tar reforming over biochar catalysts.
- During the catalytic reforming of tar, O-containing groups in the biochar catalyst can be consumed, resulting in the decrease of the catalytic activity of biochar.
- The O-containing functional groups play a more important role than the pore volume in determining the catalytic activity of biochar.

- The catalytic activity of biochar can also be improved by CO_2 activation. However, CO_2-activated biochar showed lower catalytic activity than the H_2O-activaed in tar reforming both in the atmosphere of H_2O and CO_2. This could be attributed to the lower content of O-containing groups in CO_2-activated biochar.
- Under otherwise identical conditions, reforming in steam was always more rapid than that in CO_2 regardless of the atmosphere in which biochar was activated. The addition of excess H_2O during tar reforming can produce additional O-containing groups in biochar, improving and maintaining the catalytic activity of biochar.

8.2 Recommendations

This study of the pore structure development of biochar provides useful information for understanding the process of biomass gasification, which can facilitate the development of gasification technology, achieving highly efficient utilization of biomass. This would also be helpful in optimizing the properties of biochar for other applications. The study on tar reforming using biochar catalysts has identified the crucial role of O-containing functional groups in biochar for the destruction of tar, especially the large aromatic hydrocarbons and non-oxygen-containing light tar compounds. Despite the positive outcome of this study, further work could be done to gain further insight and to promote the development of gasification technologies. The following research paths are suggested:

1. Pore development was characterized *in situ* in the process of gasification. The *in situ* changes in the chemical structure of biochar would provide valuable information regarding the carbon sites that is preferably attached by H_2O or CO_2. Therefore, *in situ* characterization of the chemical structure of biochar should be undertaken to better understand the reaction pathways of biochar gasification. For example, using *in situ* Raman spectroscopy to examine the evolution of the carbon structure of biochar during gasification.

2. The critical role of O-containing functional groups in biochar for tar reforming has been identified in this study. Apart from acting as intermediates, those functional groups also affect the surface chemistry of biochar. During gasification and/or tar reforming, O-containing functional groups decomposed to release CO_2, CO and H_2O. Real-time monitoring the release of gases using temperature-programmed desorption (TPD) could further provide helpful information in understanding the stability and reactivity of various O-containing functional groups.
3. There could be different types of active sites in biochar on which various tar compounds are preferably adsorbed and destructed. Additionally, these different active sites could interact with each other and act in conjunction to promote tar reforming. Therefore, studies are required to further understand the catalytic behaviour of biochar catalysts.
4. Most of the studies on biochar catalysts were conducted using bench-scale micro reactors. It is a demanding task to perform more trials in industrial plants so as to assess the performance and practical feasibility of biochar. Which could also facilitate the design of gasifier that integrates with hot gas cleaning employing the biochar produced inside the reactor. Besides, the consumption of char-based catalysts through gasification during tar reforming is inevitable. Thus, the easy refill and regeneration of char-based catalysts should be taken into consideration when developing novel gasification technology.
5. To increase the economic efficiency of gasification technology, the alternative uses of residual biochar for the production of innovative carbon-based materials could be explored.
6. Biomass gasification is a mature technology that can act as a viable pathway for cost-competitive hydrogen production. More work can be done to modify the experimental conditions for hot gas cleaning, aiming to convert tar compounds into more hydrogen in the produced gas stream.

Appendix I

Permission of Reproduction from the Copyright Owner

In situ SAXS studies of the pore development in biochar during gasification

Author: Yurong Liu,Mark Paskevicius,M. Veronica Sofianos,Gordon Parkinson,Chun-Zhu Li

Publication: Carbon

Publisher: Elsevier

Date: February 2021

A SAXS study of the pore structure evolution in biochar during gasification in H2O, CO2 and H2O/CO2

Author:
Yurong Liu,Mark Paskevicius,M. Veronica Sofianos,Gordon Parkinson,Shuai Wang,Chun-Zhu Li

Publication: Fuel
Publisher: Elsevier
Date: 15 May 2021

Role of O-containing functional groups in biochar during the catalytic steam reforming of tar using the biochar as a catalyst

Author:
Yurong Liu,Mark Paskevicius,Hongqi Wang,Gordon Parkinson,Jean-Pierre Veder,Xun Hu,Chun-Zhu Li

Publication: Fuel
Publisher: Elsevier
Date: 1 October 2019

Difference in tar reforming activities between biochar catalysts activated in H2O and CO2

Author:
Yurong Liu,Mark Paskevicius,Hongqi Wang,Chihiro Fushimi,Gordon Parkinson,Chun-Zhu Li

Publication: Fuel
Publisher: Elsevier
Date: 1 July 2020

Insights into the mechanism of tar reforming using biochar as a catalyst

Author:
Yurong Liu,Mark Paskevicius,Hongqi Wang,Gordon Parkinson,Juntao Wei,Muhammad Asif Akhtar,Chun-Zhu Li

Publication: Fuel

Publisher: Elsevier

Date: 15 July 2021

ELSEVIER LICENSE
TERMS AND CONDITIONS

Mar 31, 2021

This Agreement between Curtin University -- Yurong Liu ("You") and Elsevier ("Elsevier") consists of your license details and the terms and conditions provided by Elsevier and Copyright Clearance Center.

License Number	5039210891979
License date	Mar 31, 2021
Licensed Content Publisher	Elsevier
Licensed Content Publication	Fuel
Licensed Content Title	Importance of volatile–char interactions during the pyrolysis and gasification of low-rank fuels – A review
Licensed Content Author	Chun-Zhu Li
Licensed Content Date	Oct 1, 2013
Licensed Content Volume	112
Licensed Content Issue	n/a
Licensed Content Pages	15
Start Page	609
End Page	623
Type of Use	reuse in a thesis/dissertation

Portion	figures/tables/illustrations
Number of figures/tables/illustrations	1
Format	both print and electronic
Are you the author of this Elsevier article?	No
Will you be translating?	No
Title	Reaction Mechanisms of Biochar Gasification and Tar Reforming
Institution name	Curtin University
Expected presentation date	Apr 2021
Portions	Fig. 1. Gasification as the core of many versatile near-zero emission energy technologies.
Requestor Location	Curtin University 166B Hillview terrace Perth, WA 6102 Australia Attn: Curtin University
Publisher Tax ID	GB 494 6272 12
Total	0.00 AUD

Terms and Conditions

INTRODUCTION

1. The publisher for this copyrighted material is Elsevier. By clicking "accept" in connection with completing this licensing transaction, you agree that the following terms and conditions apply to this transaction (along with the Billing and Payment terms and conditions established by Copyright Clearance Center, Inc. ("CCC"), at the time that you opened your Rightslink account and that are available at any time at http://myaccount.copyright.com).

GENERAL TERMS

2. Elsevier hereby grants you permission to reproduce the aforementioned material subject to the terms and conditions indicated.

3. Acknowledgement: If any part of the material to be used (for example, figures) has appeared in our publication with credit or acknowledgement to another source, permission must also be sought from that source. If such permission is not obtained then that material may not be included in your publication/copies. Suitable acknowledgement to the source must be made, either as a footnote or in a reference list at the end of your publication, as follows:

"Reprinted from Publication title, Vol /edition number, Author(s), Title of article / title of chapter, Pages No., Copyright (Year), with permission from Elsevier [OR APPLICABLE SOCIETY COPYRIGHT OWNER]." Also Lancet special credit - "Reprinted from The Lancet, Vol. number, Author(s), Title of article, Pages No., Copyright (Year), with permission from Elsevier."

4. Reproduction of this material is confined to the purpose and/or media for which permission is hereby given.

5. Altering/Modifying Material: Not Permitted. However figures and illustrations may be altered/adapted minimally to serve your work. Any other abbreviations, additions, deletions and/or any other alterations shall be made only with prior written authorization of Elsevier Ltd. (Please contact Elsevier's permissions helpdesk here). No modifications can be made to any Lancet figures/tables and they must be reproduced in full.

6. If the permission fee for the requested use of our material is waived in this instance, please be advised that your future requests for Elsevier materials may attract a fee.

7. Reservation of Rights: Publisher reserves all rights not specifically granted in the combination of (i) the license details provided by you and accepted in the course of this licensing transaction, (ii) these terms and conditions and (iii) CCC's Billing and Payment terms and conditions.

8. License Contingent Upon Payment: While you may exercise the rights licensed immediately upon issuance of the license at the end of the licensing process for the transaction, provided that you have disclosed complete and accurate details of your proposed use, no license is finally effective unless and until full payment is received from you (either by publisher or by CCC) as provided in CCC's Billing and Payment terms and conditions. If full payment is not received on a timely basis, then any license preliminarily granted shall be deemed automatically revoked and shall be void as if never granted. Further, in the event that you breach any of these terms and conditions or any of CCC's Billing and Payment terms and conditions, the license is automatically revoked and shall be void as if never granted. Use of materials as described in a revoked license, as well as any use of the materials beyond the scope of an unrevoked license, may constitute copyright infringement and publisher reserves the right to take any and all action to protect its copyright in the materials.

9. Warranties: Publisher makes no representations or warranties with respect to the licensed material.

10. Indemnity: You hereby indemnify and agree to hold harmless publisher and CCC, and their respective officers, directors, employees and agents, from and against any and all claims arising out of your use of the licensed material other than as specifically authorized pursuant to this license.

11. No Transfer of License: This license is personal to you and may not be sublicensed, assigned, or transferred by you to any other person without publisher's written permission.

12. No Amendment Except in Writing: This license may not be amended except in a writing signed by both parties (or, in the case of publisher, by CCC on publisher's behalf).

13. Objection to Contrary Terms: Publisher hereby objects to any terms contained in any purchase order, acknowledgment, check endorsement or other writing prepared by you, which terms are inconsistent with these terms and conditions or CCC's Billing and Payment terms and conditions. These terms and conditions, together with CCC's Billing and Payment terms and conditions (which are incorporated herein), comprise the entire agreement between you and publisher (and CCC) concerning this licensing transaction. In the event of any conflict between your obligations established by these terms and conditions and those established by CCC's Billing and Payment terms and conditions, these terms and conditions shall control.

14. Revocation: Elsevier or Copyright Clearance Center may deny the permissions described in this License at their sole discretion, for any reason or no reason, with a full refund payable to you. Notice of such denial will be made using the contact information provided by you. Failure to receive such notice will not alter or invalidate the denial. In no event will Elsevier or Copyright Clearance Center be responsible or liable for any costs, expenses or damage incurred by you as a result of a denial of your permission request, other than a refund of the amount(s) paid by you to Elsevier and/or Copyright Clearance Center for denied permissions.

LIMITED LICENSE

The following terms and conditions apply only to specific license types:

15. **Translation**: This permission is granted for non-exclusive world **English** rights only unless your license was granted for translation rights. If you licensed translation rights you may only translate this content into the languages you requested. A professional translator must perform all translations and reproduce the content word for word preserving the integrity of the article.

16. **Posting licensed content on any Website**: The following terms and conditions apply as follows: Licensing material from an Elsevier journal: All content posted to the web site must maintain the copyright information line on the bottom of each image; A hyper-text must be included to the Homepage of the journal from which you are licensing at http://www.sciencedirect.com/science/journal/xxxxx or the Elsevier homepage for books at http://www.elsevier.com; Central Storage: This license does not include permission for a scanned version of the material to be stored in a central repository such as that provided by Heron/XanEdu.

Licensing material from an Elsevier book: A hyper-text link must be included to the Elsevier homepage at http://www.elsevier.com . All content posted to the web site must maintain the copyright information line on the bottom of each image.

Posting licensed content on Electronic reserve: In addition to the above the following clauses are applicable: The web site must be password-protected and made available only to bona fide students registered on a relevant course. This permission is granted for 1 year only. You may obtain a new license for future website posting.

17. **For journal authors:** the following clauses are applicable in addition to the above:

Preprints:

A preprint is an author's own write-up of research results and analysis, it has not been peer-reviewed, nor has it had any other value added to it by a publisher (such as formatting, copyright, technical enhancement etc.).

Authors can share their preprints anywhere at any time. Preprints should not be added to or enhanced in any way in order to appear more like, or to substitute for, the final versions of articles however authors can update their preprints on arXiv or RePEc with their Accepted Author Manuscript (see below).

If accepted for publication, we encourage authors to link from the preprint to their formal publication via its DOI. Millions of researchers have access to the formal publications on ScienceDirect, and so links will help users to find, access, cite and use the best available version. Please note that Cell Press, The Lancet and some society-owned have different preprint policies. Information on these policies is available on the journal homepage.

Accepted Author Manuscripts: An accepted author manuscript is the manuscript of an article that has been accepted for publication and which typically includes author-incorporated changes suggested during submission, peer review and editor-author communications.

Authors can share their accepted author manuscript:

- immediately
    - via their non-commercial person homepage or blog
    - by updating a preprint in arXiv or RePEc with the accepted manuscript
    - via their research institute or institutional repository for internal institutional uses or as part of an invitation-only research collaboration work-group
    - directly by providing copies to their students or to research collaborators for their personal use
    - for private scholarly sharing as part of an invitation-only work group on commercial sites with which Elsevier has an agreement
- After the embargo period
    - via non-commercial hosting platforms such as their institutional repository
    - via commercial sites with which Elsevier has an agreement

In all cases accepted manuscripts should:

- link to the formal publication via its DOI
- bear a CC-BY-NC-ND license - this is easy to do
- if aggregated with other manuscripts, for example in a repository or other site, be shared in alignment with our hosting policy not be added to or enhanced in any way to appear more like, or to substitute for, the published journal article.

Published journal article (JPA): A published journal article (PJA) is the definitive final record of published research that appears or will appear in the journal and embodies all value-adding publishing activities including peer review co-ordination, copy-editing, formatting, (if relevant) pagination and online enrichment.

Policies for sharing publishing journal articles differ for subscription and gold open access articles:

Subscription Articles: If you are an author, please share a link to your article rather than the full-text. Millions of researchers have access to the formal publications on ScienceDirect, and so links will help your users to find, access, cite, and use the best available version.

Theses and dissertations which contain embedded PJAs as part of the formal submission can be posted publicly by the awarding institution with DOI links back to the formal publications on ScienceDirect.

If you are affiliated with a library that subscribes to ScienceDirect you have additional private sharing rights for others' research accessed under that agreement. This includes use for classroom teaching and internal training at the institution (including use in course packs and courseware programs), and inclusion of the article for grant funding purposes.

Gold Open Access Articles: May be shared according to the author-selected end-user license and should contain a CrossMark logo, the end user license, and a DOI link to the formal publication on ScienceDirect.

Please refer to Elsevier's posting policy for further information.

18. **For book authors** the following clauses are applicable in addition to the above: Authors are permitted to place a brief summary of their work online only. You are not allowed to download and post the published electronic version of your chapter, nor may you scan the printed edition to create an electronic version. **Posting to a repository:** Authors are permitted to post a summary of their chapter only in their institution's repository.

19. **Thesis/Dissertation**: If your license is for use in a thesis/dissertation your thesis may be submitted to your institution in either print or electronic form. Should your thesis be published commercially, please reapply for permission. These requirements include permission for the Library and Archives of Canada to supply single copies, on demand, of the complete thesis and include permission for Proquest/UMI to supply single copies, on demand, of the complete thesis. Should your thesis be published commercially, please reapply for permission. Theses and dissertations which contain embedded PJAs as part of the formal submission can be posted publicly by the awarding institution with DOI links back to the formal publications on ScienceDirect.

Elsevier Open Access Terms and Conditions

You can publish open access with Elsevier in hundreds of open access journals or in nearly 2000 established subscription journals that support open access publishing. Permitted third party re-use of these open access articles is defined by the author's choice of Creative Commons user license. See our open access license policy for more information.

Terms & Conditions applicable to all Open Access articles published with Elsevier:

Any reuse of the article must not represent the author as endorsing the adaptation of the article nor should the article be modified in such a way as to damage the author's honour or reputation. If any changes have been made, such changes must be clearly indicated.

The author(s) must be appropriately credited and we ask that you include the end user license and a DOI link to the formal publication on ScienceDirect.

If any part of the material to be used (for example, figures) has appeared in our publication with credit or acknowledgement to another source it is the responsibility of the user to ensure their reuse complies with the terms and conditions determined by the rights holder.

Additional Terms & Conditions applicable to each Creative Commons user license:

CC BY: The CC-BY license allows users to copy, to create extracts, abstracts and new works from the Article, to alter and revise the Article and to make commercial use of the Article (including reuse and/or resale of the Article by commercial entities), provided the user gives appropriate credit (with a link to the formal publication through the relevant DOI), provides a link to the license, indicates if changes were made and the licensor is not represented as endorsing the use made of the work. The full details of the license are available at http://creativecommons.org/licenses/by/4.0.

CC BY NC SA: The CC BY-NC-SA license allows users to copy, to create extracts, abstracts and new works from the Article, to alter and revise the Article, provided this is not done for commercial purposes, and that the user gives appropriate credit (with a link to the formal publication through the relevant DOI), provides a link to the license, indicates if changes were made and the licensor is not represented as endorsing the use made of the

work. Further, any new works must be made available on the same conditions. The full details of the license are available at http://creativecommons.org/licenses/by-nc-sa/4.0.

CC BY NC ND: The CC BY-NC-ND license allows users to copy and distribute the Article, provided this is not done for commercial purposes and further does not permit distribution of the Article if it is changed or edited in any way, and provided the user gives appropriate credit (with a link to the formal publication through the relevant DOI), provides a link to the license, and that the licensor is not represented as endorsing the use made of the work. The full details of the license are available at http://creativecommons.org/licenses/by-nc-nd/4.0. Any commercial reuse of Open Access articles published with a CC BY NC SA or CC BY NC ND license requires permission from Elsevier and will be subject to a fee.

Commercial reuse includes:

- Associating advertising with the full text of the Article
- Charging fees for document delivery or access
- Article aggregation
- Systematic distribution via e-mail lists or share buttons

Posting or linking by commercial companies for use by customers of those companies.

20. **Other Conditions**:

v1.10

Questions? customercare@copyright.com or +1-855-239-3415 (toll free in the US) or +1-978-646-2777.

ELSEVIER LICENSE
TERMS AND CONDITIONS

Mar 31, 2021

This Agreement between Curtin University -- Yurong Liu ("You") and Elsevier ("Elsevier") consists of your license details and the terms and conditions provided by Elsevier and Copyright Clearance Center.

License Number	5039211099034
License date	Mar 31, 2021
Licensed Content Publisher	Elsevier
Licensed Content Publication	Fuel
Licensed Content Title	Volatilisation and catalytic effects of alkali and alkaline earth metallic species during the pyrolysis and gasification of Victorian brown coal. Part III. The importance of the interactions between volatiles and char at high temperature
Licensed Content Author	Hongwei Wu,Dimple M. Quyn,Chun-Zhu Li
Licensed Content Date	May 1, 2002
Licensed Content Volume	81
Licensed Content Issue	8
Licensed Content Pages	7
Start Page	1033
End Page	1039
Type of Use	reuse in a thesis/dissertation

Portion	figures/tables/illustrations
Number of figures/tables/illustrations	1
Format	both print and electronic
Are you the author of this Elsevier article?	No
Will you be translating?	No
Title	Reaction Mechanisms of Biochar Gasification and Tar Reforming
Institution name	Curtin University
Expected presentation date	Apr 2021
Portions	Fig. 1. A schematic diagram of the two-stage quartz reactor
Requestor Location	Curtin University 166B Hillview terrace Perth, WA 6102 Australia Attn: Curtin University
Publisher Tax ID	GB 494 6272 12
Total	0.00 AUD
Terms and Conditions	

INTRODUCTION

1. The publisher for this copyrighted material is Elsevier. By clicking "accept" in connection with completing this licensing transaction, you agree that the following terms and conditions apply to this transaction (along with the Billing and Payment terms and conditions established by Copyright Clearance Center, Inc. ("CCC"), at the time that you opened your Rightslink account and that are available at any time at http://myaccount.copyright.com).

GENERAL TERMS

2. Elsevier hereby grants you permission to reproduce the aforementioned material subject to the terms and conditions indicated.

3. Acknowledgement: If any part of the material to be used (for example, figures) has appeared in our publication with credit or acknowledgement to another source, permission must also be sought from that source. If such permission is not obtained then that material may not be included in your publication/copies. Suitable acknowledgement to the source must be made, either as a footnote or in a reference list at the end of your publication, as follows:

"Reprinted from Publication title, Vol /edition number, Author(s), Title of article / title of chapter, Pages No., Copyright (Year), with permission from Elsevier [OR APPLICABLE SOCIETY COPYRIGHT OWNER]." Also Lancet special credit - "Reprinted from The Lancet, Vol. number, Author(s), Title of article, Pages No., Copyright (Year), with permission from Elsevier."

4. Reproduction of this material is confined to the purpose and/or media for which permission is hereby given.

5. Altering/Modifying Material: Not Permitted. However figures and illustrations may be altered/adapted minimally to serve your work. Any other abbreviations, additions, deletions and/or any other alterations shall be made only with prior written authorization of Elsevier Ltd. (Please contact Elsevier's permissions helpdesk here). No modifications can be made to any Lancet figures/tables and they must be reproduced in full.

6. If the permission fee for the requested use of our material is waived in this instance, please be advised that your future requests for Elsevier materials may attract a fee.

7. Reservation of Rights: Publisher reserves all rights not specifically granted in the combination of (i) the license details provided by you and accepted in the course of this licensing transaction, (ii) these terms and conditions and (iii) CCC's Billing and Payment terms and conditions.

8. License Contingent Upon Payment: While you may exercise the rights licensed immediately upon issuance of the license at the end of the licensing process for the transaction, provided that you have disclosed complete and accurate details of your proposed use, no license is finally effective unless and until full payment is received from you (either by publisher or by CCC) as provided in CCC's Billing and Payment terms and conditions. If full payment is not received on a timely basis, then any license preliminarily granted shall be deemed automatically revoked and shall be void as if never granted. Further, in the event that you breach any of these terms and conditions or any of CCC's Billing and Payment terms and conditions, the license is automatically revoked and shall be void as if never granted. Use of materials as described in a revoked license, as well as any use of the materials beyond the scope of an unrevoked license, may constitute copyright infringement and publisher reserves the right to take any and all action to protect its copyright in the materials.

9. Warranties: Publisher makes no representations or warranties with respect to the licensed material.

10. Indemnity: You hereby indemnify and agree to hold harmless publisher and CCC, and their respective officers, directors, employees and agents, from and against any and all claims arising out of your use of the licensed material other than as specifically authorized pursuant to this license.

11. No Transfer of License: This license is personal to you and may not be sublicensed, assigned, or transferred by you to any other person without publisher's written permission.

12. No Amendment Except in Writing: This license may not be amended except in a writing signed by both parties (or, in the case of publisher, by CCC on publisher's behalf).

13. Objection to Contrary Terms: Publisher hereby objects to any terms contained in any purchase order, acknowledgment, check endorsement or other writing prepared by you, which terms are inconsistent with these terms and conditions or CCC's Billing and Payment terms and conditions. These terms and conditions, together with CCC's Billing and Payment terms and conditions (which are incorporated herein), comprise the entire agreement between you and publisher (and CCC) concerning this licensing transaction. In the event of any conflict between your obligations established by these terms and conditions and those established by CCC's Billing and Payment terms and conditions, these terms and conditions shall control.

14. Revocation: Elsevier or Copyright Clearance Center may deny the permissions described in this License at their sole discretion, for any reason or no reason, with a full refund payable to you. Notice of such denial will be made using the contact information provided by you. Failure to receive such notice will not alter or invalidate the denial. In no event will Elsevier or Copyright Clearance Center be responsible or liable for any costs, expenses or damage incurred by you as a result of a denial of your permission request, other than a refund of the amount(s) paid by you to Elsevier and/or Copyright Clearance Center for denied permissions.

LIMITED LICENSE

The following terms and conditions apply only to specific license types:

15. **Translation**: This permission is granted for non-exclusive world **English** rights only unless your license was granted for translation rights. If you licensed translation rights you may only translate this content into the languages you requested. A professional translator must perform all translations and reproduce the content word for word preserving the integrity of the article.

16. **Posting licensed content on any Website**: The following terms and conditions apply as follows: Licensing material from an Elsevier journal: All content posted to the web site must maintain the copyright information line on the bottom of each image; A hyper-text must be included to the Homepage of the journal from which you are licensing at http://www.sciencedirect.com/science/journal/xxxxx or the Elsevier homepage for books at http://www.elsevier.com; Central Storage: This license does not include permission for a scanned version of the material to be stored in a central repository such as that provided by Heron/XanEdu.

Licensing material from an Elsevier book: A hyper-text link must be included to the Elsevier homepage at http://www.elsevier.com . All content posted to the web site must maintain the copyright information line on the bottom of each image.

Posting licensed content on Electronic reserve: In addition to the above the following clauses are applicable: The web site must be password-protected and made available only to bona fide students registered on a relevant course. This permission is granted for 1 year only. You may obtain a new license for future website posting.

17. **For journal authors:** the following clauses are applicable in addition to the above:

Preprints:

A preprint is an author's own write-up of research results and analysis, it has not been peer-reviewed, nor has it had any other value added to it by a publisher (such as formatting, copyright, technical enhancement etc.).

Authors can share their preprints anywhere at any time. Preprints should not be added to or enhanced in any way in order to appear more like, or to substitute for, the final versions of articles however authors can update their preprints on arXiv or RePEc with their Accepted Author Manuscript (see below).

If accepted for publication, we encourage authors to link from the preprint to their formal publication via its DOI. Millions of researchers have access to the formal publications on ScienceDirect, and so links will help users to find, access, cite and use the best available version. Please note that Cell Press, The Lancet and some society-owned have different preprint policies. Information on these policies is available on the journal homepage.

Accepted Author Manuscripts: An accepted author manuscript is the manuscript of an article that has been accepted for publication and which typically includes author-incorporated changes suggested during submission, peer review and editor-author communications.

Authors can share their accepted author manuscript:

- immediately
    - via their non-commercial person homepage or blog
    - by updating a preprint in arXiv or RePEc with the accepted manuscript
    - via their research institute or institutional repository for internal institutional uses or as part of an invitation-only research collaboration work-group
    - directly by providing copies to their students or to research collaborators for their personal use
    - for private scholarly sharing as part of an invitation-only work group on commercial sites with which Elsevier has an agreement
- After the embargo period
    - via non-commercial hosting platforms such as their institutional repository
    - via commercial sites with which Elsevier has an agreement

In all cases accepted manuscripts should:

- link to the formal publication via its DOI
- bear a CC-BY-NC-ND license - this is easy to do
- if aggregated with other manuscripts, for example in a repository or other site, be shared in alignment with our hosting policy not be added to or enhanced in any way to appear more like, or to substitute for, the published journal article.

Published journal article (JPA): A published journal article (PJA) is the definitive final record of published research that appears or will appear in the journal and embodies all value-adding publishing activities including peer review co-ordination, copy-editing, formatting, (if relevant) pagination and online enrichment.

Policies for sharing publishing journal articles differ for subscription and gold open access articles:

Subscription Articles: If you are an author, please share a link to your article rather than the full-text. Millions of researchers have access to the formal publications on ScienceDirect, and so links will help your users to find, access, cite, and use the best available version.

Theses and dissertations which contain embedded PJAs as part of the formal submission can be posted publicly by the awarding institution with DOI links back to the formal publications on ScienceDirect.

If you are affiliated with a library that subscribes to ScienceDirect you have additional private sharing rights for others' research accessed under that agreement. This includes use for classroom teaching and internal training at the institution (including use in course packs and courseware programs), and inclusion of the article for grant funding purposes.

Gold Open Access Articles: May be shared according to the author-selected end-user license and should contain a CrossMark logo, the end user license, and a DOI link to the formal publication on ScienceDirect.

Please refer to Elsevier's posting policy for further information.

18. **For book authors** the following clauses are applicable in addition to the above: Authors are permitted to place a brief summary of their work online only. You are not allowed to download and post the published electronic version of your chapter, nor may you scan the printed edition to create an electronic version. **Posting to a repository:** Authors are permitted to post a summary of their chapter only in their institution's repository.

19. **Thesis/Dissertation**: If your license is for use in a thesis/dissertation your thesis may be submitted to your institution in either print or electronic form. Should your thesis be published commercially, please reapply for permission. These requirements include permission for the Library and Archives of Canada to supply single copies, on demand, of the complete thesis and include permission for Proquest/UMI to supply single copies, on demand, of the complete thesis. Should your thesis be published commercially, please reapply for permission. Theses and dissertations which contain embedded PJAs as part of the formal submission can be posted publicly by the awarding institution with DOI links back to the formal publications on ScienceDirect.

Elsevier Open Access Terms and Conditions

You can publish open access with Elsevier in hundreds of open access journals or in nearly 2000 established subscription journals that support open access publishing. Permitted third party re-use of these open access articles is defined by the author's choice of Creative Commons user license. See our open access license policy for more information.

Terms & Conditions applicable to all Open Access articles published with Elsevier:

Any reuse of the article must not represent the author as endorsing the adaptation of the article nor should the article be modified in such a way as to damage the author's honour or reputation. If any changes have been made, such changes must be clearly indicated.

The author(s) must be appropriately credited and we ask that you include the end user license and a DOI link to the formal publication on ScienceDirect.

If any part of the material to be used (for example, figures) has appeared in our publication with credit or acknowledgement to another source it is the responsibility of the user to ensure their reuse complies with the terms and conditions determined by the rights holder.

Additional Terms & Conditions applicable to each Creative Commons user license:

CC BY: The CC-BY license allows users to copy, to create extracts, abstracts and new works from the Article, to alter and revise the Article and to make commercial use of the Article (including reuse and/or resale of the Article by commercial entities), provided the user gives appropriate credit (with a link to the formal publication through the relevant DOI), provides a link to the license, indicates if changes were made and the licensor is not represented as endorsing the use made of the work. The full details of the license are available at http://creativecommons.org/licenses/by/4.0.

CC BY NC SA: The CC BY-NC-SA license allows users to copy, to create extracts, abstracts and new works from the Article, to alter and revise the Article, provided this is not done for commercial purposes, and that the user gives appropriate credit (with a link to the formal publication through the relevant DOI), provides a link to the license, indicates if changes were made and the licensor is not represented as endorsing the use made of the

work. Further, any new works must be made available on the same conditions. The full details of the license are available at http://creativecommons.org/licenses/by-nc-sa/4.0.

CC BY NC ND: The CC BY-NC-ND license allows users to copy and distribute the Article, provided this is not done for commercial purposes and further does not permit distribution of the Article if it is changed or edited in any way, and provided the user gives appropriate credit (with a link to the formal publication through the relevant DOI), provides a link to the license, and that the licensor is not represented as endorsing the use made of the work. The full details of the license are available at http://creativecommons.org/licenses/by-nc-nd/4.0. Any commercial reuse of Open Access articles published with a CC BY NC SA or CC BY NC ND license requires permission from Elsevier and will be subject to a fee.

Commercial reuse includes:

- Associating advertising with the full text of the Article
- Charging fees for document delivery or access
- Article aggregation
- Systematic distribution via e-mail lists or share buttons

Posting or linking by commercial companies for use by customers of those companies.

20. **Other Conditions**:

v1.10

Questions? customercare@copyright.com or +1-855-239-3415 (toll free in the US) or +1-978-646-2777.

Appendix II

Co-author Attribution Statement

Chapter 3. Paper “Liu Y, Paskevicius M, Sofianos MV, Parkinson G, Li C-Z. In situ SAXS studies of the pore development in biochar during gasification”. Carbon N Y 2020;172.

	Conception & design	Experiments conduction & data acquisition	Data processing & analysis	Interpretation & discussion	Manuscript writing, revision & finalisation	Final approval
Yurong Liu	x	x	x	x	x	x
I acknowledge that these represent my contribution to the above result output. Signed:						
Mark Paskevicius	x	x	x	x	x	x
I acknowledge that these represent my contribution to the above result output. Signed:						
M. Veronica Sofiano		x			x	x
I acknowledge that these represent my contribution to the above result output. Signed:						
Gordon Parkinson	x			x	x	x
I acknowledge that these represent my contribution to the above result output. Signed:						
Chun-Zhu Li	x		x	x	x	x
I acknowledge that these represent my contribution to the above result output. Signed:						

Chapter 4. Paper "Liu Y, Paskevicius M, Sofianos MV, Parkinson G, Wang S, Li C-Z. "A SAXS study of the pore structure evolution in biochar during gasification in H_2O, CO_2 and H_2O/CO_2". Fuel. 292 (2021) 120384.

	Conception & design	Experiments conduction & data acquisition	Data processing & analysis	Interpretation & discussion	Manuscript writing, revision & finalisation	Final approval
Yurong Liu	x	x	x	x	x	x
I acknowledge that these represent my contribution to the above result output. Signed:						
Mark Paskevicius	x	x	x	x	x	x
I acknowledge that these represent my contribution to the above result output. Signed:						
M. Veronica Sofiano		x			x	x
I acknowledge that these represent my contribution to the above result output. Signed:						
Gordon Parkinson	x			x	x	x
I acknowledge that these represent my contribution to the above result output. Signed:						
Shuai Wang		x				x
I acknowledge that these represent my contribution to the above result output. Signed:						
Chun-Zhu Li	x		x	x	x	x
I acknowledge that these represent my contribution to the above result output. Signed:						

Chapter 5. Paper ”Liu Y, Paskevicius M, Wang H, Parkinson G, Veder JP, Hu X, Li C-Z. Role of O-containing functional groups in biochar during the catalytic steam reforming of tar using the biochar as a catalyst”. Fuel 2019;253:441–8.

	Conception & design	Experiments conduction & data acquisition	Data processing & analysis	Interpretation & discussion	Manuscript writing, revision & finalisation	Final approval
Yurong Liu	x	x	x	x	x	x
I acknowledge that these represent my contribution to the above result output. Signed:						
Mark Paskevicius				x	x	x
I acknowledge that these represent my contribution to the above result output. Signed:						
Hongqi Wang		x				x
I acknowledge that these represent my contribution to the above result output. Signed:						
Gordon Parkinson	x			x	x	x
I acknowledge that these represent my contribution to the above result output. Signed:						
Jean-Pierre Veder		x				x
I acknowledge that these represent my contribution to the above result output. Signed:						
Xun Hu					x	x
I acknowledge that these represent my contribution to the above result output. Signed:						
Chun-Zhu Li	x		x	x	x	x
I acknowledge that these represent my contribution to the above result output. Signed:						

Chapter 6. Paper "Liu Y, Paskevicius M, Wang H, Fushimi C, Parkinson G, Li C-Z. Difference in tar reforming activities between biochar catalysts activated in H_2O and CO_2". Fuel 2020;271:117636.

	Conception & design	Experiments conduction & data acquisition	Data processing & analysis	Interpretation & discussion	Manuscript writing, revision & finalisation	Final approval
Yurong Liu	x	x	x	x	x	x
I acknowledge that these represent my contribution to the above result output. Signed:						
Mark Paskevicius	x			x	x	x
I acknowledge that these represent my contribution to the above result output. Signed:						
Hongqi Wang		x				x
I acknowledge that these represent my contribution to the above result output. Signed:						
Chihiro Fushimi					x	x
I acknowledge that these represent my contribution to the above result output. Signed:						
Gordon Parkinson	x			x	x	x
I acknowledge that these represent my contribution to the above result output. Signed:						
Chun-Zhu Li	x		x	x	x	x
I acknowledge that these represent my contribution to the above result output. Signed:						

Chapter 7. Paper "Liu Y, Paskevicius M, Wang H, Parkinson G, Wei J, Akhtar M.A, Li C-Z. "Insights into the mechanism of tar reforming using biochar as a catalyst". Fuel. 296 (2021) 120672.

	Conception & design	Experiments conduction & data acquisition	Data processing & analysis	Interpretation & discussion	Manuscript writing, revision & finalisation	Final approval
Yurong Liu	x	x	x	x	x	x
I acknowledge that these represent my contribution to the above result output. Signed:						
Mark Paskevicius	x		x	x	x	x
I acknowledge that these represent my contribution to the above result output. Signed:						
Hongqi Wang		x				x
I acknowledge that these represent my contribution to the above result output. Signed:						
Gordon Parkinson	x			x	x	x
I acknowledge that these represent my contribution to the above result output. Signed:						
Juntao Wei		x				x
I acknowledge that these represent my contribution to the above result output. Signed:						
Muhammad Asif Akhtar		x				x
I acknowledge that these represent my contribution to the above result output. Signed:						
Chun-Zhu Li	x		x	x	x	x
I acknowledge that these represent my contribution to the above result output. Signed:						

Every reasonable effort has been made to acknowledge the owners of copyright material. I would be pleased to hear from any copyright owner who has been omitted or incorrectly acknowledged.